



Implicit Dynamic Active Constraints for Robotic Arthroscopy with Surface Reconstruction

Edoardo Lopez

A thesis submitted in partial fulfillment of the requirements for the degree of
MRes in Medical Robotics and Image Guided Intervention and for the Diploma
of Imperial College

Imperial College London

Department of Surgery and Cancer

September 2012

**Dr. Ka-Wai Kwok
Prof. Guang-Zhong Yang**

Statement of Originality

I herewith declare that I have produced this paper without the prohibited assistance of third parties and without making use of aids other than those specified; notions taken over directly or indirectly from other sources have been identified as such. This paper has not previously been presented in identical or similar form to any other English or foreign examination board.

The thesis work was conducted from January, 23rd 2012 to September, 14th 2012, under the supervision of Prof. Guang-Zhong Yang and Dr. Ka-Wai Kwok at Imperial College London, Department of Surgery and Cancer.

London,

*Ai miei genitori,
presenti in ogni momento della mia vita.*

Acknowledgments

I would like to express my deep gratitude to Prof. Guang-Zhong Yang, for his guidance and for allowing me to have this experience. I would like to acknowledge also the Rector's Scholarship Fund, that has been a precious support during this year.

I would also like to thank Dr. Ka-Wai Kwok, for always being supportive, both scientifically and emotionally, and for having always helped me each time I needed. I am also particularly grateful for the assistance given by Mr. Petros Giataganas, who was always present while completing this thesis.

I would like to offer my special thanks to Dr. Valentina Vitiello, for her advices, and Mr. Christopher J Payne, for having designed the flexible instrument.

I would like to express my very great appreciation to Dr. Daniel Elson, for having organised the MRes course with great care, and to all the other people within the Hamlyn Centre, for offering me their help.

Finally, I would like to thank my family, and all the people who have been so close to me and so understanding, people that I will never forget.

Contents

List of Figures	vii
List of Tables	x
List of Acronyms	xi
1 Introduction	1
1.1 Project description and main novelties	6
1.2 Thesis structure	10
2 Robotic Knee Chondroplasty	12
2.1 Introduction	12
2.2 Knee arthroscopy	12
2.2.1 Lavage, Shaving and Debridement	13
2.2.2 Abrasion chondroplasty	15
2.2.3 Laser chondroplasty	15
2.3 State of the art in Orthopaedic Robots	18
2.3.1 Active Robots	18
2.3.2 Semi-active Robots	19
2.3.3 Passive Robots	20
2.4 Intracorporeal constraints for minimally invasive surgery	21
2.4.1 Remote Centre of Motion	21
2.4.2 Prevention of undesired tissues damages	24
2.5 Active Constraints Control	26
2.5.1 Demands for Dynamic Active Constraints	29
2.6 Conclusions	30

CONTENTS

3 6 Dimensions Active Constraints	31
3.1 Introduction	31
3.2 Impedance control for high-dimension constraints	33
3.2.1 Orientation constraints	34
3.2.2 An alternative implementation technique	36
3.2.3 Prescription of surgical path	41
3.2.4 Reduction of drift error	43
3.2.5 Implementation on the FRI	53
3.3 Validation of 6 DoFs Active Constraints algorithm	54
3.3.1 Simulation of external forces	55
3.3.2 Experimental results	57
3.3.3 Discussions	60
3.4 Conclusions	61
4 Dynamic Active Constraints	62
4.1 Introduction	62
4.2 Real-time tracking underdynamic environment	63
4.2.1 Calibration between tracking system and LWR.	64
4.2.2 Trocar position during repositioning	68
4.2.3 Instrument motion during repositioning	69
4.3 Flexible instrument for knee arthroscopy	71
4.3.1 Kinematic analysis	72
4.3.2 Dynamic adaptation of the Active Constraints law	73
4.3.3 Calibration of the flexible instrument	76
4.3.4 Experimental results	77
4.3.5 Discussion	78
4.4 Conclusions	80
5 Implicit Active Constraints	82
5.1 Introduction	82
5.2 Surface interpolation	83
5.2.1 ABOS interpolation	83
5.2.2 Extended ABOS method	84
5.2.3 Advantages of the proposed method	88

CONTENTS

5.2.4	Evaluation of the surface normal	89
5.2.5	Lattice mesh and robot stiffness	92
5.2.6	Post-smoothing interpolation	93
5.2.7	Validation of surface reconstruction	99
5.3	Implicit evaluation of the trocar position	102
5.4	Subject tests	103
5.4.1	Experimental protocol	103
5.4.2	Results	106
5.4.3	Specification for the flexible instrument	113
5.4.4	Discussion	114
5.5	Conclusions	115
6	Conclusions	117
6.1	Achievement of this thesis	117
6.2	Ongoing research and future directions	120
Bibliography		121

List of Figures

1.1	Diseases causing disability in activities	3
1.2	Four DoFs involved in an arthroscopic procedure	3
1.3	Flexible instruments for hip arthroscopy	4
1.4	Usefulness of flexible instruments in hip, knee and ankle arthroscopy . .	5
1.5	Main reference frames in the operative theatre	7
1.6	Sketch of the LWR	7
2.1	Usefulness of lavage and debridement for knee osteoarthritis	14
3.1	Constraining the instrument to pass through the trocar point	32
3.2	Dealing with the reduced room within the joint	32
3.3	Definition of reference frames for the rigid instrument	34
3.4	Instrument motion due the conical motion constraint	37
3.5	Decomposition of the instrument motion due to the conical constraint .	38
3.6	Force felt by the surgeon when constraining his motion on a pre-planned surface	44
3.7	Definition of the maximum tangent to chord angle parameter	47
3.8	Maximum angle of tangent and chord factor	48
3.9	Force felt by the surgeon when constraining his motion on a pre-planned surface after the Catmull spline Interpolation	51
3.10	Simulation of an external operator	57
3.11	Mean value of the position error $e_p(t)$	59
3.12	Mean value of the orientation error $e_o(t)$	59
3.13	Analysis of the stability of the proposed control law	60
4.1	Introduction of a tracking system in the proposed setup	63

LIST OF FIGURES

4.2	Validation of the proposed calibration procedure - position	66
4.3	Validation of the proposed calibration procedure - orientation	67
4.4	Flexible instrument for knee chondroplasty	71
4.5	Definition of the reference frames for the flexible instrument	72
4.6	Multithread architecture of the control program	76
4.7	Calibration of the flexible instrument - bending angle	78
4.8	Calibration of the flexible instrument - f_x and f_z	79
5.1	eABOS <i>base</i> plane	87
5.2	Results of the <i>Circulation</i>	87
5.3	Results of the eABOS method	88
5.4	Theoretical explanation of how to evaluate the normal of the reconstructed surface	90
5.5	eABOS normal evaluation	92
5.6	Results of the eABOS normal evaluation	93
5.7	Representation of the <i>post-smoothing interpolation</i> method	96
5.8	eABOS post-smoothing interpolation	96
5.9	Reduction of computational time due to post-smoothing interpolation .	98
5.10	eABOS validation: Ground truth	99
5.11	Results of the eABOS interpolation: mean error	100
5.12	Results of the eABOS interpolation: standard deviation	101
5.13	Comparison between the ground truth and the reconstructed surface .	102
5.14	The experimental setup for the Subject tests	104
5.15	Pre-planned path on the articular cartilage	105
5.16	Time to completion - All subjects (s)	107
5.17	Orientation error - All subjects (mm)	107
5.18	Intracorporeal error - All subjects (mm)	108
5.19	Intracorporeal, Extracorporeal and Orientation errors	108
5.20	Extracorporeal error - All subjects (mm)	108
5.21	Quantile-Quantile Plots for the analysed data	109
5.22	Analysis of the performance indices	110
5.23	Difficulty index (qualitative survey) - All subjects	111
5.24	Difficulty index (qualitative survey) - Statistical analysis	111

LIST OF FIGURES

5.25 Control ergonomics - Acquisition of control points	113
5.26 Illustration of the centre of motion C and the range of motion R	113
5.27 Evaluation of the centre of motion C and the range of motion R	114

List of Tables

1.1	Incidence, prevalence and cost of different types of osteoarthritis.	2
1.2	Clinical relevance, novelties and aim of experiments.	11
2.1	Statistical significance evaluation of real benefits of lavage and debridement after 1 year and 2 years follow-up [60].	14
2.2	Laser sources property, pros and cons.	17
2.3	Main characteristics for principal <i>active</i> and <i>semi-active</i> orthopaedic robots.	22
3.1	Suggested values for defining the robot stiffness and the interpolation lattice grid dimension.	48
3.2	Parameters for the validation of the proposed <i>active constraints</i> technique. .	58
4.1	Calibration of the flexible instrument - Numerical coefficients.	79
5.1	<i>HP Z400 Workstation</i> properties	94
5.2	Computational time of the extended ABOS method	94
5.3	Results of the Subject tests: performance indices.	112

List of Acronyms

ABOS	Approximation Based On Smoothing	GUI	Graphic User Interface
ADL	Activities of Daily Living	KRC	KUKA Robot Controller
CAS	Computer Assisted Surgery	KRL	KUKA Robot Language
CPI	Consumer Price Index	LWR	KUKA Light Weight Robot 4+
CT	Computer Tomography	MIS	Minimally Invasive Surgery
DC	Direct Current	MRI	Magnetic Resonance Imaging
DoF(s)	Degree(s) of Freedom	RCM	Remote Centre of Motion
eABOS	extended ABOS	RPY	Roll-Pitch-Yaw
ECG	Electrocardiography	THA	Total Hip Arthroplasty
FDA	Food and Drug Administration	TKA	Total Knee Arthroplasty
FRI	KUKA Fast Research Interface	UKA	Unicondylar Knee Arthroplasty
GPU	Graphic Processing Unit		

Abstract

A robotic system for minimally invasive laser knee chondroplasty is presented in this thesis. Laser chondroplasty has been demonstrated to be an effective surgical approach for treatment of early-stage osteoarthritis, a disease affecting over 10 million people alone in the UK [7].

The research objective is to develop a safe robotic system, that can enhance the surgical performances, by providing *in situ* manipulation guidance during a minimally invasive procedure. A 2 degrees-of-freedom (DoFs) flexible arthroscopic instrument is coupled with a 7 DoFs commercial compliant manipulator. The control concept of Implicit Dynamic Active Constraints is proposed, by which the robot is capable of constraining the orientation of the instrument so as to pass through the incision point, so not to cause excessive injuries to the tissues around the port. To increase the safety of the operation, the proposed method also provides a haptic interaction for constraining the instrument tip motion within a pre-defined cartilage region. This requires a technique that can reconstruct the articular cartilage surface from just a set of not-ordered control points, without having to acquire pre-operative images, thus reducing the setup time and the radiation dose to the patient. The use of the flexible arthroscopic instrument is also investigated to enlarge reachable and dexterous workspaces. The possibility of reaching the target anatomy with an optimal approach direction is of importance to increase the ablation rate and to reduce the thermal damaged areas during laser chondroplasty. The proposed framework is capable to adapt to a dynamic surgical scenario, so that the manipulation guidance can be automatically adjusted while the knee is re-positioned by the operator. An algorithm for registering the tracking system relatively to the robot base frame is proposed.

The stability of the control framework is also proved by simulating external disturbances. The surface reconstruction technique is validated and the kinematics of the flexible instrument is fully characterised. A detailed performances analysis is conducted on a group of subjects for validating the framework, simulating an arthroscopic procedure. Results demonstrate a statistically significant enhancement in the control ergonomics and in the accuracy and safety of the procedure.

Chapter 1

Introduction

In this thesis, a robotic system for knee arthroscopy will be presented. Arthroscopy is an early-stage treatment of osteoarthritis, the most diffuse type of arthritis, which represents the most common disease causing disability [61]. Arthroscopic intervention is cost-effective and represents a revision surgery that can be repeated several times, if necessary, without considerable complications [32].

Arthritis is affecting over 10 million people alone in the UK in 2010 [7], and more than 43 million people in the US in 2003 [88]. This disease is costing the UK £5.7 billion per year in health and social care services [7]. An overall medical care expenditure of \$ 6,978 per year per person was esteemed in the US in 2003, with a total cost of \$ 81 billion per year [88]. Moreover, due to the disabling nature of this disease, earning losses were evaluated of \$ 3,163 per year per person [88]; thus, a total economic burden of \$ 10,141 (April 2012 \$ 12,643, considering US government Consumer Price Index (CPI) data released on April 13, 2012) per year per person can be attributed to arthritis. It is worth noticing that knee osteoarthritis has the highest incidence, *i.e.* the number of new cases per year among the population considered disease-free at the beginning of the reference time, and prevalence, *i.e.* the number of diseased people among the total number of analysed subjects; resulting in the highest costs compared to other kinds of osteoarthritis affecting, for example, hands or hips. As shown in Table 1.1, incidence of knee osteoarthritis is more than double than hands or hips one, with the highest prevalence in subjects over 45 years. In Table 1.1, prevalence was distinguished in Radiologic osteoarthritis and Symptomatic osteoarthritis, where, according to Murphy and Helmick [61]:

1. INTRODUCTION

“Radiographic osteoarthritis is based on information from X-rays and can be defined with either individual features or, more commonly, the Kellgren-Lawrence scale of 0 to 4 [...]. Symptomatic osteoarthritis is defined as the combination of radiographic evidence of osteoarthritis and symptoms (pain, stiffness) in the radiographically affected joint.”

Table 1.1: Incidence, prevalence and cost of different types of osteoarthritis.

	Standardized incidence per 100,000 persons (1990) [63]	Prevalence		Total joint replacement	
		Radiologic osteoarthritis (2000) [46]	Symptomatic osteoarthritis (2000) [46]	Number of operations (2009) [61]	Total cost (billion \$) (2009) [61]
Hands	100	27.2% (≥ 26) ¹	6.8% (≥ 26) ¹	—	—
Knees	240	13.8% (≥ 26) ¹ 27.8% (≥ 45) ²	4.9% (≥ 26) ¹ 16.7% (≥ 45) ²	620,192	28.5
Hips	88	27.0% (≥ 45) ²	9.2% (≥ 45) ²	284,708	13.7

It is worth noticing that, referring to data provided by Guccione *et al.*, which are summarised in Fig. 1.1, knee osteoarthritis represents the major cause of disability in lots of activity, *i.e.* stair climbing (16.7% of disability attributable to knee osteoarthritis), walking a mile (15.4%), housekeeping (16.7%) and carrying boundles (16.6%), when compared to other major diseases such as hip fractures, diabetes, strokes and heart diseases [27].

The focus of this thesis is on minimally invasive laser chondroplasty, an effective surgical procedures that is presenting some advantages over other procedures, such as lavage, shaving, debridement, burr arthroplasty and Pride drilling, as shown in Section 2.2.

During a minimally invasive arthroscopic procedure, the instrument has always to pass through the incision point not to create damages to the skin, that acts as a Remote Centre of Motion (RCM); resulting in a reduction of number of Degrees of Freedom (DoFs) from 6 to 4 (pan, tilt, rotation around the instrument axis and instrument insertion), as shown in Fig. 1.2. Thus, a rigid instrument has to move within a double cone having a vertex in the RCM.

¹Framingham OA study, subjects older than 26

²Johnston County OA Project, subjects older than 45

1. INTRODUCTION

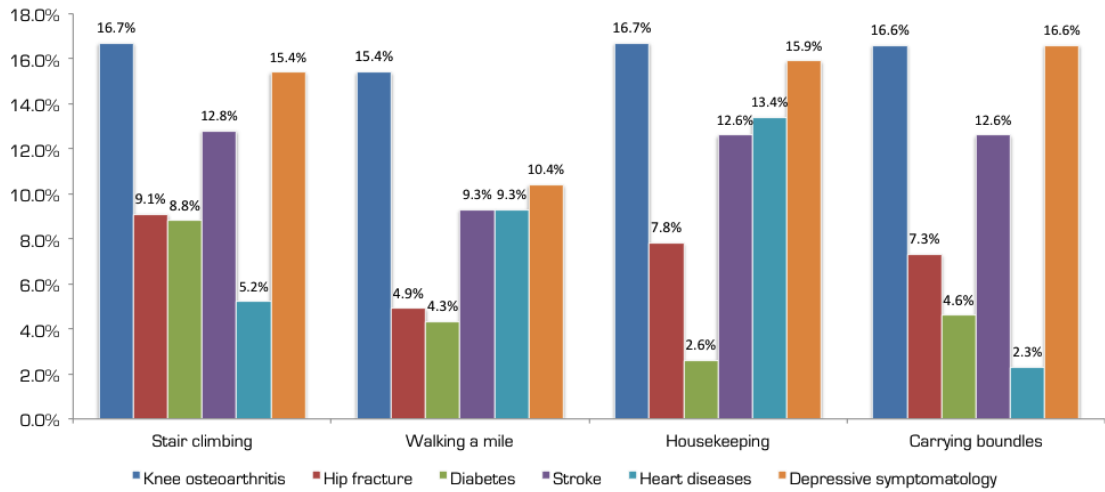


Figure 1.1: Diseases causing disability in activities - Data were adjusted for age, sex and comorbidity. Comparison among different diseases [27].

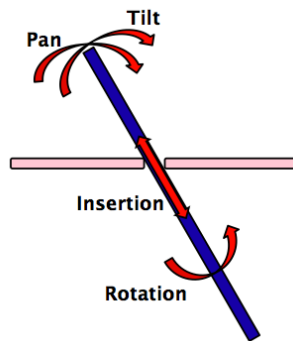


Figure 1.2: Four DoFs involved in an arthroscopic procedure - The fulcrum effect reduces the number of DoFs and mirrors the surgeon's movements.

1. INTRODUCTION

Moreover, since the layer of the cartilage that has to be ablated is relatively thin, a safe region where the operator has to move in, and a forbidden region where the operator is not allowed to penetrate, have to be defined intra-operatively without requiring pre-operative imaging, such as Computer Tomography (CT) and Magnetic Resonance Imaging (MRI).

Confined anatomical cavities highly limit the motion inside the joint. Thus reduces the feasibility of performing a minimally invasive procedure, especially near convex surfaces [40]. To this end, a flexible instrument can be developed to improve the accessibility to the target anatomy, enhancing reachable and dexterous robotic workspace. The same target can be reached with various poses of the instrument.

Referring to Shenker and Philippon [72] and Kelly *et al.* [40], hip arthroscopy would have not been carried out without the introduction of flexible instruments (such as the instruments by Smith & Nephew Plc, Andover, MA¹, Fig. 1.3). In this sense, the femoral head, the acetabulum and the acetabular fossa can not be exposed using straight rigid instruments due to spatial constraints [26]. Hence, the use of flexible instruments allowed some arthroscopic procedures such as the definition of the margins of the labral tears through debridement [39, 67] or using a Radio Frequency (RF) probe [71], and treatment of capsular laxity with flexible RF probes [71].



Figure 1.3: Flexible instruments for hip arthroscopy - The EFLEX Instruments are used in clinical practice for hip arthroscopy, increasing the surgical workspace.

Another convex surface within the knee is represented by the condyles, the distal part of the femur that articulates with the tibia through the menisci. Therefore, there is a rising demand in developing flexible instruments for arthroscopy, designed to introduce additional intra-corporeal DoFs, so that the overall dexterity of the system can

¹<http://global.smith-nephew.com/us/>

1. INTRODUCTION

be improved [17, 78]. Takalhashi and Yamamoto developed a flexible instrument for arthroscopy, which was tested for hip, knee and ankle arthroscopy [78]. A survey was then submitted to surgeons, where they had to report whether or not the introduction of the flexible instrument had improved the outcome of the procedure. Results are summarised in Fig. 1.4.

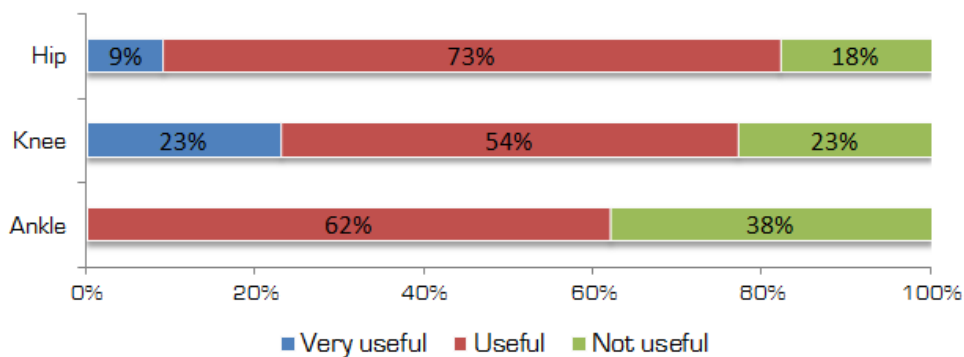


Figure 1.4: Usefulness of flexible instruments in hip, knee and ankle arthroscopy - Instrument was tested in hip arthroscopy (11 patients), knee arthroscopy (13 patients, 8 of which with osteoarthritis) and ankle arthroscopy (21 patients) [78].

It is worth noticing that, while the flexible instrument is not reported not to be very useful for ankle arthroscopy, it is claimed to be really useful more for knees than for hips (23 % vs 9%), and claimed to be at least useful in more than 75% of procedures for both knee and hip arthroscopy. Thus, the development of a flexible instrument for knee arthroscopy represents a really interesting research topic, due to its novelty and its usefulness in clinical practice.

However, the introduction of additional intracorporeal DoFs increases the complexity of the surgical task, since instrument DoFs and external position have to be set concurrently in order to reach the desired intracorporeal position; considering a flexible instruments with n DoFs, the surgeon has to control concurrently $6 + n$ DoFs, *i.e.* the position of the flexible instruments (3 DoFs), its orientation (3 DoFs) and the additional DoFs, thus increasing the cognitive burden.

Besides, when performing a laser chondroplasty, the instrument should be as perpendicular as possible to the articular surface for increasing the ablation rate, reducing the operative time and the thermal damaged area. Thus, the instrument DoFs can be automatically controlled for reaching an optimal approach direction.

1. INTRODUCTION

The flexible instrument can be attached to the end-effector of a compliant robot, which will “guide” the surgeon to be inside the safe zone, avoiding undesired collisions, still dealing with the constraints of Minimally Invasive Surgery (MIS), such as the pivoting effect due to the incision point. Thus, this thesis will deal with the following research objectives:

1. To introduce a cooperative control system for a compliant robot under a hands-on approach, for improving surgeon performances while providing him with haptic interactions;
2. To increase the safety of the operation constraining the surgeon’s motion on a pre-planned surface or path, that will be implicitly defined from the surgeon’s first movements;
3. To consider a dynamic scenario, where limb re-positioning might occur and the control system has to quickly adapt to the new situation;
4. To autonomously control a flexible instrument in order to reduce the number of DoFs that the surgeon has to directly control, maintaining the instrument roughly perpendicular to the bone surface in order to improve the outcomes of the laser chondroplasty, still considering the additional constraints of a MIS application.

The process requires registration among different reference frames, such as 1) the operative theatre, 2) the robot base, 3) the tracking system and 4) the markers on the patient’s knee (Fig. 1.5).

Last but not least, the stability of the system has to be guaranteed, for proving the safety of the proposed solution.

1.1 Project description and main novelties

A 7 DoFs manipulator, *i.e.* the *KUKA Light Weight Robot 4+* (LWR, Fig. 1.6) and a flexible 2 DoFs hand-held device can be coupled, and a control architecture for the whole system is proposed in this thesis.

The LWR was designed to interact with people in an unstructured environment. It is equipped with strain gauge-based torque sensors, magneto-resistive position encoders and potentiometers. The actuation system is composed by specifically designed motors

1. INTRODUCTION

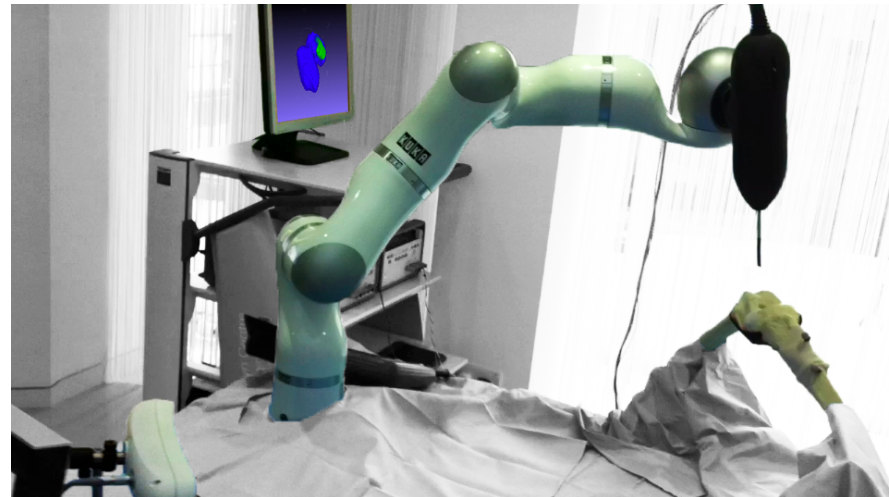


Figure 1.5: Main reference frames in the operative theatre - Main components of the proposed solution are coloured in this image.

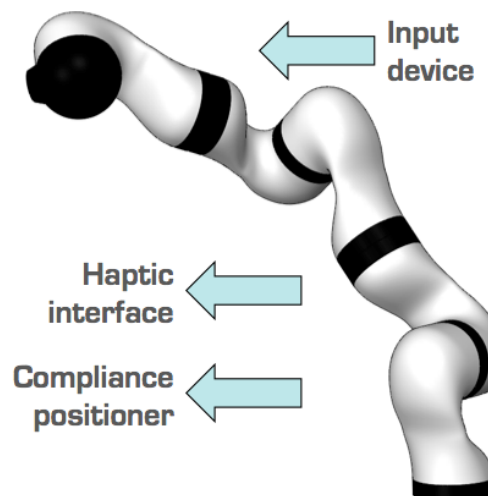


Figure 1.6: Sketch of the LWR - The LWR will be exploited as an accurate positioner, and as an input device considering a *hands-on* control architecture.

1. INTRODUCTION

and harmonic drive transmissions [3]. Back-driveability is not obtained mechanically, but through the control system [29]. The robot stiffness can be set by the operator; the higher is the stiffness, the higher is the accuracy in positioning tasks, whereas safety can be increased reducing the stiffness. The external torque is estimated by a state-observer, where the input parameters are the torques measured by the torque sensors and the dynamic model of the robot (in terms of masses, Coriolis and gravitation forces) [29]. The end-effector interaction force is estimated using the kineto-statics duality, once the external torque has been evaluated.

The manipulator is controlled by a two-loops control architecture, where the inner loop is a joint level control (performed in a 3 kHz cycle) and the outer loop is computed in a 1 kHz cycle. Three outer control modalities are provided: joint space position control, and both operational space and joint space impedance control, where the stiffness of the end effector in each direction (operational space control) or of each joint (joint space control) can be set independently. The inverse kinematics is not obtained using an inversion algorithm based on the pseudo-inverse Jacobian matrix, but a customized inversion algorithm was introduced to face up with singular configurations, exploiting the redundant DoF [3].

The user can establish his control law using the KUKA Robot Controller (KRC), that has to be programmed in KUKA Robot Language (KRL), or defining some parameters using the KUKA Fast Research Interface (FRI). The KRC represents the core of the control system (cycling at 1 kHz), while the FRI is a communication toolkit that allows the user to modify some parameters in the KRC. Since the FRI communicates with the KRC through the UDP port, the maximum update rate is determined by the packet size. Preliminary experimental investigations carried on in the Hamlyn Centre showed a maximum update rate equal to 5 ms. Considering the operational space impedance control, the robot will be controlled according to the following law [73]:

$$\tau_{\text{contr}}^{\text{FRI}} = J^T [k_c (x_d - x) + F_{ext}] + D(d_c) + f_{\text{dynamics}}(q, \dot{q}, \ddot{q}) \quad (1.1)$$

where $\tau_{\text{contr}}^{\text{FRI}} \in \mathbb{R}^{7 \times 1}$ is the control torque, $J \in \mathbb{R}^{6 \times 7}$ is the Jacobian matrix (kineto-statics duality is exploited), $k_c \in \mathbb{R}^{6 \times 6}$ is a diagonal control gain matrix, $x_d \in \mathbb{R}^{6 \times 1}$ is the desired pose, $x \in \mathbb{R}^{6 \times 1}$ is the actual pose, $F_{ext} \in \mathbb{R}^{6 \times 1}$ is an arbitrary additional external force that can be set by the user, $D(d_c) \in \mathbb{R}^{7 \times 1}$ is a damping vector depending on the damping coefficient d_c that can be set by the user and $f_{\text{dynamics}}(q, \dot{q}, \ddot{q}) \in \mathbb{R}^{7 \times 1}$ is

1. INTRODUCTION

the robot dynamic compensation (not modifiable). User can set through the FRI the diagonal control gain matrix, the desired position, the external force and the damping coefficient. It is worth noticing that the LWR is not equipped with joint velocity transducers, and velocity has to be estimated deriving position measurements.

The hand-handle device is a 2 DoFs instrument able to *bend* and *rotate* around its shaft. The bending mechanism is tendon driven, and it is similar to the one proposed by Dario *et al.* [17]; the instrument has one cavity, for hosting a flexible endoscopic camera equipped with illumination and/or the surgical instrument (a milling drill if abrasion chondroplasty is performed, or an optical fibre for laser chondroplasty, see Section 2.2).

The focuses of this thesis will be placed on the following aspects and novelties, which will facilitate the potential clinical translation of this research:

1. **6 DoFs Active Constraints technique** is introduced, to constrain both position and orientation, using a compliance control, instead of considering an impedance control (where the external forces has to be sensed and used as input). Using a compliant robot, the error between the actual pose and the desired one is used as input, reducing additional costs due to force/torque sensors and problems related to the force sensor noise. Thus, an impedance (6×6) matrix is evaluated, relating the user linear and angular velocity to the control force and torque.
2. **Pre-planned cartilage region** is implicitly derived. Once the surgeon had acquired few control points within the operative site in a random order, the pre-planned surface is automatically defined. Moreover, other additional MIS constraints, such as the trocar position, are implicitly derived.
3. **A 7 DoFs compliant manipulator and a flexible instrument** are integrated. A hands-on cooperative approach is proposed, rather than a fully automatic or a master-slave control, because of its higher performances and its higher acceptability within the clinical community [48]. The flexible instrument is autonomously controlled for providing the optimal access to the target anatomy.

1. INTRODUCTION

4. **Manipulation guidance adapted with knee re-positioning** is introduced, for reducing the intra-operative setup time. Tracking system for the configuration of the knee is designed. Real-time registration between the patient's knee and the operative site is implemented.
5. **Promising control stability** is guaranteed. To evaluate the stability of the approach, extended disturbances are introduced, exploiting some unique features of the compliant manipulator.

1.2 Thesis structure

The Literature Review (*Chapter 2*) will investigate the major procedures for knee arthroscopy. The state of the art in orthopaedic robots will then be reviewed.

In *Chapter 3*, a 6 DoFs *Active Constraints* technique will be proposed, which will address some problems of minimally invasive surgery. Stability of the system will be evaluated.

A flexible instrument with 2 DoFs (tip bending and rotation along the instrument shaft) will be introduced in *Chapter 4*, in order to increase the workspace and the ablation rate. The tool can be used for abrasion and laser chondroplasty, when a proper probe is added. The instrument will be kinematically characterised, and it will be integrated within the proposed solution. Moreover, limb re-positioning will be taken into account, tracking the limb motion using an optical tracking system.

A technique for implicitly reconstructing the surface from the few control points will be presented in *Chapter 5*, as an extension of the Approximation Based on Smoothing (ABOS) method proposed by Dressler, 2007 [21]. A technique for deriving the port placement will be introduced. Subject tests will be carried on for evaluating the real benefits of the proposed solution. Both quantitative and qualitative assessments will be performed, and whether or not the enhancements are statistically significant will be evaluated.

Finally, results will be summarised in *Chapter 6* and future works will be presented.

Tab. 1.2 summarises the clinical relevance, the novelties and the aim of the experiments for Chapters 3 - 5.

1. INTRODUCTION

Table 1.2: Clinical relevance, novelties and aim of experiments.

Clinical relevance	Novelties	Aim of experiments
Ch. 3	The Active Constraints technique is an intuitive method for increasing surgical performances, constraining the motion on pre-planned surfaces that can be defined <i>in situ</i> , not requiring sophisticated registration between the pre-operative images and the patient, avoiding the use of screws or other fiducial markers. Constraints can be derived implicitly from the surgeon's motion. This technique can be used for increasing surgeon's performances, since his motion can be readjusted for respecting the anatomical constraints of a MIS procedure.	An impedance (6×6) matrix is evaluated for constraining the instrument pose. Stability is guaranteed, introducing external disturbances.
Ch. 4	The use of a flexible instrument can enhance the dexterity of the proposed robotic-assisted framework and potentially improve the ablation rate when performing laser chondroplasty. The instrument configuration can be automatically set, resulting in a simpler surgical procedure. For reducing intra-operative setup times when limb re-positioning occurs, a tracking system is introduced.	The use of a flexible instrument allows to re-establish the intra-corporeal dexterity. The Active Constraints technique is extended to integrate the additional DoFs. A tracking system is used for reducing setup times. A calibration technique is proposed for automatic, fast and robust registration between the tracking system and the robot base frames.
Ch. 5	The eABOS interpolation technique can be used for implicitly reconstructing the articular cartilage surface. The technique is suitable when control points are acquired in a random order, thus increasing the control ergonomics and the acceptability within the clinical community. The surface is continuous in C^1 , to obtain seamless motion transitions so that energy will not be stored, assuring that the system will be safe.	The ABOS method is extended for surfaces not explicitly definable in the base reference frame; normal direction evaluation is performed and post-smoothing interpolation is used for speeding up the process. No prior knowledge is required, since points can be acquired <i>in situ</i> . External constraints are evaluated from the surgeon's initial movements.

Chapter 2

Robotic Knee Chondroplasty

2.1 Introduction

This chapter covering a detailed review of procedures, robotic systems and techniques for chondroplasty is structured as follow: Section 2.2 describes minimally invasive arthroscopic procedures for knee surgery, focusing mainly on laser chondroplasty; Section 2.3 reviews the state of the art in orthopaedic robots, categorising them in *active*, *semi-active* and *passive* robots; Section 2.4 deals with constraints that have to be taken into account when performing an arthroscopic procedure, and Section 2.5 refers to the *Active Constraints* Technique, which is applied for cooperative control for avoiding collision or constraining the motion of the instrument.

2.2 Knee arthroscopy

Several arthroscopic treatments have been developed for solving osteoarthritis [61]:

1. *Lavage*, irrigation of joints with appropriate solutions;
2. *Shaving*, removal of chondrial tissue;
3. *Debridement*, combination of both lavage and shaving, where fluids are removed from the joint;
4. *Laser chondroplasty*, removal of tissue using laser light;
5. *Abrasion chondroplasty, Pride drilling, microfracture creation and spongialization*, creation of bone damages and holes in order to stimulate natural repair.

2. ROBOTIC KNEE CHONDROPLASTY

Effective approaches to arthroscopy are demanding for the prevention of final-stage treatments, namely total/partial joint replacement (*arthroplasty*), which represent a huge economic burden for the country [7].

Only few alternatives to these final-stage treatments have been proposed, such as: 1) *Osteotomy*, in which the bone is cut and shortened or lengthened in order to modify its alignment with surrounding bones; 2) *Joint distraction surgery*, where the bone is fractured and the two parts are gradually moved away and 3) *Periosteal* or *Osteochondral grafting* [61]. However, those interventions cannot be performed using an arthroscopic procedure.

2.2.1 Lavage, Shaving and Debridement

Lavage consists in irrigating the joint with solutions for washing out cartilage fragments. *Shaving* is a treatment where the articular cartilage is shaved in order to make it smoother. Combination of lavage and shaving, *i.e.* smoothing the chondral tissue while irrigating the joint, is called *Debridement*.

Although the presence of benefits is still a question without any strong clinical proof, these treatments have been widely used. However, no real benefit have been proved so far. Jackson and Dieterichs carried on a qualitative study, based on symptoms and comfort in Activity of Daily Living (ADL), for defining whether lavage and debridement have long-term benefits or not (after 4 or 6 years). They demonstrated these procedures might be useful only if exerted in early-stage osteoarthritis (Stage I and II, *i.e.* without or with minor radiographic signs), while moderate benefits are shown for Stage III osteoarthritis (major radiographic evidence) and poor benefits are recorded for Stage IV osteoarthritis (bone is directly exposed) [35]. Their results are summarised in Fig. 2.1.

However, Moseley *et al.* conducted a double-blind study that was published on the *New England Journal of Medicine* and involving one hand red sixty-five subjects, demonstrated that benefits after 1 and 2 years are not statistically significant either for lavage or for debridement [60]. In this study, subjects where assigned to have lavage, debridement or placebo procedure (simulating a normal procedure), and qualitative assessments for both pain and functional improvements were performed after 1 and 2 years. No statistically significant benefits were reported for both procedures against the null hypothesis (*i.e.* the placebo procedure), with *p value* higher than 0.6 in every

2. ROBOTIC KNEE CHONDROPLASTY

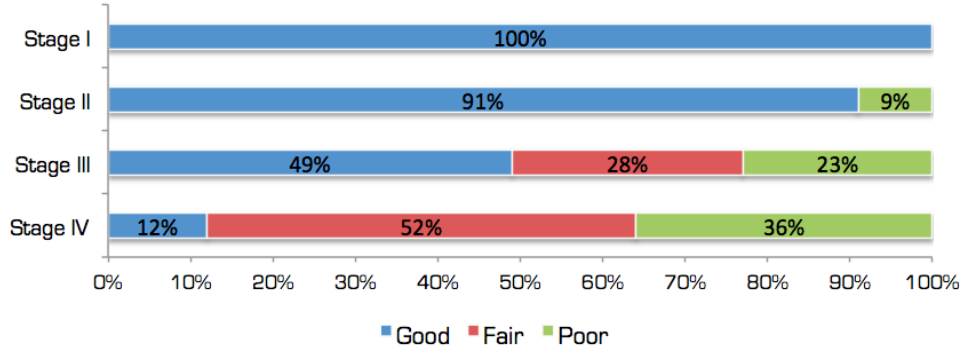


Figure 2.1: Usefulness of lavage and debridement for knee osteoarthritis - *Good* refers to no or reduced pain without limitations in ADL; *Fair* refers to discomfort in ADL but with improvements with respect to the initial condition; *Poor* refers to high limitations in ADL (121 patients) [35].

case after 2 years; thus demonstrating that lavage and debridement are not effective procedures. Results are quoted in Table 2.1.

For all the above mentioned reasons, the current research attention has naturally shifted to chondroplasty.

Table 2.1: Statistical significance evaluation of real benefits of lavage and debridement after 1 year and 2 years follow-up [60].

		Pain ¹		Functional improvement ²	
		1 year	2 years	1 year	2 years
Placebo	Mean \pm SD	48.9 \pm 21.9	51.6 \pm 23.7	49.4 \pm 25.5	53.8 \pm 27.5
Lavage	Mean \pm SD	54.8 \pm 19.8	53.7 \pm 23.7	49.6 \pm 29.1	51.1 \pm 28.3
	P value ³	0.14	0.64	0.98	0.61
Debridement	Mean \pm SD	51.7 \pm 22.4	51.4 \pm 23.2	56.4 \pm 28.4	56.4 \pm 29.4
	P value ⁴	0.51	0.96	0.19	0.64

¹Pain Scale created by the authors, going from 0 (no pain) to 100 (extreme pain) [60].

²Arthritis Impact Measurement - Walking and Bending subscale (AIMS2-WB), converted in a scale going from 0 to 100.

³Lavage vs Placebo

⁴Debridement vs Placebo

2. ROBOTIC KNEE CHONDROPLASTY

2.2.2 Abrasion chondroplasty

Abrasion chondroplasty has been being widely performed in clinical practice [57], and consists in penetrating the cartilage and the bone till bleeding, in order to stimulate spontaneous healing of tissues with formation of fibrocartilage. In dog experiments, absence of synovial inflammation, proliferation of cartilage with fibrillation in the operated area and no formation of osteophytes were observed [4]; indicating a healing response from tissues.

Different methodologies have been proposed, and burr arthroplasty (removal of the cartilage) and Pride drilling (holes are drilled in the bone to achieve bleeding) are the most common. Comparison studies between those modalities were carried on, showing better outcomes for Pride drilling than for burr arthroplasty¹ [57]. According to Menche *et al.*, while in burr arthroplasty the burred tissue is exposed to mechanical load, when performing Pride drilling the drilled areas are protected from load, thus causing disparity in outcomes [57].

However, it is worth noticing that the exact biological healing response mechanism is not fully understood [32, 66]; resulting in a reduction of the acceptability of those techniques.

Moreover, the need of high contact force imposes strict constrain on the stiffness of a flexible probe.

2.2.3 Laser chondroplasty

Laser chondroplasty exploits the energy absorbed by tissues to perform chondrial ablation and reshaping. Different laser sources are available, and they are characterised by a specific wavelength, while tissues absorption coefficient is varying according to the light frequency. If the absorption coefficient is high for a specific laser source, ablation can be performed; otherwise, more energy has to be released within the tissue, thus increasing thermal damages [9].

Several light sources have been investigated for chondroplasty (Table 2.2): CO_2 laser and *Excimer* laser can not be used for flexible chondroplasty (apart from the *XeCl Excimer* laser), since they need a rigid or articulated arm to be transmitted, and fiberoptic can not be used [34]. Moreover, since fluids are used during arthroscopy for

¹Degenerative changes are smaller for Pride drilling (43% vs 60%) [57].

2. ROBOTIC KNEE CHONDROPLASTY

distending the joint, feasibility of using laser beam in an aqueous environment has to be considered. Another advantage of fiberoptic transmittable lasers is that images can be acquired through the optical fibre while ablating the tissue [47].

Among the fiberoptic transmittable and aqueous environment compatible light sources, the xenon-chloride *XeCl* Excimer laser [9, 34, 47], the neodymium:yttrium-aluminum-garnet (*Nd : YAG*) [9, 34, 47], the holmium:yttrium-aluminum-garnet (*Ho : YAG*) [9, 34, 52, 76] and the erbium:yttrium-aluminum-garnet (*Er : YAG*) [34, 52] seem to present the major affinity for chondroplasty.

The *XeCl* is the only one not presenting long-term damages after 12 weeks during *in vivo* experiments [9]; however, its ablation rate is so slow (lower than 5 μm /pulse) to not permit a clinical application of this laser source [34]. The *Nd : YAG* is used in clinical practice, but it presents a poor affinity with the absorption coefficient for hyaline cartilage and fibrocartilage [52], thus increasing the thermal necrosis zone (up to 870 μm) [34]. However, a sapphire or ceramic tip can be used to focus the heating, thus reducing the thermal damaged area (< 230 μm) [34].

The *Ho : YAG* and the *Er : YAG* represent the more interesting laser sources; the first one provides an excellent haemostat control, but the thermal damaged area is not negligible [34], while the water absorption coefficient is 300 times higher for the *Er : YAG* wavelength, thus drastically reducing the thermal necrosis area (< 40 μm) [52].

It is worth noticing that no laser requires contact but the *Nd : YAG* when a sapphire tip is used; thus, no contact force will be exerted on the tip of the surgical instrument, thus reducing constraints about the required stiffness for the flexible device.

In conclusion, laser chondroplasty represents the best candidate for a robotic system for arthroscopy with flexible probes. The reason can be briefly explained by the following points:

- Significant clinical benefits of this treatment can be demonstrated.
- No high contact forces are required, thus relaxing constraints on the stiffness of the flexible probe.

2. ROBOTIC KNEE CHONDROPLASTY

Table 2.2: Laser sources property, pros and cons.

Source	Wavelength	Flex. probe	Aq. Env.	Thermal damage	Pros		Cons
					CO ₂	XeCl	
CO ₂	10.64 μm	X	X	< 200 μm			Smoke has to be removed. Beam has to be transmitted through articulated arm. Synovial inflammation was shown. Gas presence may result in subcutaneous emphysema.
XeCl	308 nm	✓	✓	< 24 μm	No long-term damages. Very precise cartilage ablation.		Ablation rate is low (lower than 5 $\mu m/pulse$), thus not allowing a clinical application of this laser source.
Nd : YAG	1.064 μm	✓	✓	< 230 μm	A sapphire tip can be used for focusing the effect, thus reducing lateral damages. A high healing response was shown (vascularisation of tissues and chondrocytes proliferation). A frequency-doubled laser source can be used (wavelength equal to 532 nm), absorbed by haemoglobin.		Coagulation zone is very large (up to 6 mm) and thermal necrosis area is not negligible. Absorption coefficient is small for hyaline cartilage and fibrocartilage.
Ho : YAG	2.12 μm	✓	✓	< 220 μm	High-quality haemostat control can be provided. Can cut both soft and hard tissues, thus it is widely used in otorhinolaryngology. The ablation rate is high, and linear with the laser energy. It is used for chondroplasty.		Thermal necrosis area is not negligible.
Er : YAG	2.94 μm	✓	✓	< 40 μm			Haemostat control quality is not so good as for the Ho : YAG laser source.

2. ROBOTIC KNEE CHONDROPLASTY

- The laser beam can be transmitted via a bundle of flexible thin optical fibres (core diameter of $600 \mu m$ [9, 47, 52]).
- Thermal damages can be highly reduced using the *Er : YAG* laser source.
- High quality haemostat control can be achieved with *Ho : YAG* light source.
- Images can be acquired simultaneously while performing the arthroscopic procedure.

2.3 State of the art in Orthopaedic Robots

Computer Assisted Surgery (CAS) was proposed for arthroplasty to increase surgeons' performances using imaging techniques and mechatronic devices. Several solutions were developed for both open operation and MIS¹. However, it is worth noticing that no robotic solutions have ever been introduced for arthroscopy², apart from flexible instruments for increasing dexterity [1, 17, 78] and a robot proposed for arthroscopic procedures by Shirzad *et al.*, that is actually a 6 DoFs manipulator without any specific feature for medical application, and no simulations considering a medical environment or clinical trials had ever been carried on [74].

Robots for CAS can be distinguished in *active* robots, *semi-active* robots and *passive* robots [30]. Active robots perform the planned surgery autonomously; semi-active robots constrain surgeons' movements in order to enhance the final outcome of the operation; while passive robots do not perform any action, but help the surgeon to locate the instruments.

2.3.1 Active Robots

The first robot specifically designed for arthroplasty is the *ROBODOC* system, cleared by Food and Drug Administration (FDA) in 1994-1995 for total hip arthroplasty (THA) [53, 77]. It is a SCARA manipulator with 2 additional DoFs, able to autonomously mill

¹MIS refers to procedures where the incision length is reduced (by the way of example, MIS total knee arthroplasty can be performed with an incision length of 4 *in*, compared to an incision of 12 *in* when performing an open total knee arthroplasty).

²Literature review carried on the following database: *Web of Science*, *Current Contents Connect*, *Derwent Innovations Index*, *CABI: CAB Abstracts*, *MEDLINE*, *Journal Citation Reports*, *IEEE Xplore*.

2. ROBOTIC KNEE CHONDROPLASTY

a bone cavity according to a preoperative plan based on CT data. The *CASPAR* system is similar to *ROBODOC*, to the extent that it realises the cavity according to the CT image [77], and it is used for total knee arthroplasty (TKA), THA and ligamentoplasty in knee [53, 81]. Other two systems, the *MARS* (also known as *Mazor's SpineAssist*) [85, 86] and the *MBARS* [84, 85], use a Stuart-Gough parallel manipulator for needle insertion during spinal operations or for bone drilling during arthroplasty, respectively: one of the platforms of the Stuart-Gough structure is rigidly attached to the operated bone, while the other can move according to a pre-operative model. Mitsuishi *et al.* proposed a 7 DoFs system to perform TKA or unicondylar knee arthroplasty (UKA); the kinematic structure was designed in order to achieve an adequate workspace, still providing a good line-of-sight to the surgeon [58]. Kim and Minh investigated a lateral access procedure for MIS TKA using a 6 DoFs industrial robot [42].

All the above-mentioned solutions are intended to automatically bring to completion the intended arthroplasty (*active* robots), and the surgeon is *out from the control-loop*. This simplifies the control of the robot, since no human components interfere with the control system. However, this solution represents a sub-optimal allocation of function, since the excellent judgment capabilities of the surgeon and his ability to improvise are not exploited, resulting in a reduced acceptability by both surgeons and patients.

2.3.2 Semi-active Robots

In order to re-introduce the surgeon in the control-loop, two other commercial systems, the *ACROBOT* and the *MAKOplasty*, were developed, which use a pre-operative CT image to constrain the surgeon's movements in order to achieve a better outcome in arthroplasty (*semi-active* robots). Two main approaches have been introduced to allow the surgeon to interact with the robot, and thus with the patient: the *hands-on* approach and the *master-slave* approach. When using a hands-on approach, the surgeon directly interacts with a handle device located close to the end-effector of the manipulator. A force control strategy is generally implemented, where the force exerted by the operator to the handle device has to be measured, and the force exerted by the robot is properly established in order to limit surgeon's movement. On the contrary, in a master-slave approach the surgeon interacts with a master interface, and his movements are directly mapped in the movements of another manipulator (i.e. the slave device), which interacts with the patient's tissues. Thus, a position control strategy

2. ROBOTIC KNEE CHONDROPLASTY

is generally applied, where a haptic feedback can be provided to the surgeon for increasing his performances [56, 79, 83]. However, a hands-on device can be represented as a master-slave system, where “*the master [device] is located directly on the slave manipulator*” [18]. Li *et al.* compared these approaches to control a no back-driveable robot simulating a sinus operation, finding that better outcomes can be achieved when using the hands-on approach¹. Moreover, surgeons claim that the hands-on approach is easier to use when applied to an arthroscopic procedure [48].

The *ACROBOT* was developed for MIS UKA and is composed by two parts: a 4 DoFs gross positioner and a 3 DoFs spherical manipulator that is used for fine manipulation [16, 18, 24, 37, 38]. A 3D model is derived from a CT image, then the model is registered within the operative site and surgeon’s motion is thus constrained using a hands-on approach; the surgeon can move freely when he is inside a “safe” region, while the robot becomes very stiff as the tool-tip approaches the boundaries of the safe region. A similar solution, called *MAKOplasty*, is composed by a 6 DoFs back-driveable manipulator, specifically designed for UKA and THA [30]. Yen and Davies introduced a 6 DoFs manipulator, composed by a 3 DoFs parallel mechanism used for establishing the position of the end-effector and a 3 DoFs orientation mechanism [90]. The robot is designed for TKA, where a lateral milling strategy is applied under a hands-on approach [89]. The *BRIGIT* robot is a 6 DoFs robot that can be controlled with a hands-on approach or with a master-slave approach, where haptic feedback is provided to the surgeon. It does not require a pre-operative model [51]. Another *semi-active* mechatronic device is the *Precision Freehand Sculpture* produced by *BlueBelt*, which is a handheld device where the cutter can retract when the surgeon is trying to mill within a “non-safe” region [13, 30]. The main characteristics of the above-mentioned systems are quoted in Table 2.3.

2.3.3 Passive Robots

The *passive* robots represent the third category of manipulators for orthopaedic applications. These systems are position guides that can be used to increase the accuracy of the intervention. They are generally no back-driveable and thus constrain passively surgeons’ movements. The *Praxiteles* is a bone-mounted robot used for positioning a surgical cutting guide for TKA. Two versions were proposed: the first one was a 2

¹In the master-slave approach, no haptic feedback was provided to the surgeon.

2. ROBOTIC KNEE CHONDROPLASTY

DoFs robot that had to be fixated to both the medial and lateral side of the bone [69]; the second one, intended for MIS TKA, is mounted only on one side of the bone [68]. *Praxiteles* was cleared by FDA in 2008 and a new version, called *iBlock*, was cleared in 2010 [24].

2.4 Intracorporeal constraints for minimally invasive surgery

When considering minimally invasive surgery, undesired collisions with other tissues have to be avoided, and the RCM position have to be constrained. Moreover, the instrument should be roughly perpendicular to the surface of interest, in order to increase the field of view, when an arthroscope is considered, or to increase the ablation rate, when an arthroscopic instrument for laser chondroplasty is used.

2.4.1 Remote Centre of Motion

When considering a MIS approach, the instrument is inserted through a small incision in the patient skin, that acts as a RCM, limiting the surgeon's motion.

When robots are introduced in MIS, the RCM is generally *mechanically constrained*, since this approach is considered really safe, and, by the way of example, a parallelogram mechanism was used in the *da Vinci* system [28].

However, this approach does not allow re-locating the limb while operating. To overcome this problem, two other approaches can be considered: *passive* or *active* constraints.

When the RCM is *passively* constrained, 2 non-actuated DoFs are introduced and the manipulator motion is determined by the position of the trocar and by the actuation of the actuated DoFs; the *AESOP* system is constrained passively [50].

Active constraints (or *programmable* or *software* or *virtual* constraints) are usually applied to open-chain manipulators [12, 50], where the constraint is achieved by a software controller. This approach is more flexible, allows a higher manipulability and can deal with the need of re-positioning during an arthroscopic surgical procedure. However, active constraints for the trocar point are considered less safe, since a fault in the control architecture can hurt the patient.

2. ROBOTIC KNEE CHONDROPLASTY

Table 2.3: Main characteristics for principal *active* and *semi-active* orthopaedic robots.

Robot	Category	DoFs	Applications	Pros	Cons
ROBODOC	Active	5	THA	Progresses showed in real-time on the CT image. Reduced number of failures.	Pain caused by three titanium screws used for the registration process. Longer operative time. No better outcome, according to several clinical studies. Surgeon is not in the loop. Unproved overall added value, not cost-effective. Large skin incision.
CASPAR	Active	6	TKA, THA, Ligamento-plasty	Better alignment; bone cavity suitable for cementless fixation.	Surgeon is not in the loop. Unproved overall added value, not cost-effective.
MARS	Active	6	Spinal needle insertion	High accuracy, repeatability and nominal load/weight ratio. Better outcomes with respect to control group. Minimally invasive access procedure.	It has to be attached to the vertebra. Surgeon is not in the loop.
MBARS	Active	6	Joint arthroplasty	High accuracy, repeatability and nominal load/weight ratio. No CT images required (scanning procedure at the beginning of the operation).	Attached to the bone by three pins. Surgeon is not in the loop.
Mitsubishi <i>et al.</i>	Active	7	TKA, UKA	Small incision; algorithm to avoid damages to the skin. Registration with reflective markers and not screws.	Surgeon is not in the loop.
Kim and Minh	Active	6	MIS TKA (Lateral Access)	Lateral access in order to reduce invasiveness. Registration with optical markers and not screws.	Surgeon is not in the loop.
ACROBOT	Hands-on	4+3	MIS UKA	Usage of active constraints for avoiding penetration in forbidden regions. Registration does not require artificial landmarks. Clinical outcomes show improvements.	It uses four short and small pins for preventing bones movements.

Continued on next page

2. ROBOTIC KNEE CHONDROPLASTY

Table 2.3 – *Continued from previous page*

Robot	Category	DofS	Applications	Pros	Cons
MAKOplasty	Hands-on	6	MIS UKA, MIS THA	Usage of active constraints for avoiding penetration in forbidden regions. Preoperative planning can be defined. A soft-tissue compensation algorithm is implemented. Auditory feedback is provided besides the kinaesthetic feedback. Progresses showed in real-time on the CT image. Failure resistance is taken into account exploiting redundant components. Registration does not require artificial landmarks. The instrument will stop cutting if excessive forces are exerted. Clinical outcomes show improvements.	Large skin incision.
Yen and Davies	Hands-on	6	TKA (Lateral milling strategy)	Usage of active constraints for avoiding penetration in forbidden regions. A cooperative force control is implemented to provide power to the surgeon. It uses lateral milling strategy to improve clinical outcomes. The milling velocity decreases when the cutting forces exceed a threshold value. Lower cost with respect to AC-ROBOT.	It uses four short and small pins for preventing bones movements.
BRIGIT	Hands-on and master-slave	6	TKA, Osteotomy	It can be used in both hands-on and master-slave approaches. It is claimed to be easier to install. Anatomical markers are used instead of preoperative images.	

2. ROBOTIC KNEE CHONDROPLASTY

Heuristic functions were presented by Boctor *et al.* for actively constraining the RCM during needle insertion [12]. Definition of a differential inverse kinematic function was proposed by Azimian *et al.*, where the primary task of constraining the RCM and the secondary task of determining the tool-tip position were introduced [8]. A peculiar form of extended Jacobian, called *Alternative Jacobian*, was analysed by Locke and Patel, where *alternative* operational space variables were established in order to define the Jacobian matrix [50]. The RCM constraint can also be considered as an additional virtual link, thus an open-chain structure can be considered as a parallel mechanism, and both the kinematic and dynamic models can be derived for the virtual closed-chain mechanism [33, 87]. Ortmaier and Hirzinger proposed a kinematic approach for constraining the RCM, whose position is estimated automatically by a state observer according to data collected after having put the instrument inside the human body [64].

When the RCM is *actively* constrained, position controls are generally exploited, thus not allowing for a hands-on approach, but limiting the technique to master-slave teleoperated systems, that are not advisable when considering an arthroscopic scenario [48]. However, in this thesis a new technique for constraining the RCM will be introduced, based on *active constraints* under compliant control, considering all the 6 Cartesian DoFs of the manipulator, which can be used for hands-on systems.

2.4.2 Prevention of undesired tissues damages

In order to reduce potential dangerous collision, contact between the instrument and the patient's tissues has to be avoided. Thus, a *forbidden region* can be derived, where the instrument has not to penetrate into. Explicit margins of forbidden regions for the entire articulated instrument should be realised, while existing solutions for orthopaedic surgery consider only the end-effector position for defining active constraints, ignoring the instrument body.

However, the distance between each point within the instrument and the boundary of the forbidden region has to be calculate in real-time in order to evaluate whether the instrument is penetrating into the forbidden region or not; the process of finding the distance between two objectives in a 3D space is named *Proximity queries*. This process is computational expensive and represents one of the major problems when considering collision between the whole manipulator and the environment. Although

2. ROBOTIC KNEE CHONDROPLASTY

the Euclidean distance is not the best metric from a computational point of view, it is the most used due to its physical interpretation [23].

Finding the distance between two objects X and Y can be defined by the following equation [14]:

$$\min \|x_g - y_g\|_2 \quad x_g \in X \quad y_g \in Y \quad (2.1)$$

Different algorithms have been proposed. They all refer to convex shapes, but can be applied to any object if it can be subdivided into a set of convex shapes. Among popular algorithm, the Gilbert-Johnson-Keerthi procedure does not require pre-processing, and the computational time is proportional to the number of vertices used for defining the objects, whereas the Lin-Canny procedure requires pre-processing for determining the closest features, while the computational time is independent of the complexity of the object once the algorithm has been initialised, considering that the closest features change relatively infrequently [14, 49]. Chakraborty *et al.* introduced a new algorithm, where the condition that “*the normal on the two surfaces at the closest points are aligned with each other*” was exploited [14]. However, using this algorithm, the objects have to be approximated by continuously differentiable functions. Thus, this algorithm can be used for evaluating distances among simple objects, but it does not suit to a surgical scenario, where the anatomical structure can be easily described by a set of points rather than by functions. Moreover, in order to assure that the closest point is unique, a proximity queries algorithm requires one object to be strictly convex, while the other can be only convex [22]. Escande *et al.* introduced a boundary composed of toruses and spheres for approximating objects, called *Spheres and Toruses Bounding Volume - STP-BV*, in order to make them strictly convex [22]. They developed an algorithm to automatically create the bounding volume, when a set of 3D points representing the boundary of a convex geometry is provided.

Kwok *et al.* introduced geometrical considerations for evaluating distances between the margins of a safe region and a snake-like flexible robot; the safe region is considered as the union of a set of cylindrical shapes, and the distance between the snake-like robot and each shape forming the safe zone is measured in parallel [44]. Moreover, if the algorithm is implemented on a parallel architecture, such as the Graphic Processing Unit (GPU), the computational time can be reduced; using the GPU, Kwok *et al.* succeeded in evaluating distance between 14,800 vertices with an update rate equal to 1 kHz.

2. ROBOTIC KNEE CHONDROPLASTY

However, when considering a simple instrument, like a rigid instrument or a flexible instrument with few DoFs, and a complex anatomy described by a dense cloud of points, it might be more efficient and reliable to approximate the instrument shape with a set of cylindrical objects (just one cylinder can be used when considering a rigid instrument), and then evaluating the distance between each point of the cloud representing the anatomical structure and the set of objects representing the surgical instrument. GPU can be exploited advantageously since distance evaluation from the huge number of points describing the anatomical area can be distributed among the several processors composing the GPU. Moreover, the cloud of points representing the anatomy can be substituted by its *r-spherical extension*, where a margin of thickness equal to r is added in order to increase safety [23].

2.5 Active Constraints Control

Active constraints were introduced by Ho *et al.* and implemented on a prototype of the ACROBOT [31] to limit the surgeon’s motion. The surgical field was divided in three regions according to a 3D image registered with the patient, namely a free zone, where the surgeon could move freely, a safe zone, where the surgeon can move only along the boundary, and a transition zone, where the stiffness increases linearly for stability reason. The distance to the safe zone was evaluated dividing the 3D model in slices and computing the distance for several planes, resulting in a computational expensive process; thus, a two-loop control system was required, where the inner loop (cycling at 500 Hz) was a PD control with compensation of interaction forces between the robot and both surgeon’s and patient’s tissues, while the stiffness of the robot was defined by the outer loop (cycling at 60-100 Hz) [38]. Thus, only a really simple boundary could be used.

Recently, Kikuuwe *et al.* proposed a new method for limiting access to a safe region in such a way that no energy is stored [41], in order to assure the stability of the system according to the passivity theory [15]. Their approach allows users to penetrate inside forbidden regions, thus providing surgeons with more autonomy. They introduced *plasticity-based virtual fixtures*, where the “*user can distinguish the direction in which the tool should not move before it actually starts to move*” [41]. The technique was proposed for both one-dimensional and multi-dimensional surfaces, and can be

2. ROBOTIC KNEE CHONDROPLASTY

implemented in both admittance-type and impedance-type robots. Yen and Davies applied a modified version of the *active constraints technique* in their TKA robot; the stiffness was increasing according to a jerk-free function and an algorithm for decreasing the milling velocity when the cutting forces exceeded a threshold value was implemented [90].

While Ho *et al.* (and following works) introduced *active constraints technique* for limiting access to some regions, Bettini *et al.* used this technique for helping the surgeon to move according to a preoperative plan, in both reaching tasks (*i.e.* directing movements to a target point) and tracking tasks (*i.e.* constraining movements on a reference curve in the space) [10, 19]. Moreover, it is possible to constrain movements inside a tube or inside a cone for guiding the user to a target point gradually, instead of limiting motions on a line [11]. Force applied by the user can be subdivided into one component parallel and another one orthogonal to the reference direction. The orthogonal component can then be constrained more or less hardly, setting appropriate parameters; the more the orthogonal component is constrained, the more the robot exhibits an anisotropic behaviour. Marayong *et al.* proposed a tuning rule, where parameters were chosen in order to reduce the execution time or the error or a weighted combination of both speed and accuracy [54].

Active constraints technique introduced by Bettini *et al.* was improved in order to constrain the motion not only on a line, but also on a preferred surface or volume by defining new projection operators for subdividing the force exerted by the user into two components [55]. This technique was implemented on a teleoperated system, where two impedance-type robots were used at both the master and the slave side [2]. Moore *et al.* introduced a similar approach for confining movements of an Arm Cobot on a line or above a surface, by introducing a function for defining the continuously variable transmission ratio; both position and aligning errors were taken into account [59].

However, all the above-mentioned approaches are limited to correlating the Cartesian end-effector linear velocity with the end-effector interaction forces, defining a (3×3) admittance matrix A:

$$\begin{bmatrix} v_x \\ v_y \\ v_z \end{bmatrix} = A_{(3 \times 3)} \begin{bmatrix} f_x \\ f_y \\ f_z \end{bmatrix} \quad (2.2)$$

which is evaluated considering the distance between the end-effector position and the boundary of the forbidden region if *active constraints* are used for limiting surgeon's

2. ROBOTIC KNEE CHONDROPLASTY

motion [37], or considering the direction connecting the end-effector position to the closest point on the preferred movement path if active constraints are exploited for guiding the surgeon [10]. A (6×6) admittance matrix could be evaluated instead, when a robot with 6 (or more) DoFs is used in order to correlate linear and angular velocities to both end-effector interaction forces and torques.

Unified approaches, where *active constraints* are used for guiding movements while avoiding collisions, have been developed. Turro *et al.* used *active constraints* for avoiding collisions between a PUMA 560 Robot and the environment and for avoiding singular configurations, while constraining the end effector to move on a curve or above a surface [82]. In their work they did not consider only the end-effector, but the whole manipulator structure, approximated by 72 triangles. Although the amount of triangles was really small, they still had to verify collisions asynchronously: considering a really simple environment modelled by 26 triangles, the collision detection module could not cycle faster than 200 Hz. The OBBTree interference detection algorithm was used, where every object is approximated by a set of *oriented bounding boxes* using a computationally expensive process ($O(n \log^2 n)$). Moreover, the algorithm can only determine whether two objects collide or not, without providing a measure of the distance between these objects if there is no interference [25].

Li *et al.* applied *active constraints technique* in sinus surgery, for helping the surgeon to move on a planned trajectory and for avoiding collisions between the whole instrument and the sinus cavity, which was modelled upon a CT image [48]. The approach proposed by Marayong *et al.* [55] was applied for constraining the surgeon's motion on a planned curve, while introducing an algorithm for evaluating the distance between different parts of the instrument and the patient's tissue; thus, this information is used as an optimization criterion for solving the inverse kinematic problem. The algorithm can be used in both a hands-on and a master-slave approach. However, the algorithm used for finding the distance between different objects is claimed to be too slow for being used in a real scenario [70].

It is worth noticing that none of the above-mentioned researches considered a minimally invasive procedure, where the RCM introduces an additional constraint.

In conclusion, *active constraints technique* can be used for:

2. ROBOTIC KNEE CHONDROPLASTY

1. Guiding the instruments along a preferred path;
2. Avoiding undesired injuries to bones or other tissues;
3. Confining the instrument to always pass through the trocar during the intervention.

2.5.1 Demands for Dynamic Active Constraints

Few researches were published about implementing *dynamic active constraints*, where boundaries of safe regions or planned curves are not fixed, but may vary in time, as it happen due to the cardiac motion or limb re-positioning, common during an arthroscopic procedure.

Ren *et al.* considered the cardiac motion of the heart for defining time-varying *active constraints*. The dynamic model of the heart was obtained interpolating a 4D MRI dataset, where 3D images were acquired using Electrocardiography (ECG)-gated imaging [70]. Based on the 3D time-varying model, *active constraints* were defined, and the model was registered with the patient (fluctuations in the heart beat rate can be taken into account using real-time ultrasound imaging and ECG for registering the model with the patient). Two different experiments were carried on: firstly, *active constraints* were used for limiting surgeon's movement when performing an incision, using a generalized sigmoid function to establish a virtual wall; secondly, *active constraints* were implemented for guiding the surgeon when performing tissue dissections, and a generalized Gaussian function was implemented for constraining the motion on an optimal curve.

Kwok *et al.* implemented *active constraints* for guiding a hyper-redundant snake-like robot on a planned curve around a beating heart. Risks of collisions were tracked and this information was used for exploiting advantageously the high number of redundant DoFs, in order to avoid interactions between the whole robot and the dynamic model of the heart [43, 45]. Kinaesthetic feedback was provided to the operator through a master device (PHANTOM Omni), in order to increase consistency between surgeon's and snake-like robot's movements [44].

It is worth noticing that the orthopaedic scenario avoids the bottleneck caused by the need of a real-time modelling with fast meshing adaptation under the rapid changes

2. ROBOTIC KNEE CHONDROPLASTY

of tissues morphology, since tissues deformations can be ignored due to the high stiffness of bones and other tissues involved in arthroscopic procedures.

However, re-positioning of the limb may become necessary during surgery [65, 68], thus requiring real-time registration between the pre-operative model and the patient, whose motion can be tracked with optical tracking systems using appropriate markers. Using tracking systems, movements of the knee can be monitored, and the surgical instrument may follow automatically the limb motion.

2.6 Conclusions

In this Chapter, several arthroscopic procedures have been review. Only abrasion chondroplasty and laser chondroplasty have been reported to be effective. However, while abrasion chondroplasty requires high contact forces for mechanically ablating the tissue, no direct contact is required for laser chondroplasty, that represents the best candidate for a robotic system for arthroscopy with flexible probes, since the light source can be transmitted through thin flexible optical fibres.

Neither commercial solutions nor research platforms have been developed so far for robotic-assisted chondroplasty. However, analysing the state of the arts of orthopaedic robots, it is possible to understand that a semi-active cooperative solutions with a hands-on approach might represent the best solution for such an application, having the highest acceptability among surgeons and allowing to achieve better outcomes, when compared to master-slave orthopaedic robotic systems.

The Active Constraints technique can be used for limiting the motion of a point within a pre-defined region, evaluating a (3×3) admittance matrix, which relates the interaction force and the robot end-effector velocity. However, when performing a minimally invasive procedure, other constraints should be considered, such as the remote centre of motion constraint.

In the next Chapter, the Active Constraints technique will be extended for constraining both position and orientation of a laparoscopic instrument, formulating a (6×6) impedance matrix, in order to deal with the other constraints of MIS. An algorithm for adapting this high-dimensional Active Constraints during limb-repositioning will be presented in Chapter 4.

Chapter 3

6 Dimensions Active Constraints

3.1 Introduction

For dealing with the constraints of a minimally invasive procedure, the orientation of the instrument has to be constrained in order to maintain the instrument to always pass through the incision point. Moreover, when considering chondroplasty, the layer of the tissue that has to be ablated is relatively thin; thus, the instrument tip should be constrained within a pre-defined region for increasing the safety of the solution.

For addressing these problems, a modified version of the Virtual Fixture law, as introduced in Bettini *et al.* [10, 11], and quoted in (2.2), will be proposed in this thesis.

The constraint on the orientation of the instrument limits its motion within a double cone. If the centre of the conical shape is corresponding to the trocar position, the instrument will always pass through the trocar point, not creating damages to the patient, as shown in Fig. 3.1. However, the conical constraint can also be used for dealing with the reduced space within the knee joint, as shown in Fig. 3.2. It is worth noticing that the trocar position can be easily update during the operation, thus reducing drastically the setup time when limb repositioning occurs (see Section 4.2).

The stability of the system will be investigated exploiting a unique feature of the FRI, which allows to analyse the behaviour of the robot when a frequency-known disturbance is introduced.

3. 6 DIMENSIONS ACTIVE CONSTRAINTS

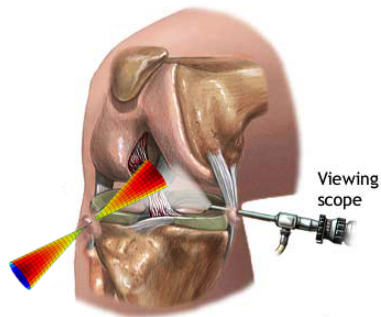


Figure 3.1: Constraining the instrument to pass through the trocar point -
When the centre of the conical motion is chosen accordingly to the trocar position, the instrument is constrained to pass through the trocar point.

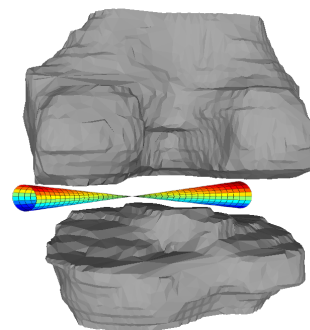


Figure 3.2: Dealing with the reduced room within the joint - The proposed technique for constraining the motion within a cone can be used for dealing with the reduced space within the joint.

3. 6 DIMENSIONS ACTIVE CONSTRAINTS

3.2 Impedance control for high-dimension constraints

An impedance matrix with dimension of (6×6) will be considered, which relates the end-effector linear $v_{(3 \times 1)}$ and angular $\omega_{(3 \times 1)}$ velocity to the end effector control force $f_{(3 \times 1)}$ and moment $\mu_{(3 \times 1)}$, defined in the Cartesian space:

$$\begin{bmatrix} f_{(3 \times 1)} \\ \mu_{(3 \times 1)} \end{bmatrix} = \begin{bmatrix} G_{(3 \times 3)}^{v,f} & G_{(3 \times 3)}^{\omega,f} \\ G_{(3 \times 3)}^{v,\mu} & G_{(3 \times 3)}^{\omega,\mu} \end{bmatrix} \begin{bmatrix} v_{(3 \times 1)} \\ \omega_{(3 \times 1)} \end{bmatrix} \quad (3.1)$$

where the impedance matrix was split in four (3×3) sub-matrices $G^{i,j}$, relating the i element to the j one.

In the lower half of the impedance matrix, sub-matrices $G^{v,\mu}$ [$N \cdot s$] and $G^{\omega,\mu}$ [$N \cdot m \cdot s/rad$] determine the constraint imposed on the instrument orientation. In the upper half of the impedance matrix, sub-matrices $G^{v,f}$ [$N \cdot s/m$] and $G^{\omega,f}$ [$N \cdot s/rad$] will be defined so that the surgeon's movements will be constrained within a pre-planned path or surface.

A rigid instrument attached to the end effector of the LWR will be considered. Two reference frames will be introduced; the first frame (x_b, y_b, z_b) is defined having the z axis parallel to the instrument axis, the y axis pointing through the robot end-effector and the centre of the frame located at the proximal end of the instrument longitudinal axis; the second frame (x_c, y_c, z_c) is chosen with the same orientation of the previous one, but centred in the instrument tip. These reference frames are shown in Fig. 3.3, where the reference frame (x_a, y_a, z_a) is the LWR end-effector reference frame, defined by KUKA.

The homogeneous transformation matrices are defined as:

$${}^aT_b = \begin{bmatrix} 1 & 0 & 0 & 0 \\ 0 & 0 & 1 & \Delta z \\ 0 & -1 & 0 & \Delta y \\ 0 & 0 & 0 & 1 \end{bmatrix} \quad {}^bT_c = \begin{bmatrix} 1 & 0 & 0 & 0 \\ 0 & 1 & 0 & 0 \\ 0 & 0 & 1 & L \\ 0 & 0 & 0 & 1 \end{bmatrix} \quad (3.2)$$

where aT_c and bT_c describe, respectively, the transformations from the reference frame (x_a, y_a, z_a) to the reference frame (x_b, y_b, z_b) , and from the reference frame (x_b, y_b, z_b) to the reference frame (x_c, y_c, z_c) . The distances Δy and Δz are shown in Fig. 3.3, and the value L is the length of the instrument shaft.

The proposed technique is also capable of constraining the motion of a flexible instrument, as shown in Chapter 4.

3. 6 DIMENSIONS ACTIVE CONSTRAINTS

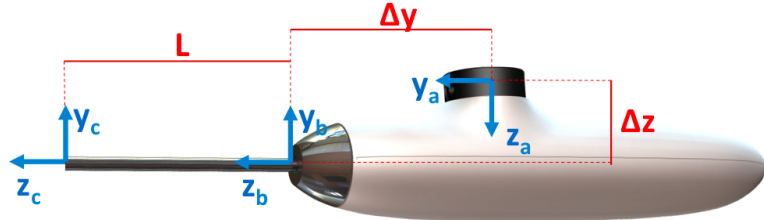


Figure 3.3: Definition of reference frames for the rigid instrument - The parameters L , Δy and Δz have been double-checked using the LWR calibration tool.

3.2.1 Orientation constraints

The conical motion has to be derived in order to restrict the instrument to pass through the incision point. However, this method can be trivially extended to the problem of spatial constraints due to the articular space within the knee cavity, by considering the centre of the conical motion as the point where the transversal section to the instrument axis is the smallest.

The trocar position ${}^0 p_T$, defined in the robot base reference frame, can be considered a known parameter. A method for deriving the position implicitly is presented in Section 5.3. Limb re-positioning can be taken into account, as illustrated in Section 4.2.2. The distance λ between the proximal end of the rigid shaft of the flexible instrument and the trocar point can be expressed as follow:

$$\lambda = \| {}^0 p_T - {}^0 p_b \| \quad (3.3)$$

where the points ${}^0 p_T$ and ${}^0 p_b$ are respectively the trocar position and the origin of the (x_b, y_b, z_b) frame, *i.e.* the proximal end of the rigid shaft, as shown in Fig. 3.3. The unitary vector r connecting these two points is obtained as:

$$r = \frac{1}{\lambda} ({}^0 p_T - {}^0 p_b) \quad (3.4)$$

Once the unitary vector r is known, both linear and angular velocity v_b and ω_b of the reference frame (x_b, y_b, z_b) can be decomposed into two components. The components v_{\parallel} and ω_{\parallel} parallel to r have not to be constricted by the trocar point. The other components v_{\perp} and ω_{\perp} , perpendicular to r , have to be constrained for avoiding further tissues damages around the incision point. The decomposition is conducted by the following equations:

$$v_{\parallel} = (rr^T)v_b \quad v_{\perp} = v_b - v_{\parallel} = (I_3 - rr^T)v_b \quad (3.5)$$

3. 6 DIMENSIONS ACTIVE CONSTRAINTS

$$\omega_{\parallel} = (rr^T)\omega_b \quad \omega_{\perp} = \omega_b - \omega_{\parallel} = (I_3 - rr^T)\omega_b \quad (3.6)$$

where I_3 is the (3×3) identity matrix.

The linear velocity perpendicular to the rigid instrument direction relate to the trocar position, denoted $v_{RCM,\perp}$, has to be null in order to maintain the instrument passing through the trocar position. Thus, it is possible to define a proper value ω^* for the component of the angular velocity such that:

$$\omega^* : v_{RCM,\perp} = v_{\perp} + \omega^* \times \lambda r = 0 \quad (3.7)$$

The component of the angular velocity ω^* has to be perpendicular to both the linear velocity v_{\perp} and to the unitary vector r , and its magnitude should be such that (3.7) is true. Thus, the angular velocity component ω^* can be evaluated as:

$$\omega^* = -\frac{\|v_{\perp}\|}{\lambda} \frac{r \times v_{\perp}}{\|r \times v_{\perp}\|} \quad (3.8)$$

By introducing the (3×3) matrix $[r]_{\times}$ corresponding to the cross-product $(r \times \bullet)$ ¹, (3.8) can be written as ($\|[r]_{\times}\| = 1$):

$$\omega^* = -\frac{\|v_{\perp}\|}{\lambda} \frac{[r]_{\times} v_{\perp}}{\|[r]_{\times}\| \|v_{\perp}\|} = -\frac{1}{\lambda} [r]_{\times} v_{\perp} = -\frac{1}{\lambda} [r]_{\times} (I_3 - rr^T) v_b \quad (3.10)$$

Consequently, the angular velocity component $\tilde{\omega}$:

$$\tilde{\omega} = \omega_{\perp} - \omega^* = (I_3 - rr^T)\omega_b + \frac{1}{\lambda} [r]_{\times} (I_3 - rr^T) v_b \quad (3.11)$$

can be considered as an error, and a proportional controller with the control moment μ as introduced in (3.1) can be introduced in order to reduce it. Defining with k_{μ} the gain of the proportional controller, the following control law, relating the control moment μ with the angular velocity error $\tilde{\omega}$ can be established:

$$\mu = k_{\mu} \tilde{\omega} \quad (3.12)$$

Thus, considering (3.1), (3.11) and (3.12), the following impedance sub-matrices can be evaluated:

$$G^{v,\mu} = \frac{k_{\mu}}{\lambda} [r]_{\times} (I_3 - rr^T) \quad (3.13)$$

¹ The matrix can be defined as follow:

$$r = \begin{bmatrix} r_x \\ r_t \\ r_z \end{bmatrix} \rightarrow [r]_{\times} = \begin{bmatrix} 0 & -r_z & r_y \\ r_z & 0 & -r_x \\ -r_y & r_x & 0 \end{bmatrix} \quad (3.9)$$

3. 6 DIMENSIONS ACTIVE CONSTRAINTS

$$G^{\omega,\mu} = k_\mu(I_3 - rr^T) \quad (3.14)$$

considering the linear velocity v and the angular velocity ω introduced in (3.1) as the linear velocity and the angular velocity of the (x_b, y_b, z_b) frame (*i.e.* $v = v_b$, and $\omega = \omega_b$).

3.2.2 An alternative implementation technique

The proposed technique has two major drawbacks so far:

1. Numerical differentiation has to be used for obtaining angular velocity, thus introducing noise. Digital filtering might be applied (as Infinite Impulse Response, IIR), but it will increase the delay, potentially leading to an unstable behaviour.
2. The orientation, expressed in Roll-Pitch-Yaw (RPY) angles $\Phi = [\varphi; \vartheta; \psi]^T$ at the instant time t will be equal to (being Δt the discretisation time interval):

$$\Phi(t) = \Phi(t_0) + \int_{t_0}^t \dot{\Phi}(\tau) d\tau = \Phi(t_0) + \Delta t \sum_{k=0}^t \dot{\Phi}(k) + e_\Phi(t) \quad (3.15)$$

where the *drift error* term:

$$e_\Phi(t) = \int_{t_0}^t \dot{\Phi}(\tau) d\tau - \Delta t \sum_{k=0}^t \dot{\Phi}(k) \quad (3.16)$$

will increase, due to the time discretisation, since no compensation strategies have been introduced.

A different way for implementing the proposed technique, overcoming to both these problems, will now be introduced. The RPY velocity $\dot{\Phi}$ and the angular velocity ω are related by the representation transformation matrix $T(\Phi)$ as follows [6]:

$$\omega = T(\Phi)\dot{\Phi} \quad T(\Phi) = \begin{bmatrix} 0 & -\sin(\varphi) & \cos(\varphi) \cos(\vartheta) \\ 0 & \cos(\varphi) & \sin(\varphi) \cos(\vartheta) \\ 1 & 0 & -\sin(\vartheta) \end{bmatrix} \quad (3.17)$$

If the angular velocity error $\tilde{\omega}$, as defined in (3.11), is fully constrained, the orientation Φ at the instant $k + 1$ will be equal to (using a RPY representation):

$$\Phi_{k+1} = \Phi_k + T(\Phi)^{-1}(\omega_b - \tilde{\omega})\Delta t = \Phi_k + \underbrace{T(\Phi)^{-1}\omega^*\Delta t}_{\text{Compensation}} + \underbrace{T(\Phi)^{-1}\omega_\parallel\Delta t}_{\text{Rotation}} \quad (3.18)$$

3. 6 DIMENSIONS ACTIVE CONSTRAINTS

where $T(\Phi)$ is the transformation matrix introduced in (3.17), Δt is the discretisation time interval, ω_b is the angular velocity of the reference frame (x_b, y_b, z_b) , ω^* is the component of the angular velocity compatible with the trocar constraint and ω_{\parallel} is the component of the angular velocity parallel to the instrument shaft (still compatible with the trocar constraint).

The term “*Rotation*” ($T(\Phi)^{-1}\omega_{\parallel}\Delta t$) represents a rotation around the instrument rigid shaft axis, while the term “*Compensation*” ($T(\Phi)^{-1}\omega^*\Delta t$) represents a compensatory movement carried on in order to make the instrument always pass through the trocar point (the angular velocity ω^* is perpendicular to both the unitary vector r and the linear velocity component v_{\perp} , as defined in (3.8)).

The motion of the instrument from the time instant k (red configuration in Fig. 3.4 and Fig. 3.5) to the time instant $k + 1$ (green configuration in Fig. 3.4 and Fig. 3.5) can be considered as composed of two sub-motions: a *translation* perpendicular to the instrument axis from the time instant k to the time instant k^* (light grey configuration in Fig. 3.4 and Fig. 3.5), and a following rotation (*compensation*) from the instant time k^* to the instant time $k + 1$.

When moving from the time instant k to k^* , a translation of vdt is performed perpendicular to the direction z_b . When moving from the configuration k^* to the configuration $k + 1$ a rotation of an angle α in the plane defined by z_b and r around the point P_b (centre of the reference frame (x_b, y_b, z_b)) is performed, so that the instrument will pass through the trocar point P_T .

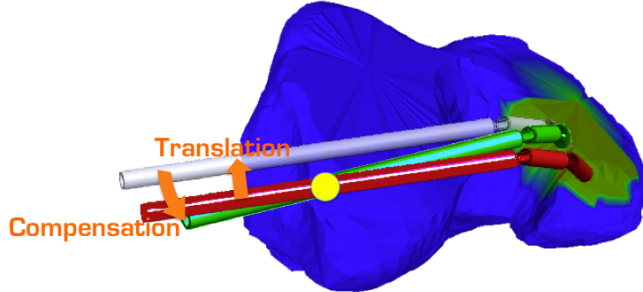


Figure 3.4: Instrument motion due the conical motion constraint - The *compensation* makes the instrument pass through the trocar position (yellow circle).

The “*Compensation*” is thus equivalent to a rotation of an angle α around an axis a . Considering Fig. 3.5, the unitary vector \hat{a} representing the direction of the axis a

3. 6 DIMENSIONS ACTIVE CONSTRAINTS

can be defined as:

$$\hat{a} = \frac{z_b \times r}{\|z_b \times r\|} \quad (3.19)$$

while the rotation angle α is related to the z axis of the reference frame (x_b, y_b, z_b) at the time instant k^* ¹ and the unitary vector r defined in (3.4), by the following equations (trigonometric consideration shown in Fig. 3.5):

$$\begin{cases} \sin(\alpha) = \|z_b \times r\| \\ \cos(\alpha) = z_b^T \cdot r \end{cases} \quad (3.20)$$

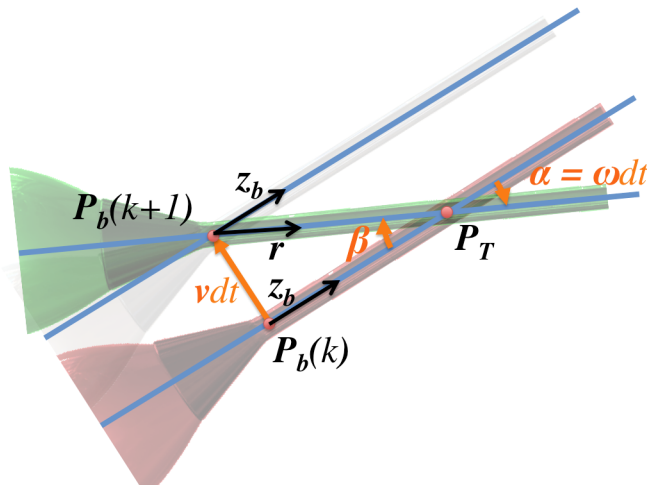


Figure 3.5: Decomposition of the instrument motion due to the conical constraint - It is possible to show that, the amplitude of the angle α is equal to $\|\omega^*\|dt$ under some assumptions.

Since the vector z_b , the unitary vector r and the component of the linear velocity perpendicular to the instrument axis v_\perp are all in the same plane, and considering (3.8) and (3.19), it can easily find out that:

$$\hat{a} = \frac{z_b \times r}{\|z_b \times r\|} = \frac{r \times v_\perp}{\|r \times v_\perp\|} = \frac{\omega^*}{\|\omega^*\|} = \hat{\omega}^* \quad (3.21)$$

where $\hat{\omega}^*$ represents the direction of the angular velocity ω^* . Moreover, the following approximation can be performed when assuming that the time interval dt is small:

$$v_\perp dt = \lambda \tan(\beta) \approx \lambda \beta \quad (3.22)$$

¹Since from the time instant k to the time instant k^* only a translation is performed, $z_b(k^*) = z_b(k)$.

3. 6 DIMENSIONS ACTIVE CONSTRAINTS

(the distance λ is defined in (3.3) and β is the angle between z_b and r , as shown in Fig. 3.5). Since angles α and β are vertically opposite, they are equal to each other. Thus, considering (3.8), the following relationship can be formulated as:

$$\alpha = \frac{v_\perp}{\lambda} dt = \|\omega^*\| dt \quad (3.23)$$

In conclusion, it has been shown that the “Compensation” ($\omega^* dt$), introduced in (3.24) and the rotation of the angle α (as evaluated in (3.23)) around the unitary vector \hat{a} (as evaluated in (3.21)) are equivalent for $dt \ll 1$ (otherwise, the approximation introduced in (3.22) can not be considered as true), since they are rotations of the same angle around the same axis. Thus, the “Compensation” can be evaluated as an axis-angle rotation matrix ${}^0R_a(\alpha)$ [75]:

$${}^0R_a(\alpha) = \begin{bmatrix} a_x^2(1 - c_\alpha) + c_\alpha & a_x a_y (1 - c_\alpha) - a_z s_\alpha & a_x a_z (1 - c_\alpha) + a_y s_\alpha \\ a_x a_y (1 - c_\alpha) + a_z s_\alpha & a_y^2(1 - c_\alpha) + c_\alpha & a_y a_z (1 - c_\alpha) - a_x s_\alpha \\ a_x a_z (1 - c_\alpha) - a_y s_\alpha & a_y a_z (1 - c_\alpha) + a_x s_\alpha & a_z^2(1 - c_\alpha) + c_\alpha \end{bmatrix} \quad (3.24)$$

where $[a_x; a_y; a_z]^T$ are the components of the \hat{a} unitary vector, and s_α and c_α are the sine and the cosine of the α angle.

Thus, the orientation Φ_{k+1} in the RPY representation for the time instant $k+1$ can be evaluated as:

$$\Phi_{k+1} = \Phi_k^* + \underbrace{T(\Phi)^{-1} \omega_{\parallel} \Delta t}_{\text{Rotation}} \quad (3.25)$$

where Φ_k^* is the RPY representation of the rotation matrix ${}^0R_k^*$, defined as follows¹:

$$\Phi_k^* \leftrightarrow {}^0R_k^* = {}^0R_a(\alpha) {}^0R_k \quad (3.26)$$

being the rotation matrix R_k the matrix equivalent to the RPY representation Φ_k of the orientation at the time instant k ².

¹The matrix ${}^0R_a(\alpha)$ is pre-multiplied because it is a rotation defined in the base fixed reference frame.

² Rotation matrix and RPY angles are related by the following equations [75]:

$$R = \begin{bmatrix} r_{11} & r_{12} & r_{13} \\ r_{21} & r_{22} & r_{23} \\ r_{31} & r_{32} & r_{33} \end{bmatrix} \rightarrow \Phi(R) = \begin{bmatrix} \varphi \\ \vartheta \\ \psi \end{bmatrix} = \begin{bmatrix} \text{atan2}(r_{21}, r_{11}) \\ \text{atan2}(-r_{31}, r_{11}c_\varphi + r_{21}s_\varphi) \\ \text{atan2}(r_{13}s_\varphi - r_{23}c_\varphi, r_{22}c_\varphi - r_{12}s_\varphi) \end{bmatrix} \quad (3.27)$$

$$\Phi(R) = \begin{bmatrix} \varphi \\ \vartheta \\ \psi \end{bmatrix} \rightarrow R(\Phi) = \begin{bmatrix} c_\varphi c_\vartheta & c_\varphi s_\vartheta s_\psi - s_\varphi c_\psi & c_\varphi s_\vartheta c_\psi + s_\varphi s_\psi \\ s_\varphi c_\vartheta & s_\varphi s_\vartheta s_\psi + c_\varphi c_\psi & s_\varphi s_\vartheta c_\psi - c_\varphi s_\psi \\ -s_\vartheta & c_\vartheta s_\psi & c_\vartheta c_\psi \end{bmatrix} \quad (3.28)$$

3. 6 DIMENSIONS ACTIVE CONSTRAINTS

Considering now the “*Rotation*” term, as introduced in (3.24), it represents a rotation of an angle $\|\omega_{\parallel}\|dt$ around the instrument shaft, *i.e.* the z_b axis of the (x_b, y_b, z_b) frame. Thus, the orientation Φ_{k+1} for the time instant $k+1$ can be defined as the RPY equivalent representation of the rotation matrix ${}^0R_{k+1}$, defined as:

$$\Phi_{k+1} \leftrightarrow {}^0R_{k+1} = {}^0R_k^{*b}R_z(\gamma) = {}^0R_a(\alpha){}^0R_k^bR_z(\gamma) \quad (3.29)$$

being the rotation matrix ${}^0R_k^*$ defined in (3.26), and ${}^bR_z(\gamma)$ the rotation matrix around the z axis of the reference frame (x_b, y_b, z_b) of an angle γ . For evaluating the angle γ , it is possible to consider a proportional *viscous* relationship between the momentum applied by the surgeon in the direction parallel to the instrument axis μ_{\parallel}^s and the desired component of the angular velocity parallel to the instrument axis ω_{\parallel} . Being b the viscous proportional coefficient, the following equations can be evaluated:

$$\|\mu_{\parallel}^s\| = b\|\omega_{\parallel}\| \leftrightarrow \mu_{\parallel}^s = (rr^T)\mu^s \quad (3.30)$$

where the unitary vector r is defined in (3.4) and μ_s is the total momentum applied by the surgeon to the instrument. Introducing a new viscous coefficient $b^* = bdt$, the angle γ can be evaluated as follow:

$$\gamma = \|\omega_{\parallel}\|dt = \frac{\|\mu_{\parallel}^s\|}{b^*} \quad (3.31)$$

The desired orientation Φ_{k+1} at the time instant $k+1$, as evaluated in (3.29), is the reference orientation for the robot at time instant $k+1$ in order to constrain its motion in a conical shape.

The proposed implementation method introduces three main advantages with respect to the active constraints technique based on the formulation of the impedance matrix as defined in (3.1), (3.13) and (3.19), *i.e.:*

1. No velocity estimation is required, thus avoiding numerical derivation, which introduces noise and inaccuracy in the control system.
2. Drift error is compensated, since the reference position is evaluated once at every cycle.

Notation s_{α} and c_{α} denote respectively the sine and cosine operators applied to the angle α , as evaluated in (3.20).

3. 6 DIMENSIONS ACTIVE CONSTRAINTS

3. Orientation accuracy for rotation around the instrument rigid shaft axis can be possibly improved by using an external and more accurate force/torque sensor.

However, it is worth noticing that these two formulations for constraining the orientation of the instrument are equivalent only under the following assumptions:

1. The cycle time should be small enough to have the approximation (3.22) valid.
2. The direct relationship in (3.30) is valid.

In order to fulfil to the second assumption, the rotation around the instrument rigid shaft axis will not be performed using the LWR, but it will be integrated in the flexible device introduced in Chapter 4. The LWR orientation will be then controlled using the value Φ_{k+1} defined in (3.29) as reference orientation.

3.2.3 Prescription of surgical path

The surgeon can define a path (or a surface, as shown in Chapter 5), where his motion has to be constrained on, in order to avoid damages to other tissues. This feature represents an interesting advantage of robotic systems for arthroscopy, since pre-operative images can be used for *guiding* the surgeon within a predefined region and for defining *no-fly zones*, where the surgeon should not be allowed to penetrate into. However, chondroplasties are generally performed without having a patient specific model (defined by CT or MRI images); thus, a generic model might also be used, which has to adapt to the patient's specificity using intra-operative information, such as laser-scanning data or reconstruction from endoscopic video.

Without loss of generality, a surface can be defined implicitly in the 3D space by the function $g()$:

$$g(x, y, z) = 0 \quad (3.32)$$

where x , y , and z are the coordinates of the points, defined in the robot base frame. If the unitary vector $n(x, y, z)$ representing the normal to the surface for each point satisfying the equation (3.32) is known, the linear velocity \dot{p}_c of the tip of the laparoscopic instrument (*i.e.* the linear velocity of the centre of the reference frame (x_c, y_c, z_c) as defined in Fig. 3.3), can be decomposed in two components, one parallel to the surface (\dot{p}_{\parallel}) and one perpendicular to the surface (\dot{p}_{\perp}):

$$\dot{p}_{\perp} = (nn^T)\dot{p}_c \quad \dot{p}_{\parallel} = \dot{p}_c - \dot{p}_{\perp} = (I_3 - nn^T)\dot{p}_c \quad (3.33)$$

3. 6 DIMENSIONS ACTIVE CONSTRAINTS

If the surgeon's motion has to be constrained on the surface $g(x, y, z) = 0$, the component of the velocity \dot{p}_\perp perpendicular to it has to be considered as an error, since only the component \dot{p}_\parallel parallel to the surface is compatible with the proposed constraint. Thus, a proportional controller can be introduced, relating the robot control force f , as introduced in (3.1), to the error \dot{p}_\perp on the linear velocity \dot{p}_c of the reference frame (x_c, y_c, z_c) . Defining with k_p the controller gain, the following control law can be introduced:

$$f = k_f \dot{p}_\perp = k_f (nn^T) \dot{p}_c \quad (3.34)$$

The linear velocity \dot{p}_c is related to the linear and angular velocity of the reference frame (x_b, y_b, z_b) (v_b and ω_b , respectively) by the following equation:

$$\dot{p}_c = v_b + \omega_b \times (L \cdot z_b) \quad (3.35)$$

being L the length of the rigid shaft (as shown in Fig. 3.3), and z_b the unitary vector representing the z axis of the reference frame (x_b, y_b, z_b) , defined in the robot base frame. However, if the instrument is constrained to perform a conical motion, it is possible to assume that $z_b = r$, being r the unitary vector defined by (3.4). Thus, using the matrix $[r]_\times$ equivalent to the cross-product $r \times \blacksquare$, as defined in (3.9), the control law (3.34) can be written as¹:

$$f = k_f (nn^T) v_b - k_f L (nn^T) [r]_\times \omega_b \quad (3.36)$$

Thus, considering (3.36), the impedance sub-matrices $G^{v,f}$ and $G^{\omega,f}$ introduced in (3.1) can be specified as:

$$G^{v,f} = k_f (nn^T) \quad (3.37)$$

$$G^{\omega,f} = k_f L (nn^T) [r]_\times \quad (3.38)$$

In conclusion, considering (3.13), (3.19), (3.37) and (3.37), the impedance matrix (3.1) can be evaluated as:

$$\begin{bmatrix} f \\ \mu \end{bmatrix} = \begin{bmatrix} k_f (nn^T) & k_f L (nn^T) [r]_\times \\ \frac{k_\mu}{\lambda} [r]_\times (I_3 - rr^T) & k_\mu (I_3 - rr^T) \end{bmatrix} \begin{bmatrix} v_b \\ \omega_b \end{bmatrix} \quad (3.39)$$

where:

\mathbf{f}, μ Control force and torque, respectively

¹Being $a \times b = -b \times a$.

3. 6 DIMENSIONS ACTIVE CONSTRAINTS

v_b, ω_b Linear and angular velocity of the reference frame (x_b, y_b, z_b), respectively, defined in the robot base frame (see Fig. 3.3)

k_f, k_μ Proportional gains of the controllers for the control force and torque, respectively

L Length of the rigid shaft (see Fig. 3.3)

λ Distance between the proximal end of the rigid shaft (centre of the reference frame (x_b, y_b, z_b)) and the centre of the conical motion constraint

n Unitary vector representing the normal to the pre-planned surface

r Unitary vector connecting the proximal end of the rigid shaft (centre of the reference frame (x_b, y_b, z_b)) and the centre of the conical motion constraint

[r]_× (3 × 3) matrix equivalent to the cross-product $r \times \blacksquare$

I₃ (3 × 3) identity matrix

3.2.4 Reduction of drift error

The drawbacks introduced in Section 3.2.2 are presented also when the position is constrained using the linear velocity as input; the derivation of velocity from position measures requires the usage of filtering, that may bring to an unstable behaviour due to the introduced delays. Moreover, if the velocity \dot{p}_\perp in the direction perpendicular to the surface is not fully constrained, the surgeon's motion will not be limited on the surface, since the *drift error* $e_p(t) = \int_{t_0}^t \dot{p}(\tau) d\tau - \Delta t \sum_{k=0}^t \dot{p}(k)$ (being p the position of the tool tip, see (3.16)) is not reduced by compensation strategies.

An alternative method will be now proposed for overcoming these problems. The task of following a pre-planned path will be considered in this paragraph, and the technique will be extended in Chapter 5 for constraining the motion on a pre-planned surface defined implicitly.

It is possible to consider an elastic relationship between the effective position p_c^e of the tool tip and the control force f (representing the force that the robot is exerting):

$$f = k(p_c^d - p_c^e) + D \quad (3.40)$$

3. 6 DIMENSIONS ACTIVE CONSTRAINTS

being k a diagonal (3×3) gain matrix [N/m], p_c^d the desired position for the tool tip and D a proper set (3×1) damping vector. For constraining the position of the tool tip on a path, it is possible to consider as the desired position the closest point on the path to the actual position of the tool tip; thus, indicating with $C = \{c_1, \dots, c_m\}$ the ordered set of points defining the pre-planned path on a 3D space, the control law can be defined as:

$$f = k(c^* - p_c^e) + D \quad \text{where} \quad c^* \in C : \|c^* - p_c^e\| < \|c - p_c^e\| \quad \forall c \in C (c \neq c^*) \quad (3.41)$$

being c^* the closest point to the tool tip within the pre-planned surface. The surgeon will feel the force field applied by the robot, represented in Fig. 3.6. Without loss of generality, this picture represents the force field on a planar section of the 3D space (being all the points of the pre-planned path within this planar section).

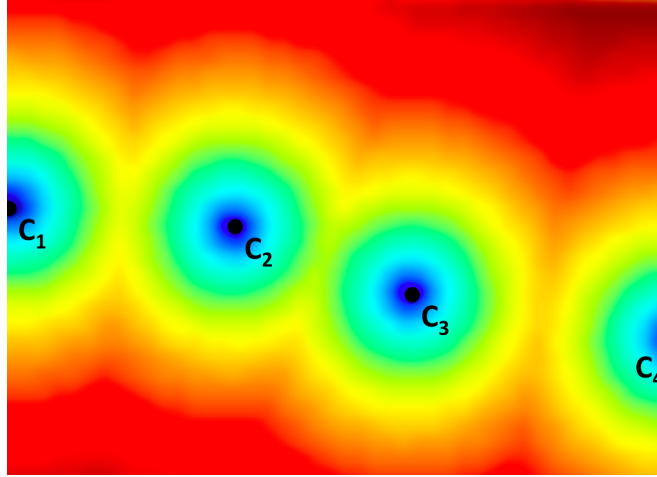


Figure 3.6: Force felt by the surgeon when constraining his motion on a pre-planned surface - The force felt by the operator increases when shifting from blue to red.

The surgeon should not feel any force when moving on the pre-planned surface; thus, given a set of m point C defining the pre-planned path, the points should be interpolated to define a new set $C' = \{c'_1, \dots, c'_n\}$ ($n \geq m$) such as the distance between two following points is lower than a threshold value, identified with ϵ :

$$C = \{c_1, \dots, c_m\} \xrightarrow{\text{interpolation}} C' = \{c'_1, \dots, c'_n\} : \forall c'_i, c'_{i+1} \in C' \quad \|c'_i - c'_{i+1}\| \leq \epsilon \quad (3.42)$$

3. 6 DIMENSIONS ACTIVE CONSTRAINTS

and the closest point c^* should then be defined within the set $C' = \{c'_1, \dots, c'_n\}$, instead of the set $C = \{c_1, \dots, c_m\}$.

The maximum distance ϵ and the gain matrix k introduced in (3.40) have to be defined; considering all the elements on the diagonal of the k matrix equal each other, it is possible to introduce some criteria.

The following values can be introduced:

HF High force value, *i.e.* the force that the operator should consider as “hard constraint”

δ Maximum displacement, *i.e.* the distance from the surface where the operator should experience an haptic interaction equal to HF

LF Low force value, *i.e.* the maximum force that the robot will exert due to the interpolation resolution when the surgeon is following the pre-planned path or is on the pre-planned surface

ρ^* Maximum path curvature

γ Maximum angle of tangent and chord, see Fig. 3.7

χ Maximum angle of tangent and chord factor, see below

In order to define the desired stiffness k , the following criteria should be considered:

1. The desired stiffness has to be upper-limited by the maximum stiffness that the robot can exert¹;
2. The operator should feel a force attracting him to the pre-planned path or surface equal to HF when the distance from it is equal to δ ;
3. The maximum curvature of the surface has to be considered, in order to avoid sudden “jumps”.

¹The LWR can exert a maximum stiffness of 5000 N/m. However, due to safety consideration, a maximum value of 4000 N/m will be considered.

3. 6 DIMENSIONS ACTIVE CONSTRAINTS

Considering the condition (2), the following equation can be derived according to the Hooke's law:

$$f = k \cdot \delta \geq HF \rightarrow k \geq \frac{HF}{s} \quad (3.43)$$

being f the force exerted by the robot when the distance between the tool tip and the closest point within the path is equal to δ .

For evaluating the curvature of a path, three consecutive points can be considered. These three points c_i, c_{i+1}, c_{i+2} define a triangle that is inscribed in a circle having the following diameter d :

$$d = \frac{a \cdot b \cdot c}{2 \cdot \Delta} \quad (3.44)$$

where a, b and c represents the length of the three edges of the triangle, and Δ its area. Thus, the curvature ρ of the circle (equal to the inverse of its radius) can be evaluated as follow:

$$\rho = \frac{2}{d} = \frac{4 \cdot \Delta}{a \cdot b \cdot c} \quad (3.45)$$

or, considering the Heron's formula:

$$\rho = \frac{\sqrt{(a+b+c)(-a+b+c)(a-b+c)(a+b-c)}}{a \cdot b \cdot c} \quad (3.46)$$

If the surgeon is experiencing a high force (equal to HF) when he is in the centre of the circle, and supposing that this force is high enough to assure that the surgeon will not go further away, the following condition is sufficient for avoiding sudden "jumps" between two diametrically opposite points with respect to the centre of curvature:

$$F = \frac{k}{\rho^*} \geq HF \rightarrow k \geq HF \cdot \rho^* \quad (3.47)$$

where ρ^* is the maximum curvature characterising the path.

However, this condition will not introduce any constraint on possible "jumps" between two points that are not diametrically opposite. Thus, the surgeon will still be able to move on a chord (different from the diameter), since he will not experience a force equal to HF , which is supposed to completely limit his motion. Thus, a condition on the maximum tangent and chord angle (see Fig. 3.7) for limiting the amplitude of the "jumps" can be introduced.

If the surgeon will experience the hard constraint when he is at a distance equal to r/χ , where r is the inverse of ρ^* (*i.e.* it is the radius corresponding to the maximum

3. 6 DIMENSIONS ACTIVE CONSTRAINTS

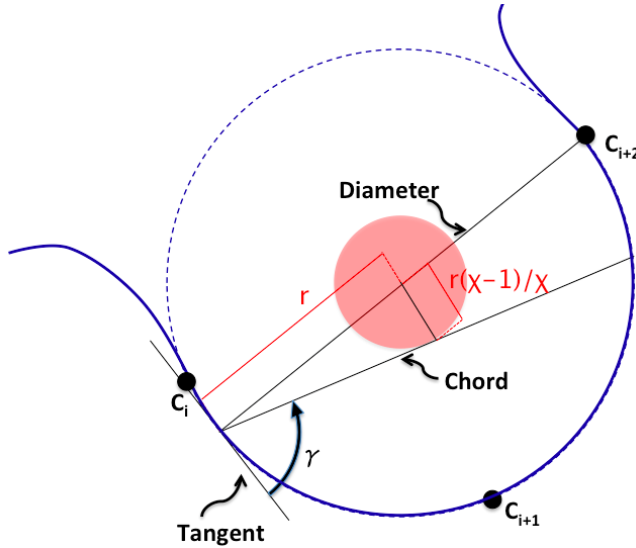


Figure 3.7: Definition of the maximum tangent to chord angle parameter - The high level force HF should be perceived at a distance r/χ for avoiding the surgeon to penetrate in the red circle.

curvature) and $\chi > 1$ is an adimensional factor, he will be able to move on chords that will not cross the red circle of Fig. 3.7, which radius is equal to $r \cdot (\chi - 1)/\chi$.

Thus, the factor χ can be related to the desired maximum tangent and chord angle γ (see Fig. 3.7). When the surgeon is moving with the maximum tangent and chord angle, his trajectory will be tangent to the red circle. Thus, due to trivial geometrical consideration:

$$\sin\left(\frac{\pi}{2} - \gamma\right) = \frac{r}{r} \left(\frac{\chi - 1}{\chi} \right) \quad (3.48)$$

and the maximum angle of tangent and chord factor χ can be derived as (Fig. 3.8):

$$\chi = \frac{1}{1 - \sin\left(\frac{\pi}{2} - \gamma\right)} \quad (3.49)$$

Thus, the condition (3.47) can be updated with the following:

$$F = \frac{k}{\rho^* \chi} \geq HF \rightarrow k \geq HF \cdot \rho^* \chi \quad (3.50)$$

By and large, considering (3.43) and (3.50), the stiffness k can be defined by the following equation:

$$k = \min \left\{ 4000, \max \left\{ \frac{HF}{s}, \frac{HF}{\rho^* \chi} \right\} \right\} \quad (3.51)$$

3. 6 DIMENSIONS ACTIVE CONSTRAINTS

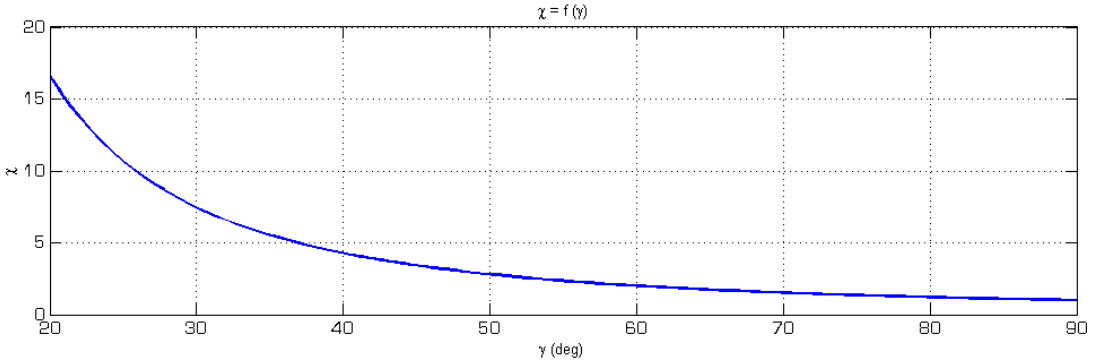


Figure 3.8: Maximum angle of tangent and chord factor - The parameter χ limits surgeon's movements, defining the maximum tangent and chord angle.

being 4000 the maximum stiffness, according to safety limits.

Once the k value was defined, the distance ϵ between two close points should be such that the maximum force experienced by the operator is lower than LF . Since the maximum force exerted to the surgeon's hand is equal to $k \cdot \epsilon/2$, when he is moving along the pre-planned path, the value of ϵ is defined by the following equation:

$$F = k \cdot \frac{\epsilon}{2} \leq LF \rightarrow \epsilon \leq \frac{2 \cdot LF}{k} \quad (3.52)$$

Considering the values quoted in Table 3.1, the following relationships can be evaluated:

Table 3.1: Suggested values for defining the robot stiffness and the interpolation lattice grid dimension.

Parameter	Value
HF	15 N
δ	5 mm
LF	0.2 N ¹
γ	60°

$$k = \begin{cases} 3000 \text{ N/m} & \rho^* < 100 \text{ 1/m} \\ 30 \text{ N} \cdot \rho^* & 100 \text{ 1/m} \leq \rho^* < 133.3 \text{ 1/m} \\ 4000 \text{ N/m} & \rho^* \geq 133.3 \text{ 1/m} \end{cases} \quad (3.53)$$

¹This value has been determined as the desired resolution for MIS [80].

3. 6 DIMENSIONS ACTIVE CONSTRAINTS

$$\epsilon = \begin{cases} 0.133 \text{ mm} & \rho^* < 100 \text{ 1/m} \\ \frac{0.0133}{\rho^*} & 100 \text{ 1/m} \leq \rho^* < 133.3 \text{ 1/m} \\ 0.1 \text{ mm} & \rho^* \geq 133.3 \text{ 1/m} \end{cases} \quad (3.54)$$

For interpolating the ordered series of points $C = \{c_1, \dots, c_m\}$ defining the pre-planned path, the Catmull spline interpolation technique can be used, in order to assure the interpolated path to pass through all the control points. According to the Catmull spline interpolation technique, the path $c(t)_{i,i+1}$ between the points c_i and c_{i+1} is defined by the following polynomial:

$$c(t)_{i,i+1} = a_3 t^3 + a_2 t^2 + a_1 t + a_0 \quad t \in [0; 1] \quad \begin{cases} a_0 = (2c_i)/2 \\ a_1 = (-c_{i-1} + c_{i+2})/2 \\ a_2 = (2c_{i-1} - 5c_i + 4c_{i+1} - c_{i+2})/2 \\ a_3 = (-c_{i-1} + 3c_i - 3c_{i+1} + c_{i+2})/2 \end{cases} \quad (3.55)$$

being t the curvilinear abscissa, defined between 0 and 1 (for $i = 1$, it is possible to assume $c_{i-1} = c_1$, while for $i = m - 1$ it is possible to assume $c_{i+2} = c_m$). Thus, the path is fully described by the set:

$$C(t) = \bigcup_{i=1}^{m-1} c(t)_{i,i+1} \quad (3.56)$$

However, the path has to be defined by a series of points $C' = \{c'_1, \dots, c'_j, \dots, c'_n\}$ $n \geq m$, that should be equally spaced with a distance of ϵ , as defined in (3.52). Thus, each point c'_j ($j = 1 \dots n$) of the path $C(t)$, has to be evaluated in correspondence to proper values of the curvilinear abscissa $T_{i,i+1} = \{t_{1,(i,i+1)}, \dots, t_{j,(i,i+1)}, \dots, t_{w,(i,i+1)}\}$, being w the number of points evaluated between c_i and c_{i+1} . The series of values for the curvilinear abscissa $T_{i,i+1} = \{t_{1,(i,i+1)}, \dots, t_{j,(i,i+1)}, \dots, t_{w,(i,i+1)}\}$ has to be defined such as:

$$\|c_{i,i+1}(t_{j+1,(i,i+1)}) - c_{i,i+1}(t_{j,(i,i+1)})\| = \epsilon \quad (3.57)$$

The increment $\Delta t_{j,(i,i+1)}$ between $t_{j+1,(i,i+1)}$ and $t_{j,(i,i+1)}$ can be defined, such as:

$$t_{j+1,(i,i+1)} = t_{j,(i,i+1)} + \Delta t_{j,(i,i+1)} \quad (3.58)$$

Thus, for $\Delta t_{j,(i,i+1)} \ll 1$, the Taylor's theorem can be applied:

$$\begin{aligned} c_{i,i+1}(t_{j+1,(i,i+1)}) &= c_{i,i+1}(t_{j,(i,i+1)} + \Delta t_{j,(i,i+1)}) = \\ &= c_{i,i+1}(t_{j,(i,i+1)}) + \frac{dc_{i,i+1}(t)}{dt} \Big|_{t_{j,(i,i+1)}} \Delta t_{j,(i,i+1)} + o(\Delta t_{j,(i,i+1)}) \end{aligned} \quad (3.59)$$

3. 6 DIMENSIONS ACTIVE CONSTRAINTS

where $dc_{i,i+1}(t)/dt|_{t_{j,(i,i+1)}}$ is the derivate of the polynomial (3.55), evaluated for $t = t_{j,(i,i+1)}$.

Considering (3.57) and (3.59), the increment $\Delta t_{j,(i,i+1)}$ is related to the maximum distance ϵ by the following equations:

$$\epsilon = \|c_{i,i+1}(t_{j+1,(i,i+1)}) - c_{i,i+1}(t_{j,(i,i+1)})\| \approx \frac{dc_{i,i+1}(t)}{dt} \Big|_{t_{j,(i,i+1)}} \Delta t_{j,(i,i+1)} \quad (3.60)$$

Thus, the series $T_{i,i+1} = \{t_{1,(i,i+1)}, \dots, t_{j,(i,i+1)}, \dots, t_{w,(i,i+1)}\}$ can be represented by the following relationship:

$$t_{j+1,(i,i+1)} = t_{j,(i,i+1)} + \frac{\epsilon}{\frac{dc_{i,i+1}(t)}{dt} \Big|_{t_{j,(i,i+1)}}} \quad \begin{cases} t_{1,(i,i+1)} = 0 \\ t_{j,(i,i+1)} \leq 1 \quad \forall j = 1, 2, \dots, w \end{cases} \quad (3.61)$$

When the application of the equation (3.61) provides a value for $t_{j+1,(i,i+1)} > 1$, it means that all the required points between c_i and c_{i+1} on the path $c(t)_{i,i+1}$ have been evaluated. However, a residual distance $d_{r,i+1} < \epsilon$ can be evaluated:

$$d_{r,i+1} = \|c_{i+1} - c_{i,i+1}(t_{w,(i,i+1)})\| \quad (3.62)$$

representing the distance between the last point of the interpolated series on the path $c(t)_{i,i+1}$ and c_{i+1} . Thus, the following point should have a distance equal to $\epsilon - d_{r,i+1}$ from c_{i+1} . This point will be evaluated on the path defined between the points c_{i+1} and c_{i+2} , i.e. on the path $c(t)_{i+1,i+2}$. Thus, the first element within the series $T_{i+1,i+2} = \{t_{1,(i+1,i+2)}, \dots, t_{j,(i+1,i+2)}, \dots, t_{w,(i+1,i+2)}\}$ should be defined such as:

$$\|c_{i+1,i+2}(t_{1,(i+1,i+2)}) - c_{i+1}\| = \epsilon - d_{r,i+1} \quad (3.63)$$

and considering that $c_{i+1} = c(0)_{i+1,i+2}$, it is possible to evaluate $t_{1,(i+1,i+2)}$ as:

$$t_{1,(i+1,i+2)} = \frac{\epsilon - d_{r,i+1}}{\frac{dc_{i,i+1}(t)}{dt} \Big|_0} \quad (3.64)$$

In conclusion, considering (3.61) and (3.64), given the set of points $C = \{c_1, \dots, c_m\}$, the path can be defined interpolating the given points with the Catmull spline interpolation $C(t)$ introduced in (3.56), and evaluating the points $C' = \{c'_1, \dots, c'_n\}$ ($n \geq m$)

3. 6 DIMENSIONS ACTIVE CONSTRAINTS

in correspondence to the following $t_{j,(i,i+1)}$ values:

$$t_{j,(i,i+1)} = \begin{cases} 0 & \text{for } i = 1; \quad j = 1 \\ \frac{\epsilon - d_{r,i+1}}{\left. \frac{dc_{i,i+1}(t)}{dt} \right|_0} & \text{for } 1 < i \leq m-1; \quad j = 1 \\ t_{j-1,(i,i+1)} + \frac{\epsilon}{\left. \frac{dc_{i,i+1}(t)}{dt} \right|_{t_{j-1,(i,i+1)}}} & \text{for } 1 < i \leq m-1; \quad j > 1 \end{cases} \quad (3.65)$$

The force field due to the interpolated path $C' = \{c'_1, \dots, c'_m\}$ ($m \geq n$) is shown in Fig. 3.9. The operators **do not** feel significant forces when moving along the path.

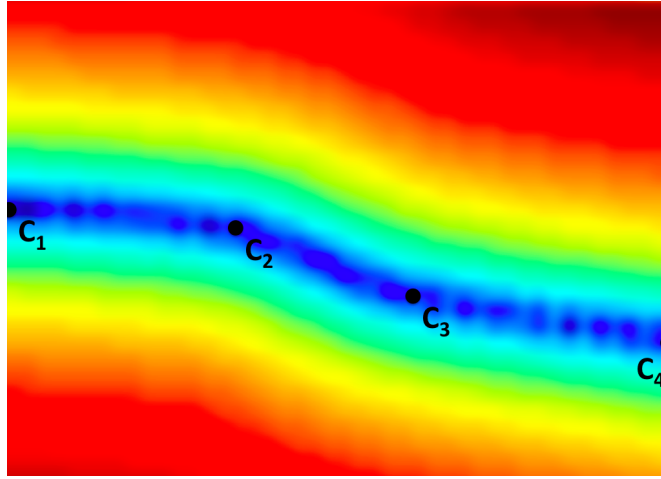


Figure 3.9: Force felt by the surgeon when constraining his motion on a pre-planned surface after the Catmull spline Interpolation - The force felt by the operator increases when shifting from blue to red.

Thus, the active constraint technique proposed in (3.34) and following equations, can be alternatively implemented considering the control law (3.41) for small cycle times. It is reasonable to assume that at the time instant k the tool tip is on the pre-planned path in the position $p_{c,k}^e$. If the component \dot{p}_\perp of the velocity perpendicular to the trajectory is fully constrained at the instant k , the instrument tip will move on the tangent of the trajectory nearby the position of the instrument tip in k . Thus, if the path is defined by the Catmull spline interpolation, as in (3.56), the tangent to the trajectory in k is defined by the derivative of the polynomial defining the trajectory, *i.e.* $\frac{dC(t)}{dt}|_{C(t)=c_k}$. Thus, at the time instant $k+1$, the position occupied by the trajectory

3. 6 DIMENSIONS ACTIVE CONSTRAINTS

$p_{c,k+1}^e$ will be defined by:

$$p_{c,k+1}^e = p_{c,k}^e \pm \frac{dC(t)}{dt} \Big|_{C(t)=c_k} \|v_{\parallel}\| \quad (3.66)$$

being $\|v_{\parallel}\|$ the component of the velocity parallel to the path and being the sign \pm dependant on the direction of motion (positive if the instrument tip is moving accordingly to the order set $C = \{c_1, \dots, c_m\}$, and negative otherwise). Without loss of generality, we can assume $\|v_{\parallel}\| = 1$, since this value affects the equation of motion and **not** the trajectory.

If the cycle time is small enough, it is possible to approximate the discrete (3.66) with its continuous form:

$$p_c^e(\tau) = p_{c,k}^e + \int_{t_k}^{t^*} \frac{dC(t)}{d\theta} d\theta = p_{c,k}^e + C(t^*) - C(t_k) = C(t^*) \quad (3.67)$$

where $p_c^e(\tau)$ the position of the tool tip at the time τ , $C(t_k)$ is the position on the path equivalent to the position of the instrument in k (having supposed that the robot is on the path at the beginning of the motion, thus $\exists t_k : p_{c,k}^e = c(t_k)$), and $t^* \in T = \cup_{i=1}^{m-1} T_{i,i+1}$ an appropriate value within the series T (union of the series $T_{i,i+1}$ defined in (3.65)).

Having demonstrated that the motion is constrained on a preplanned path, it is obvious that:

$$\exists t^* \in T : \|p_c^e(\tau) - c(t^*)\| = 0 \quad (3.68)$$

Since the path defined by $c(t)$ has been interpolated with the series $C' = \{c'_1, \dots, c'_n\}$, the point within $C' = \{c'_1, \dots, c'_n\}$ that best fits the equation (3.68) is the closest point to the instrument tip c^* , as defined in (3.41).

Thus, choosing the reference position c^* as the closest point on the path to the tool tip, is equivalent to defining an appropriate parameter for $t \in T$, being T the series defined in (3.65). In other words, it is equivalent to defining an approximated equation of motion introducing a mapping between the temporal data $p_c(\tau)$ and the elements in the series $C' = \{c'_1, \dots, c'_n\}$.

In conclusion, it has been demonstrated that the two control laws are equivalent, under the assumption of small cycle time.

3. 6 DIMENSIONS ACTIVE CONSTRAINTS

3.2.5 Implementation on the FRI

The techniques introduced in Sections 3.2.2 and 3.2.4 have been implemented in the FRI. The FRI provides the user with the homogeneous transformation matrix representing the pose of a point within the end effector (the programmer can define the preferred point by defining the appropriate transformation matrix). The robot can then be controlled defining the desired stiffness in the Cartesian space and the reference pose for the predefined point within the end effector (by defining the reference transformation matrix).

The coordinate frame (x_b, y_b, z_b) has been chosen as the reference frame.

Thus, once the pre-planned path is defined by the ordered set $C' = \{c'_1, \dots, c'_i, \dots, c'_n\}$ and the position of the centre of the conical motion 0p_T is acquired (the position can be tracked in real-time, as shown in Section 4.2), the algorithm for controlling the robot is shown in the pseudo-code 3.1.

Algorithm 3.1 Implementation of the high-dimensional *implicit active constraints* law

- 1: Read the homogenous transformation matrix 0T_b
- 2: Read the trocar position 0p_T
- 3: Evaluate the pose of the distal part of the end effector as ${}^0T_c = {}^0T_b {}^bT_c$
- 4: Search for the closest point $c^* \in C'$ to the instrument tip
- 5: Evaluate the unitary vector r connecting the distal end of the laparoscopic instrument to the trocar position (see (3.4))
- 6: Evaluate the rotation matrix ${}^0R_{k+1}$ for the desired orientation as described in (3.29)
- 7: Evaluate the homogeneous transformation matrix for the distal end of the instrument as:

$${}^0T_{c,\text{ref}} = \begin{bmatrix} {}^0R_{k+1} & c^* \\ 0 & 0 & 0 & 1 \end{bmatrix} \quad (3.69)$$

- 8: The reference homogeneous transformation matrix for the proximal end of the rigid instrument is given by:

$${}^0T_{b,\text{ref}} = \begin{bmatrix} {}^0R_{k+1} & c^* - L \cdot r \\ 0 & 0 & 0 & 1 \end{bmatrix} \quad (3.70)$$

since references (x_b, y_b, z_b) and (x_c, y_c, z_c) have the same orientation, being the origin of the (x_b, y_b, z_b) reference frame translated of L in the direction $-r$ with respect to the (x_c, y_c, z_c) reference frame

3. 6 DIMENSIONS ACTIVE CONSTRAINTS

The stiffness value for the position k can be defined according to (3.51), and the stiffness for the orientation k_o can be defined accordingly as:

$$k_o = k \frac{k_o^{\max}}{k^{\max}} \quad (3.71)$$

being k^{\max} and k_0^{\max} the maximum value for the stiffness for position and orientation, respectively (equal to 5,000 N/m and 300 N · m/rad, respectively).

It has been assumed that the distal end of the end effector is on the pre-planned path at the starting position.

3.3 Validation of 6 DoFs Active Constraints algorithm

In order to validate the proposed algorithm, the robot was constrained to follow the arbitrary path described by the equation (referring to the reference frame (x_b, y_b, z_b)):

$$x_{b,\text{ref}}(t) = \begin{bmatrix} x_0 + A_x \frac{t}{t_{\max}} \\ y_0 \\ z_0 + A_z \sin\left(2\pi\alpha \frac{t}{t_{\max}}\right) \end{bmatrix} \quad (3.72)$$

composed by a linear motion in the x direction (total distance: A_x), and a sinusoidal motion in the z direction (A_z : semi-amplitude of the motion, α : number of oscillation performed during the path), being x_0 , y_0 and z_0 the coordinates of the starting position, t_{\max} represents the completion time, and $t \in [0; t_{\max}]$ the time instant. While following the preplanned trajectory, the orientation was constrained to have the instrument passing through the trocar point, evaluating the proper rotation matrix according to (3.26) (rotation around the z_b axis was not considered).

For a straight instrument, the intra-corporeal position of the distal part of the laparoscopic instrument x_{intra} (as defined in (3.75)) and the extra-corporeal position of the proximal part x_{extra} (as defined in (3.79)) are related by simple geometrical considerations. Being r the unitary vector representing the direction of the laparoscopic instrument defined in (3.4), and L the length of the instrument as shown in Fig. 3.3, the intra-corporeal position is related to the extra-corporeal according to the following equation:

$$x_{\text{intra}}(t) = x_{\text{extra}}(t) + Lr \quad (3.73)$$

while the orientation is the same for both proximal and distal parts.

3. 6 DIMENSIONS ACTIVE CONSTRAINTS

Aim of this experiment is trying to follow the same trajectory under several conditions and introducing a frequency-known disturbance, in order to evaluate the stability of the system and to check whether the stiffness of the robot has to be limited for rejecting an external disturbance. Thus, it would be useful to follow the exact same trajectory several times, while varying the stiffness and the frequency of the disturbance. The FRI allows the programmer to simulate an external operator (as shown in Section 3.3.1), in order to test the behaviour of the system under several known conditions. A sinusoidal motion will be considered in the y direction, representing an external disturbance, with a varying frequency, for analysing the margin of stability of the system while modifying the stiffness parameters.

3.3.1 Simulation of external forces

The dynamic of a manipulator in presence of an external interaction can be represented by the following equation [75]:

$$B(q)\ddot{q} + n(q, \dot{q}) = \tau_{\text{contr}} + J^T(q)h_u \quad (3.74)$$

being $B(q)$ the inertia matrix, \ddot{q} the joint acceleration, τ_{contr} the control torque, $J(q)$ the Jacobian matrix of the manipulator, h_u the force exerted by the environment (or by the operator) to the manipulator and $n(q, \dot{q})$ a vector representing the centrifugal and Coriolis forces, the friction forces and the gravity vector.

When considering a PD controller in the operational space with dynamic compensation, the control torque can be defined as:

$$\tau_{\text{contr}}^{\text{PD}} = J^T(q) (k_c (x_{\text{ref}} - x_e)) + D(q) + f_{\text{dynamics}}(q, \dot{q}, \ddot{q}) \quad (3.75)$$

where k_c is a (6×6) impedance matrix, x_{ref} is the desired position and orientation of the end-effector, x_e is the effective position and orientation of the end-effector, $D(q)$ a damping vector and $f_{\text{dynamics}}(q, \dot{q}, \ddot{q})$ an additional torque for compensating the dynamic of the manipulator.

If the LWR is controlled through the FRI using the *Cartesian Stiffness control*, the control torque introduced in (1.1) can be defined. Considering (3.75), the control torque $\tau_{\text{contr}}^{\text{FRI}}$ can be defined as:

$$\tau_{\text{contr}}^{\text{FRI}} = J^T (k_c (x_d - x)) + D(d_c) + f_{\text{dynamics}}(q, \dot{q}, \ddot{q}) + J^T (F_{\text{ext}}) = \tau_{\text{contr}}^{\text{PD}} + J^T F_{\text{ext}} \quad (3.76)$$

3. 6 DIMENSIONS ACTIVE CONSTRAINTS

Considering (3.74) and (3.76), an external operator can be simulated by an interaction force $\overline{h_u}$, defining:

$$F_{ext} = \overline{h_u} \quad (3.77)$$

resulting in the following dynamic model:

$$B(q)\ddot{q} + n(q, \dot{q}) = \tau_{\text{contr}}^{\text{FRI}} + \underbrace{J^T(q)\overline{h_u}}_{\text{no real interaction}} = \tau_{\text{contr}}^{\text{PD}} + J^T\overline{h_u} \quad (3.78)$$

Thus, the operator can be modelled by a proper design of the force function $F_{ext} = \overline{h_u}$.

It is reasonable to assume that the operator will apply at the time instant k a force proportional to the difference between the extra-corporeal position that the operator wants to reach $x_{op}(t)$ and the effective extra-corporeal position $x_b(t)$ of the (x_b, y_b, z_b) frame (as introduced in Fig. 3.3), while the orientation will not be modified by the simulated operator, and it will be only constrained by the proposed active constraints technique:

$$\overline{h_u}(t) = \begin{bmatrix} K_{op}(x_{op}(t) - x_b(t)) \\ 0_{(3 \times 3)} \end{bmatrix} \quad (3.79)$$

where K_{op} is a (3×3) diagonal stiffness matrix (a stiffness value of 1000 N/m has been chosen for all the elements on the diagonal); according to this stiffness value, the operator applied an average force of 5.02 N (standard deviation: 1.41 N) for moving the instrument along the trajectory represented in Fig. 3.10, with a maximum value of 8.24 N .

However, the external force has to be defined in the LWR “tool” frame, *i.e.* it has to be represented in the frame (x_b, y_b, z_b) as shown in Fig. 3.3¹. The rotation matrix representing the orientation of the frame (x_b, y_b, z_b) with respect to the base frame 0R_B can be directly read from the FRI homogenous transformation matrix 0T_B . Given the force $\overline{h_u}(t)$ in the robot base frame, its equivalent formulation in the “tool” frame $F_{\text{ext}}^{\text{tool}}(t)$ is defined by [75]:

$$F_{\text{ext}}^{\text{tool}}(t) = \begin{bmatrix} {}^0R_B^T & 0 \\ 0 & {}^0R_B^T \end{bmatrix} \overline{h_u}(t) \quad (3.80)$$

¹The reference frame that will be used for defining the force is defined by the property “Stiffness.Frame” of the KRC.

3. 6 DIMENSIONS ACTIVE CONSTRAINTS

Adding the external force described by (3.79) and (3.80), the simulated external operator is able to move the robot on the path shown in Fig. 3.10, miming a real operator.

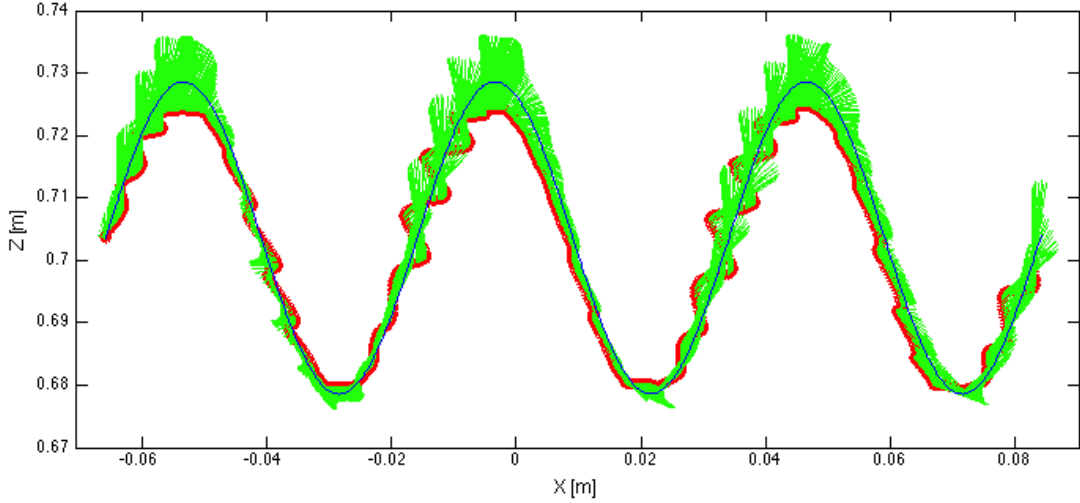


Figure 3.10: Simulation of an external operator - The desired path (blue) is approximated by the actual path (red). The green lines represent the force applied by the external operator.

For validating and analysing the proposed technique, a sinusoidal motion in the y direction, representing the disturbance, was added to the desired path (3.72). Thus, the reference position for the operator $x_{op}(t)$ is given by (in the robot base frame):

$$x_{op}(t) = x_{b,\text{ref}}(t) + \begin{bmatrix} 0 \\ A_y \sin(2\pi ft) \\ 0 \end{bmatrix} = \begin{bmatrix} x_0 + A_x \frac{t}{t_{\max}} \\ y_0 + A_y \sin(2\pi ft) \\ z_0 + A_z \sin\left(2\pi\alpha \frac{t}{t_{\max}}\right) \end{bmatrix} \quad (3.81)$$

being f the frequency of the sinusoidal motion, and A_y its semi-amplitude. The sinusoidal motion in the y direction has to be constrained by the proposed *active constraints* technique.

3.3.2 Experimental results

The robot was constrained to follow the preplanned trajectory using the proposed *active constraints* technique, while being moved by the simulated operator, as described in Section 3.3.1. Parameters were set according to Table 3.2. Motion was sampled at 100

3. 6 DIMENSIONS ACTIVE CONSTRAINTS

Hz. The frequency f of the disturbance was set equal to several values:

$$f = \{ 0.1 \ 0.2 \ 0.5 \ 1 \ 2 \ 5 \ 10 \} \text{ Hz} \quad (3.82)$$

The position stiffness k for the robot, as introduced in (3.51) was varied, while the orientation stiffness k_o was set accordingly according to (3.71):

$$k = \{ 10 \ 20 \ 50 \ 100 \ 200 \ 500 \ 1000 \ 2000 \} \text{ N/m} \quad (3.83)$$

Table 3.2: Parameters for the validation of the proposed *active constraints* technique.

Parameter	Value
A_x	150 mm
A_y	150 mm
A_z	250 mm
t_{\max}	20 s
α	3

The experiment was evaluated for all the possible combinations of frequency f and robot position stiffness k . The trocar was considered 30 cm below the reference frame (x_b, y_b, z_b) , as introduced in Fig. 3.3, in the direction of the z_b axis.

Two performances index were considered:

- **Position error** $e_p(t)$, defined as the distance between the actual position $x_b(t)$ at the time instant t and the desired position $x_{b,\text{ref}}(t)$ at the time instant t :

$$e_p(t) = \|x_b(t) - x_{b,\text{ref}}(t)\| \quad (3.84)$$

- **Orientation error** $e_o(t)$, defined as the distance between the trocar point and the instrument axis at the time instant t , evaluated as:

$$e_o(t) = \|z_b(t) \times (x_b(t) - p_T)\| \quad (3.85)$$

being $z_b(t)$ the direction of the instrument axis, $x_b(t)$ the position of the reference frame (x_b, y_b, z_b) as introduced in Fig. 3.3, and p_T the trocar point coordinates.

Results are plotted in Fig. 3.11 - 3.12.

3. 6 DIMENSIONS ACTIVE CONSTRAINTS

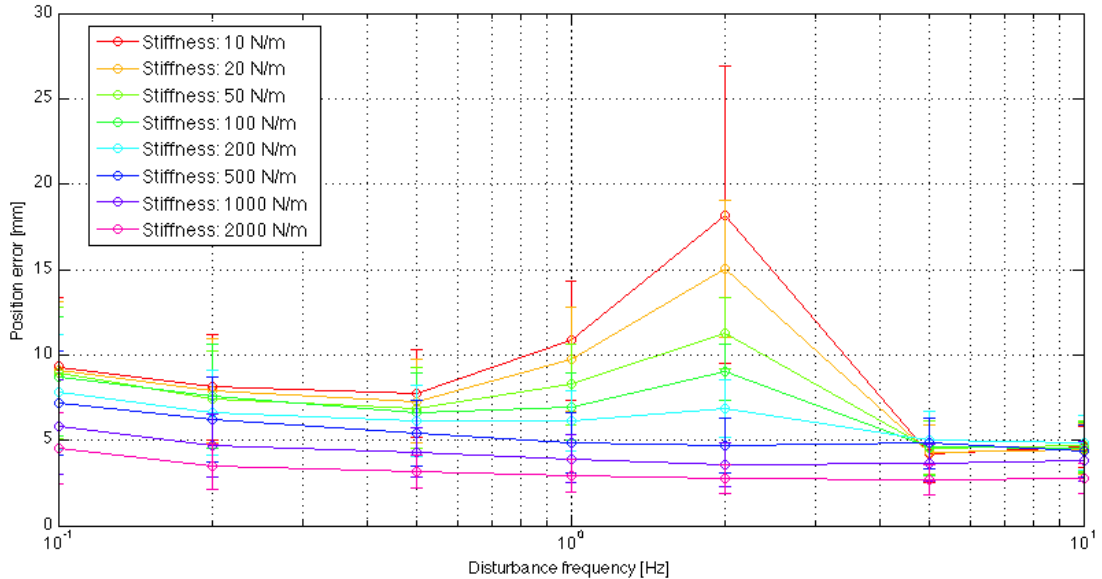


Figure 3.11: Mean value of the position error $e_p(t)$ - The mean value has been evaluated for all the combinations of frequency f and position stiffness k .

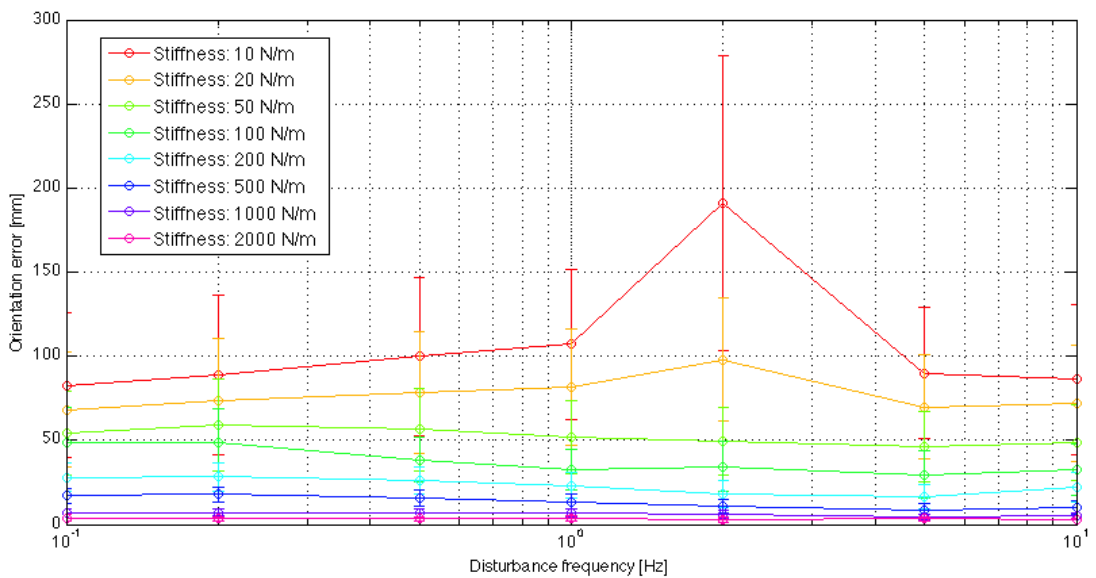


Figure 3.12: Mean value of the orientation error $e_o(t)$ - The mean value has been evaluated for all the combinations of frequency f and position stiffness k . The graph has been plotted considering the orientation stiffness k_o , evaluated according to (3.71).

3. 6 DIMENSIONS ACTIVE CONSTRAINTS

3.3.3 Discussions

For validating the proposed algorithm and analysing its stability, a simulated operator has been implemented exploiting some features of the FRI.

The robot is acting as a low-pass filter (due to its inertia), rejecting high frequency disturbance ($> 5 \text{ Hz}$). However, the effect of the disturbance is critical at 2 Hz , where it reaches a high value especially when low stiffness is applied.

Thus, a stability analysis should be carried on considering a disturbance of 2 Hz , supposing that if the system is stable for a 2 Hz disturbance, it will be stable for a disturbance of another frequency.

Thus, the same experiment was repeated considering a total time of 120 s . The amplitude of the oscillation in the y direction was recorded. The system is considered to be stable if the maximum amplitude of the sinusoidal motion is reducing during the task execution, while it is considered unstable otherwise.

The maximum amplitude was recorded in both the positive and negative y direction, and the trend of its value has been linearly interpolated. Thus, if the linear interpolation provides a positive slope, the system is considered unstable, while it is stable for a negative slope. Results are plotted in Fig. 3.13 for the negative y direction (similar results were found for the positive direction).

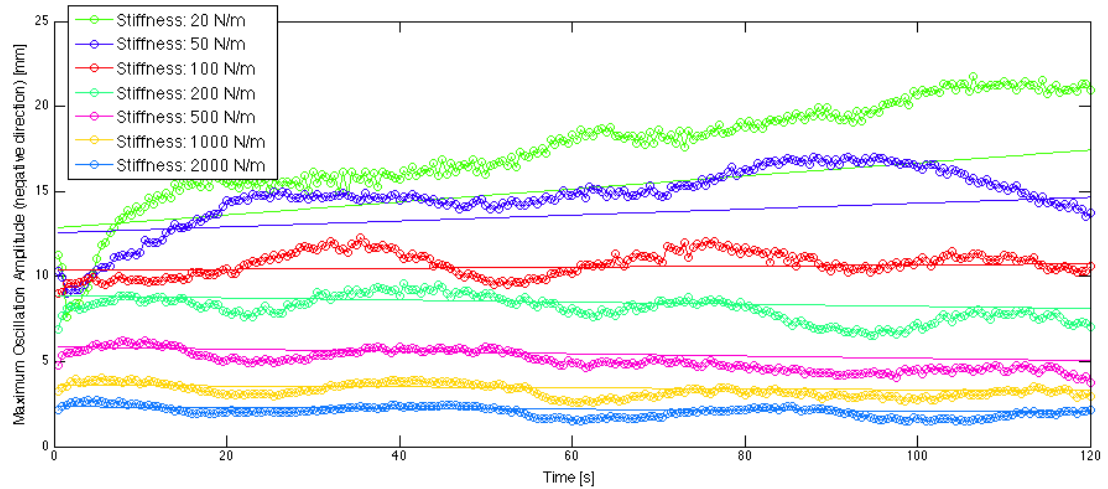


Figure 3.13: Analysis of the stability of the proposed control law - The maximum oscillations in the negative y direction are represented for different stiffness values. The lines represent the linear approximation of the maximum oscillations trends.

3. 6 DIMENSIONS ACTIVE CONSTRAINTS

The slope of the interpolating line can be considered as an index of the stability, that increases while increasing the stiffness k parameter: the system exhibits a stable behaviour for $k \geq 200 \text{ N/m}$ (slope = -0.0062 mm/s).

Considering the orientation error, its value decreases while increasing the orientation stiffness. For low orientation stiffness value ($k_0 \leq 6 \text{ N} \cdot \text{m/rad}$) the higher error is recorded for a disturbance frequency of 2 Hz. However, this has to be considered as a consequence of the low stiffness value for the position (since k and k_o are coupled by (3.71), for $k_0 \leq 6 \text{ N} \cdot \text{m/rad}$ the position stiffness value k is lower or equal to 100 N/m , and the robot exhibits an unstable behaviour). It is worth noticing that the mean error value can be limited to be smaller than 4 mm for the whole analysed frequency spectrum when the stiffness value k_o is equal to $120 \text{ N} \cdot \text{m/rad}$.

3.4 Conclusions

In this Chapter, a (6×6) impedance matrix has been proposed, for constraining the position on a pre-planned curve or surface (a technique for surface reconstruction will be presented in the next Chapter) and for constraining the orientation in order to have the instrument passing through the trocar point. However, for avoiding the numerical derivation of the velocity and reducing the drift error, an alternative implementation of the active constraints technique has been proposed. The two control laws have been demonstrated to be equivalent, under the assumption of small cycle time.

The proposed technique has been validated, introducing a simulated operator in order to analyse the system response for different frequency-known disturbances. **Safety** has to be considered as one of the major goal of a control system for surgery. In this Chapter the proposed active constraints law has been demonstrated experimentally to be stable, thus safe, for appropriate stiffness parameter.

In the following Chapter, a flexible instrument will be introduced, and the active control law will be enhanced for coping with a dynamic scenario.

All the parameters required for defining the constraints will be *implicitly* defined from the surgeon's first movements, as shown in Chapter 5, where a surface reconstruction algorithm will be proposed.

Chapter 4

Dynamic Active Constraints

4.1 Introduction

In the previous chapter, a 6 DoFs Active Constraints technique was introduced for constraining the instrument position and orientation; a static environment was supposed, *i.e.* no changes in the constraints, such as the trocar position and the pre-defined path, were considered. However, during an arthroscopic procedure, limb re-positionings might be required. Once the limb has been moved, the patient's knee has to be registered again within the operative theatre frame, where all the constraints are defined, in order to adapt the control law to the new environment, requiring long intra-operative setup times.

In Section 4.2, the Active Constraints technique introduced in Chapter 3 will be extended for dynamically adapting to the varying conditions of the environment; a tracking system will be introduced, for tracking the trocar position; thus, the constraint on the orientation of the instrument can be applied during limb re-positioning. A calibration algorithm for defining the relative position between the tracking system base frame and the robot base frame will be proposed and validated.

The constraint on the position of the tip of the laparoscopic instrument will not be dynamically adapted, but the surgeon will be required to redefine the control points each time he had moved the patient's limb. This represents a safety measurement, since a small error in the registration might lead to damage to the articular cartilage, due to the thin cartilage layer. However, only few control points are required, as it will be shown in Section 5.2.7.

4. DYNAMIC ACTIVE CONSTRAINTS

Moreover, for reducing the occurrence of re-positionings, a flexible instrument will be introduced in Section 4.3, for increasing both reachable and dexterous workspace. In addition, the flexible instrument will allow to achieve an optimal approach direction, having always the laser beam perpendicular to the surface, as shown in Section 4.3.2. The flexible instrument kinematics will be experimentally characterised in Sections 4.3.3 and 4.3.4.

4.2 Real-time tracking underdynamic environment

The *Polaris VICRA* Tracking System (Northern Digital Inc.¹, Fig. 4.1) is used for tracking the motion of the limb, requiring a marker composed of three optical reflective spheres. The marker is supposed to be rigidly attached to the trocar. Thus, the development of a customised marker rigidly connected to the trocar is envisaged.

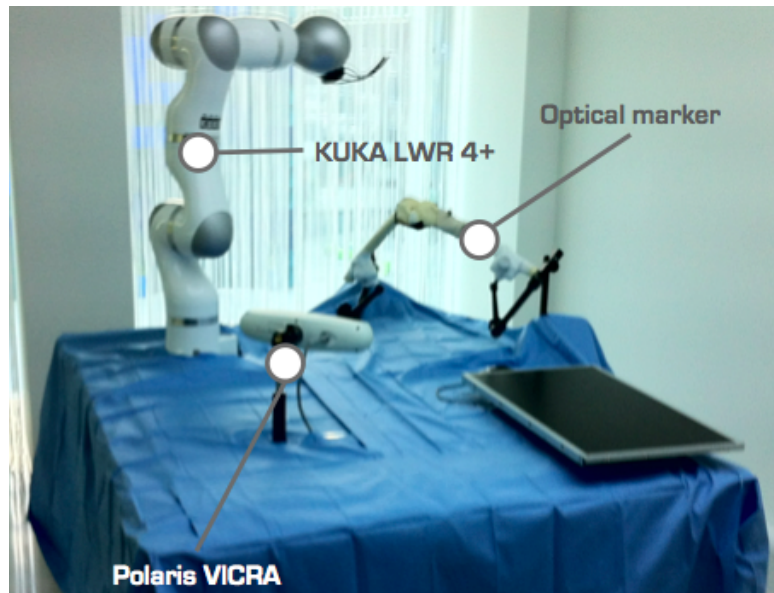


Figure 4.1: Introduction of a tracking system in the proposed setup - The *Polaris Vicra* is introduced for tracking the pose of a marker, rigidly connected to the knee phantom.

The relative position between the *Polaris VICRA* and the robot base frame has to be defined, as shown in Section 4.2.1. In Section 4.2.3 the controlling law during re-positioning is presented.

¹www.ndigital.com/medical/polarisfamily.php

4. DYNAMIC ACTIVE CONSTRAINTS

4.2.1 Calibration between tracking system and LWR.

The *Polaris VICRA* is able to provide the user with the homogenous transformation matrix pT_m , representing the position and orientation of a marker with respect to the tracking system reference frame, which can be represented as (x_p, y_p, z_p) . However, the relative pose of the *Polaris VICRA* reference frame (x_p, y_p, z_p) with respect to the robot base frame (x_0, y_0, z_0) has to be identified by evaluating the homogenous transformation matrix 0T_p .

For calibrating this matrix, a marker can be directly applied to the robot end-effector, so that the relative position between the marker and the frame (x_b, y_b, z_b) , as defined in Fig. 3.3, is constant, and can be represented by the homogenous transformation matrix mT_b . The position of the frame (x_b, y_b, z_b) (with respect to the robot base frame) can be either read directly from the FRI matrix 0T_b or evaluated from the information provided by the *Polaris VICRA* pT_m , as:

$${}^0T_b = {}^0T_p {}^pT_m {}^mT_b \quad (4.1)$$

The robot can then be moved while tracking its end-effector position, in order to acquire the temporal data ${}^0T_{b,k}$ from the FRI, and ${}^pT_{m,k}$ from the *Polaris VICRA*, where $k = 1, \dots, w$, being w the number of acquired samples. The matrix 0T_p and mT_b have to be defined (24 scalar unknowns, 12 for each matrix). The linear system:

$${}^0T_{b,k} {}^bT_m - {}^0T_p {}^pT_{m,k} = 0 \quad \text{where } {}^bT_m = ({}^mT_b)^{-1} \quad (4.2)$$

can be defined for each measurement (12 scalar equations). However, 6 additional non-linear constraints, have to be defined for each homogenous transformation matrix, in order to have orthogonal rotation matrices with determinant equal to 1. Considering the matrix 0T_p :

$${}^0T_p = \begin{bmatrix} {}^0T_{p,11} & {}^0T_{p,12} & {}^0T_{p,13} & {}^0T_{p,14} \\ {}^0T_{p,21} & {}^0T_{p,22} & {}^0T_{p,23} & {}^0T_{p,24} \\ {}^0T_{p,31} & {}^0T_{p,32} & {}^0T_{p,33} & {}^0T_{p,34} \\ 0 & 0 & 0 & 1 \end{bmatrix} \quad (4.3)$$

the following constraints have to be introduced:

$$\left\{ \begin{array}{l} {}^0T_{p,11} {}^0T_{p,11} + {}^0T_{p,21} {}^0T_{p,21} + {}^0T_{p,31} {}^0T_{p,31} - 1 = 0 \\ {}^0T_{p,12} {}^0T_{p,12} + {}^0T_{p,22} {}^0T_{p,22} + {}^0T_{p,32} {}^0T_{p,32} - 1 = 0 \\ {}^0T_{p,13} {}^0T_{p,13} + {}^0T_{p,23} {}^0T_{p,23} + {}^0T_{p,33} {}^0T_{p,33} - 1 = 0 \\ {}^0T_{p,11} {}^0T_{p,12} + {}^0T_{p,21} {}^0T_{p,22} + {}^0T_{p,31} {}^0T_{p,32} = 0 \\ {}^0T_{p,12} {}^0T_{p,13} + {}^0T_{p,22} {}^0T_{p,23} + {}^0T_{p,32} {}^0T_{p,33} = 0 \\ {}^0T_{p,13} {}^0T_{p,11} + {}^0T_{p,23} {}^0T_{p,21} + {}^0T_{p,33} {}^0T_{p,31} = 0 \end{array} \right. \quad (4.4)$$

4. DYNAMIC ACTIVE CONSTRAINTS

Likewise for the matrix bT_m .

After having evaluated the homogenous transformation matrices with a non-linear system solver, the rotation matrices can be orthogonalised in order to fully respect the constraints (4.4). After having evaluated 0T_p , the following equations can be applied (likewise for bT_m):

1. Normalise the third column of the rotation matrix:

$$[{}^0T_{p,13}, {}^0T_{p,23}, {}^0T_{p,33}]^T = \frac{[{}^0T_{p,13}, {}^0T_{p,23}, {}^0T_{p,33}]^T}{\| [{}^0T_{p,13}, {}^0T_{p,23}, {}^0T_{p,33}] \|} \quad (4.5)$$

2. Normalise the second column of the rotation matrix:

$$[{}^0T_{p,12}, {}^0T_{p,22}, {}^0T_{p,32}]^T = \frac{[{}^0T_{p,12}, {}^0T_{p,22}, {}^0T_{p,32}]^T}{\| [{}^0T_{p,12}, {}^0T_{p,22}, {}^0T_{p,32}] \|} \quad (4.6)$$

3. Evaluate the first column of the rotation matrix as the perpendicular to both second and third columns:

$$[{}^0T_{p,11}, {}^0T_{p,21}, {}^0T_{p,31}]^T = [{}^0T_{p,12}, {}^0T_{p,22}, {}^0T_{p,32}]^T \times [{}^0T_{p,13}, {}^0T_{p,23}, {}^0T_{p,33}]^T \quad (4.7)$$

4. Normalise the first column of the rotation matrix:

$$[{}^0T_{p,11}, {}^0T_{p,21}, {}^0T_{p,31}]^T = \frac{[{}^0T_{p,11}, {}^0T_{p,21}, {}^0T_{p,31}]^T}{\| [{}^0T_{p,11}, {}^0T_{p,21}, {}^0T_{p,31}] \|} \quad (4.8)$$

5. Evaluate the second column of the rotation matrix as the perpendicular to both third and first columns:

$$[{}^0T_{p,12}, {}^0T_{p,22}, {}^0T_{p,32}]^T = [{}^0T_{p,13}, {}^0T_{p,23}, {}^0T_{p,33}]^T \times [{}^0T_{p,11}, {}^0T_{p,21}, {}^0T_{p,31}]^T \quad (4.9)$$

6. Normalise the second column as in (4.6).

The Matlab non-linear system solver `fsove()` can be used. In order to increase the accuracy, the pseudo-code 4.1 has been implemented, so that the maximum number of acquired data is used still having a converging solution.

Results of the proposed calibration method are shown in Fig. 4.2 and Fig. 4.3.

4. DYNAMIC ACTIVE CONSTRAINTS

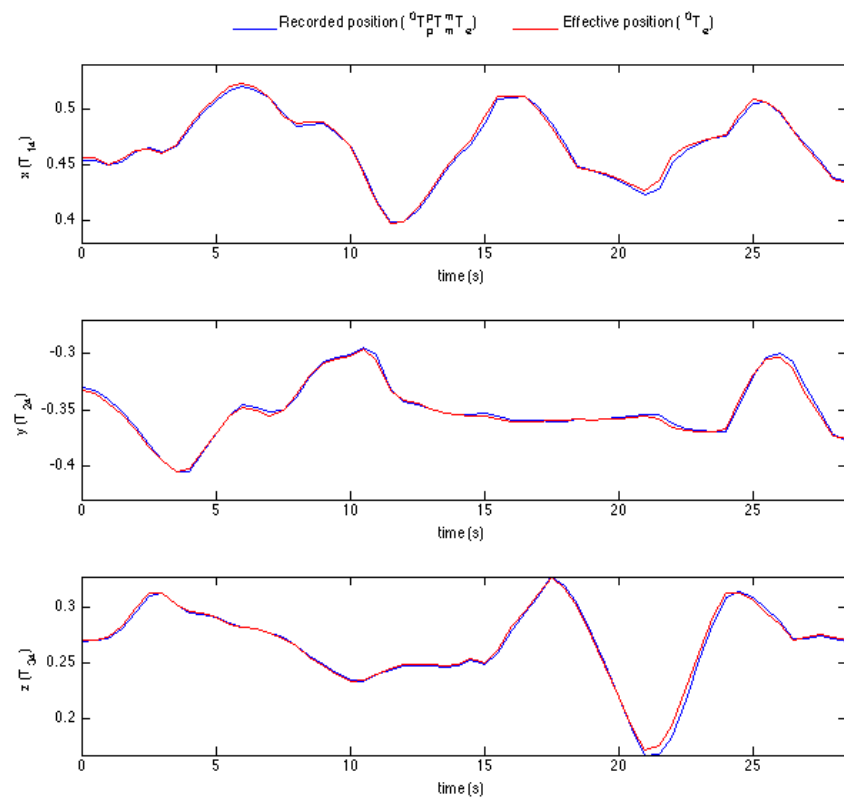


Figure 4.2: Validation of the proposed calibration procedure - position - The esteemed position (${}^0T_p{}^pT_m(t){}^mT_b$, blue) is compared to the position recorded by the robot (${}^0T_b(t)$, red).

4. DYNAMIC ACTIVE CONSTRAINTS

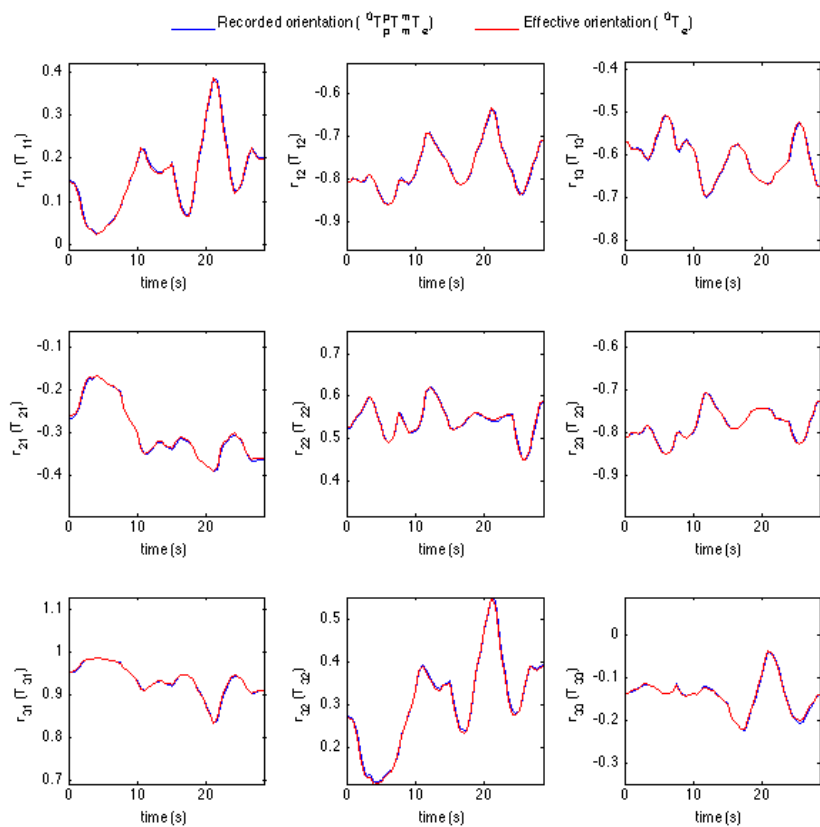


Figure 4.3: Validation of the proposed calibration procedure - orientation -
The esteemed rotation matrix (${}^0R_p {}^pR_m(t) {}^mR_b$, blue) is compared to the rotation matrix recorded by the robot (${}^0R_b(t)$, red).

4. DYNAMIC ACTIVE CONSTRAINTS

Algorithm 4.1 Calibration of the transformation matrices between the *Polaris VICRA* and the LWR.

- 1: Define a set of non-linear equations F considering the 12 constraints (4.4)
 - 2: Choose a random $k \in [1, w]$, being w the number of samples, and add k to the pool K
 - 3: Add the linear equations (4.2) for the sample k to the set F
 - 4: Evaluate 0T_p and bT_m through the Matlab solver `fsove()`
 - 5: **while** Solution is converging **do**
 - 6: Choose a random $k \in [1, w], k \notin K$, being w the number of samples, and add k to the pool K
 - 7: Add the linear equations (4.2) for the sample k to the set F
 - 8: Evaluate 0T_p and bT_m through the Matlab solver `fsove()`
 - 9: **end while**
 - 10: Orthogonalise 0T_p and bT_m
 - 11: Evaluate ${}^mT_b = ({}^bT_m)^{-1}$
-

4.2.2 Trocar position during repositioning

Once the homogenous transformation matrix 0T_p has been calibrated, a marker can be applied on the knee bone (as shown in Fig. 4.1). Thus, the pose of the marker 0T_m in the robot base frame can be tracked for each sample k as:

$${}^0T_{m,k} = {}^0T_p {}^pT_{m,k} \quad (4.10)$$

being pT_m the homogenous transformation matrix provided by the Polaris. Contemporarily, the pose of the reference frame (x_b, y_b, z_b) is defined (in the robot base frame) by the matrix 0T_b (provided by the FRI) for each sample k . Thus, the pose of the instrument is defined in the marker reference frame (supposed rigidly connected to the trocar) by the homogenous transformation matrix ${}^mT_{b,k}$:

$${}^mT_{b,k} = {}^mT_{0,k} {}^0T_{b,k} = ({}^pT_{m,k})^{-1} ({}^0T_p)^{-1} ({}^0T_{b,k}) \quad (4.11)$$

Thus, having the instrument tip in the incision point, the trocar position in the marker base frame is defined by:

$${}^mT_T = ({}^pT_m)^{-1} ({}^0T_p)^{-1} ({}^0T_T) \quad (4.12)$$

4. DYNAMIC ACTIVE CONSTRAINTS

being 0T_T the matrix provided by the FRI when the instrument tip is on the incision point.

Once the trocar point is evaluated in the marker reference frame, the robot has to be constrained to pass through the point 0p_T (defined in the robot base frame):

$${}^0p_T = E_1 {}^0T_p {}^pT_m {}^mT_T E_2 \quad (4.13)$$

being 0T_p the calibration matrix between the robot base frame and the *Polaris VICRA* reference frame, pT_m the homogenous transformation matrix provided by the *Polaris VICRA*, E_1 and E_2 the matrices:

$$E_1 = \begin{bmatrix} 1 & 0 & 0 & 0 \\ 0 & 1 & 0 & 0 \\ 0 & 0 & 1 & 0 \end{bmatrix} \quad E_2 = \begin{bmatrix} 0 \\ 0 \\ 0 \\ 1 \end{bmatrix} \quad (4.14)$$

and mT_T the previously defined homogeneous transformation matrix.

4.2.3 Instrument motion during repositioning

For safety reasons, some of the constraints will be released when re-positioning occurs:

- If the instrument is **inside** the patient ($\lambda \leq L$, being λ the distance between the proximal end of the instrument and the trocar position (3.3), and L the length of the instrument), only the conical constraint centred in the trocar position will be applied, while releasing the additional constraint on the position of the tool tip;
- If the instrument is **outside** the patient ($\lambda > L$), the pose of the instrument is maintained constant with respect to the marker pose.

The pre-planned path can then be registered with the new position of the knee. However, in order to increase the safety of the operation, a manual registration (or a redefinition) of the path will be required; due to the expected low occurrence of re-positionings when a flexible instrument is introduced, this requirement should not represent a drawback of the proposed solution.

In conclusion, when limb-repositioning is recorded, *i.e.* when the displacement between the position of the marker between two following samples is above a predefined threshold ε , the pseudo-code 4.2 is applied.

4. DYNAMIC ACTIVE CONSTRAINTS

Algorithm 4.2 Constraining the motion of the instrument during limb repositioning

```

1: repeat
2:   Read the marker pose at the instant  $k \ ^pT_{m,k}$ 
3:   if displacement  $< \varepsilon$  then
4:     Read the instrument pose at the instant  $k \ ^0T_{B,k}$ 
5:     Evaluate the matrix:


$${}^mT_B^* = ({}^pT_{m,k})^{-1}({}^0T_p)^{-1}({}^0T_{B,k}) \quad (4.15)$$


6:   else
7:     if  $\lambda \leq L$  then
8:       Set the stiffness for the position equal to 0
9:     else
10:      Set the stiffness for the position equal to HF, as in Section 3.2.4
11:      Set the reference pose for the instrument as (see equation (4.15)):


$${}^0T_{b,\text{ref}} = ({}^0T_p)({}^pT_{m,k})({}^mT_B^*) \quad (4.16)$$


12:    end if
13:    Define the trocar position as:


$${}^0p_T = E_1 {}^0T_p {}^pT_{m,k} {}^mT_T E_2 \quad (4.17)$$


14:  end if
15: until Stop is required

```

4. DYNAMIC ACTIVE CONSTRAINTS

4.3 Flexible instrument for knee arthroscopy

In order to increase the ablation rate when performing a laser chondroplasty, an optimal approach angle should be achieved, *i.e.* the instrument should be as perpendicular as possible to the articular cartilage. However, in a minimally invasive procedure, the instrument has always to pass through the incision point; thus, the actual orientation of the instrument is defined by the position of the trocar.

A flexible instrument can be introduced for overcoming this limitation, so that the approach angle is not determined anymore by the incision point. A 2 DoFs flexible instrument was developed within the Hamlyn Centre (Fig. 4.4). This instrument is able of rotation around its axis and of bending. The outer diameter of the shaft is equal to 5 mm, while the inner diameter is equal to 2.8 mm. An optical fibre and/or an endoscopic flexible camera can be passed through the instrument. Two direct current (DC) motors (Faulhaber Group, <http://www.faulhaber.com>) with integrated incremental encoders are used for driving the rotation of the instrument and the bending of the rigid shaft. The reference frame (x_b, y_b, z_b) is centred in the proximal end of the rigid shaft of the flexible instrument, as in Fig. 3.3, while the reference frame (x_d, y_d, z_d) is centred in the instrument tip, having the z_d axis pointing as the instrument tip and the x_d axis in the bending plane. The rotation angle γ is defined as the rotation around the z_b axis in the $x_b y_b$ plane identified by the reference frame (x_b, y_b, z_b) , while the bending angle β is defined as the angle between the z_b axis of the reference frame (x_b, y_b, z_b) and the z_d axis of the rigid frame (x_d, y_d, z_d) , as shown in Fig. 4.5.



Figure 4.4: Flexible instrument for knee chondroplasty - The instrument can be connected on a positioner (such as the LWR) or used standalone.

4. DYNAMIC ACTIVE CONSTRAINTS



Figure 4.5: Definition of the reference frames for the flexible instrument - The bending angle β is shown in the figure.

The instrument is not provided of any sensor (apart from the incremental encoders embedded within the motors). Thus, the bending has to be esteemed according to the angular position of the motor. A kinematic analysis is performed in the next Section, and an experimental calibration of the instrument will be provided in Section 4.3.3.

4.3.1 Kinematic analysis

The 2 DoFs of the flexible instrument are the rotation around the z_b axis and the bending in the $x_d z_d$ plane. It is easier to describe the transformation performed by these 2 DoFs introducing a third reference frame (x_c, y_c, z_c) , centred in the origin of the (x_b, y_b, z_b) frame and rotated around the z_b axis of γ , being γ the rotation angle. Thus, the transformation between the (x_b, y_b, z_b) frame and the (x_c, y_c, z_c) frame is defined by the homogenous transformation matrix (4.18), *i.e.* a rotation around the z axis in the local reference frame:

$${}^b T_c(\gamma) = \begin{bmatrix} c_\gamma & -s_\gamma & 0 & 0 \\ s_\gamma & c_\gamma & 0 & 0 \\ 0 & 0 & 1 & 0 \\ 0 & 0 & 0 & 1 \end{bmatrix} \quad (4.18)$$

The rotation angle γ is related to the encoder position M_R by the following equation, since a couple of gears are used for increasing the motor torque:

$$\gamma = \frac{r_1}{r_2} \frac{1}{S} M_R \quad (4.19)$$

being r_1 the radius of the gear connected to the motor, r_2 the radius of the gear connected to the rotation axis and S the encoder sensibility (in pos/rad , being pos the position provided by the encoder).

4. DYNAMIC ACTIVE CONSTRAINTS

When considering the bending in the x_dz_d plane, a rotation of a β angle around the y_d axis is performed. However, the rotation of a β angle is also influencing the tip position in the x_cz_c plane. Thus, indicating with $f_x = f_x(\beta)$ the displacement along the x_c axis of the (x_c, y_c, z_c) reference frame consequent to a bending angle equal to β and with $f_z = f_z(\beta)$ the displacement along the z_c axis, the following homogenous transformation matrix between the (x_c, y_c, z_c) and the (x_d, y_d, z_d) reference frames can be evaluated:

$${}^cT_d(\beta) = \begin{bmatrix} c_\beta & 0 & s_\beta & f_x(\beta) \\ 0 & 1 & 0 & 0 \\ -s_\beta & 0 & c_\beta & f_z(\beta) \\ 0 & 0 & 0 & 1 \end{bmatrix} \quad (4.20)$$

The relationship $\beta = f_\beta(M_B)$ between the bending angle β and the encoder position M_B of the bending motor, and the functions $f_x = f_x(\beta)$ and $f_z = f_z(\beta)$ can be experimentally evaluated, as shown in Section 4.3.3.

By and large, the following homogeneous transformation matrix defines the transformation between the (x_b, y_b, z_b) frame (robot end-effector) and the (x_d, y_d, z_d) frame (tip position):

$${}^bT_d(\gamma, \beta) = \begin{bmatrix} c_\gamma c_\beta & -s_\gamma & c_\gamma s_\beta & c_\gamma f_x(\beta) \\ s_\gamma c_\beta & c_\gamma & s_\gamma s_\beta & s_\gamma f_x(\beta) \\ -s_\beta & 0 & c_\beta & f_z(\beta) \\ 0 & 0 & 0 & 1 \end{bmatrix} \quad (4.21)$$

4.3.2 Dynamic adaptation of the Active Constraints law

The bending angle β and the rotation angle γ , as well as the homogeneous transformation matrix ${}^0T_{b,\text{ref}}$ defining the reference pose for the LWR, as introduced in (3.70), have to be defined while the operator is performing the operation. The 6 DoFs Active Constraint technique introduced in Chapter 3 has to be slightly modified for dynamically adapting to the varying configuration of the flexible instrument. It will be assumed that the surface, where the position has to be constrained on, is known, and characterised by a set of points ${}^0C = \{{}^0c\}$ and the respective normal directions ${}^0N = \{{}^0N\}$ (0 denotes that both set of points and set of normals are defined in the robot base frame).

All the parameters can be defined following this procedure:

1. **Acquisition of information**

4. DYNAMIC ACTIVE CONSTRAINTS

- (a) Read the homogeneous transformation matrix ${}^0T_{b,k}$ of the actual pose of the (x_b, y_b, z_b) frame from the LWR controller and the homogeneous transformation matrix ${}^bT_{d,k}$ between the (x_b, y_b, z_b) and the (x_d, y_d, z_d) frame from the instrument at the time instant k .
- (b) Evaluate the homogeneous transformation matrix ${}^0T_{d,k}$ of the tip of the flexible instrument:

$${}^0T_{d,k} = {}^0T_{b,k} {}^bT_{d,k} = \begin{bmatrix} {}^0x_{d,k} & {}^0y_{d,k} & {}^0z_{d,k} & {}^0p_{d,k} \\ 0 & 0 & 0 & 1 \end{bmatrix} \quad (4.22)$$

- (c) Find the closest point ${}^0c^*$ to the instrument tip within the pre-defined region and the normal direction ${}^0n^*$ to the surface in ${}^0c^*$.

2. Definition of the rotation angle γ

- (a) Evaluate the desired orientation ${}^0y_{d,k+1}^d$ for the y_d axis at the time instant $k + 1$ as:

$${}^0y_{d,k+1}^d = \frac{{}^0n^* \times \overline{{}^0p_T} {}^0c^*}{\| {}^0n^* \times \overline{{}^0p_T} {}^0c^* \|} \quad (4.23)$$

y_d has to be perpendicular to the bending plane, that has to contain the trocar point 0p_T , the closest point to the tip position ${}^0c^*$, and the normal direction to the surface ${}^0n^*$.

- (b) The instrument has to rotate of an angle $\Delta\gamma_{k+1}$ around its axis (*i.e.* the z_b axis of Fig. 4.5), being $\Delta\gamma_{k+1}$ the angle between the actual orientation of the y_d axis ${}^0y_{d,k}$ and the desired orientation for the time instant $k + 1$ ${}^0y_{d,k+1}^d$:

$$\Delta\gamma_{k+1} = \arcsin \left(\frac{{}^0y_{d,k} \times {}^0y_{d,k+1}^d}{\| {}^0y_{d,k} \times {}^0y_{d,k+1}^d \|} \right) \quad (4.24)$$

- (c) The motor position M_R for the rotation motor can be defined accordingly to (4.19) as:

$$M_R = S_{r_1}^{r_2}(\gamma_{k+1}) \quad \gamma_{k+1} = \gamma_k + \Delta\gamma_{k+1} \quad (4.25)$$

being γ_k the rotation angle for the time instant k .

3. Definition of the bending angle β

4. DYNAMIC ACTIVE CONSTRAINTS

- (a) The normal direction ${}^0n^*$ can be represented in the (x_d, y_d, z_d) reference frame (evaluated at the time instant k) as:

$${}^d n^* = [{}^0 x_{d,k} \quad {}^0 y_{d,k} \quad {}^0 z_{d,k}]^T {}^0 n^* \quad (4.26)$$

- (b) The bending angle should be increased (or decreased) of the quantity $\Delta\beta_{k+1}$ between the time instants k and $k+1$:

$$\Delta\beta_{k+1} = \text{atan} \left(\frac{{}^d n_x^*}{{}^d n_z^*} \right) \quad (4.27)$$

being ${}^d n_x^*$ and ${}^d n_z^*$ the x and z components, respectively, of the normal direction ${}^d n^*$ in the (x_d, y_d, z_d) reference frame.

- (c) The motor position M_B for the bending angle can be defined as:

$$M_B = f_\beta^{-1}(\beta_{k+1}) \quad \beta_{k+1} = \beta_k + \Delta\beta_{k+1} \quad (4.28)$$

being β_k the bending angle for the time instant k , and $f_\beta(M_B)$ the empirical relationship between the bending angle β and the motor position M_B , as introduced in Section 4.3.3.

4. Definition of the reference pose ${}^0T_{b,\text{ref}}$ for the LWR

- (a) The configuration for the flexible instrument for the time instant $k+1$ can be evaluated as ${}^b T_{d,k+1} = {}^b T_d$ and, supposing not big changes in the LWR configuration between the time instants k and $k+1$, an approximation of the homogeneous transformation matrix ${}^0 \tilde{T}_{d,k+1}$ between the (x_d, y_d, z_d) frame and the robot base frame for the time instant $k+1$ can be evaluated as:

$${}^0 \tilde{T}_{d,k+1} = {}^0 T_{b,k} {}^b T_{d,k+1} = \begin{bmatrix} {}^0 \tilde{x}_{d,k+1} & {}^0 \tilde{y}_{d,k+1} & {}^0 \tilde{z}_{d,k+1} & {}^0 \tilde{p}_{d,k+1} \\ 0 & 0 & 0 & 1 \end{bmatrix} \quad (4.29)$$

- (b) The point ${}^0 B^*$ in Fig. 4.5 can be evaluated as:

$${}^0 B^* = {}^0 c^* - \frac{f_x(\beta_{k+1})}{\sin(\beta_{k+1})} {}^0 \tilde{z}_{d,k+1} \quad (4.30)$$

- (c) The distance L^* between the (x_b, y_b, z_b) frame and the B^* point along the z_b axis is equal to:

$$L^* = f_z(\beta_{k+1}) - \frac{f_x(\beta_{k+1})}{\tan(\beta_{k+1})} \quad (4.31)$$

4. DYNAMIC ACTIVE CONSTRAINTS

- (d) The rotation matrix ${}^0R_{k+1}$ for the time instant $k + 1$ can be defined accordingly to (3.29).
- (e) The reference position for the LWR for the time instant $k + 1$ is eventually evaluated as:

$${}^0T_{b,\text{ref}} = \begin{bmatrix} {}^0R_{k+1} & B^* - L^* {}^0z_{b,k} \\ 0 & 0 & 1 \end{bmatrix} \quad (4.32)$$

For guaranteeing the fastest possible update rate, a multithread control program was implemented, as shown in Fig. 4.6, having five different threads: the main thread handles the Active Constraints technique; the thread “*FRI*” controls the LWR in the operational space, while the control in the joint space is provided by the KRC; the thread “*Faulhaber Controller*” sets the bending angle β and the rotation angle γ for the flexible instrument, while the motor position is defined by a PID controller (“*Motor controller*”); the thread “*UDP*” handles the communication with the Polaris VICRA; the thread “*Event handling*” deals with the communication with other input devices, such as the keyboard.

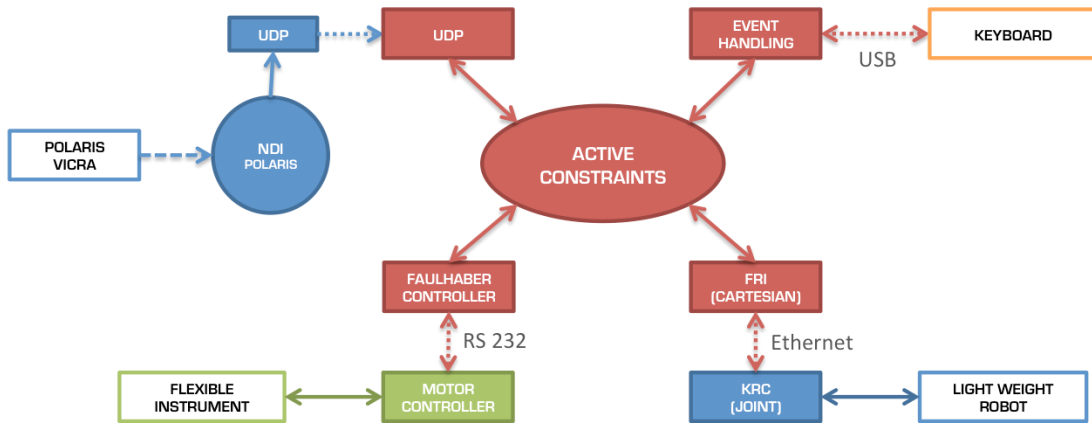


Figure 4.6: Multithread architecture of the control program - The GLFW (<http://www.glfw.org/>) framework was used.

4.3.3 Calibration of the flexible instrument

For defining the relationship $\beta = f_\beta(M_B)$ between the bending angle β and the motor position M_B , and for defining the functions f_x and f_z defined in (4.20), the Aurora Electromagnetic Tracking System (Northern Digital Inc.¹) was used for tracking the

¹<http://www.ndigital.com/medical/aurora.php>

4. DYNAMIC ACTIVE CONSTRAINTS

pose of the tip of the flexible instrument, while varying the motor position. A 6 DoFs electromagnetic sensor was used (Aurora Mini 6DOF Sensor - 610029) and inserted in the flexible instrument. It is worth noticing that the calibration will not provide an accurate measurement of the tip position, as discussed in Section 4.3.5.

The “0 position” of the incremental encoder was set having a null bending angle (*straight configuration*), in order to have $\beta = 0$ for $M_B = 0$. The pose of the tip is defined with respect to the tracking system base frame (x_t, y_t, z_t). The *straight configuration* is considered as the reference configuration R . Thus, the reference pose is defined in the tracking system base frame by the homogeneous transformation matrix tT_R :

$${}^tT_R = {}^tT_d(M_B = 0) \quad (4.33)$$

being tT_d the matrix provided by the Aurora system. The motor was moved several time in both positive and negative directions, acquiring a set of homogeneous transformation matrices ${}^tT_{d,k}$ ($k = 1, \dots, w$, being w the number of samples). For each sample, the pose relative to the reference pose (*straight configuration*) was evaluated as:

$${}^R T_{d,k} = ({}^tT_R)^{-1} {}^tT_{d,k}(M_{B,k}) \quad \forall k \in [1; w] \quad (4.34)$$

For all the sampled homogeneous transformation matrices ${}^R T_{d,k}$, the following parameters were recorded:

$$M_{B,k}; \quad \beta_k = \text{atan2}(t_{13}, t_{33}); \quad f_{x,k} = t_{14}; \quad f_{z,k} = t_{34}$$

being t_{ij} the element i, j of the matrix ${}^R T_{d,k}$.

Polynomial interpolation is used for relating these values in the relationships $\beta = f_\beta(M_B)$, $f_x = f_x(\beta)$ and $f_z = f_z(\beta)$.

4.3.4 Experimental results

The functions $\beta = f_\beta(M_B)$, $f_x = f_x(\beta)$ and $f_z = f_z(\beta)$ are shown in Fig. 4.7 and 4.8.

As shown in Fig. 4.7, due to some backlash caused by the tendon-driven actuation, the function $\beta = f_\beta(M_B)$ is dependant on the motion direction (positive or negative). However, the relationship between the motor position and the bending angle is roughly linear for both positive and negative motion directions, and an empirical function f_β can be considered:

$$\beta = f_\beta(M_B) = b_1 M_B + b_2 \quad (4.35)$$

4. DYNAMIC ACTIVE CONSTRAINTS

being the coefficients b_1 and b_2 different for positive and negative motions.

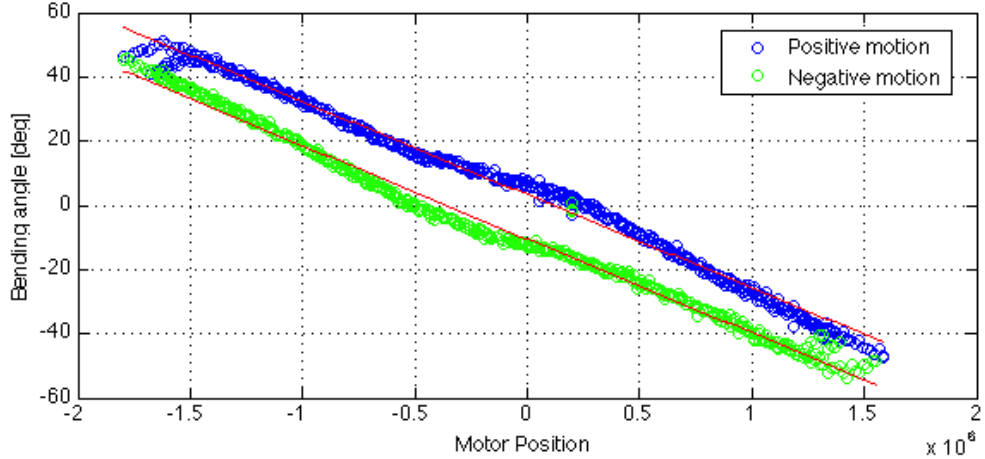


Figure 4.7: Calibration of the flexible instrument - bending angle - The relationship between the motor position M_B and the bending angle β is shown for both positive (blue) and negative (green) motion directions.

Due to the dependency of the empirical relationship (4.35) on the motion direction, also the function $f_x = f_x(\beta)$ and $f_z = f_z(\beta)$ are dependent on the motion direction. These functions are shown in Fig. 4.8 for both motion directions. While f_x has approximately a linear behaviour:

$$f_x = f_x(\beta) = x_1\beta + x_2 \quad (4.36)$$

the function f_z shows a parabolic behaviour.

Moreover, when considering the function f_z , the length of the instrument should also be considered, since the function f_z is representing the distance between the tip and the proximal end of the laparoscopic instrument; the length of the instrument L was measured using the LWR calibration tool. Thus, the function f_z is defined as:

$$f_z = f_z(\beta) = z_1\beta^2 + z_2\beta + z_3 + L \quad (4.37)$$

Numerical coefficients are quoted in Tab. 4.1.

4.3.5 Discussion

The designed flexible instrument is able to rotate around its axis and to bend; these additional DoFs enhance the intracorporeal dexterity of the instrument, increasing the

4. DYNAMIC ACTIVE CONSTRAINTS

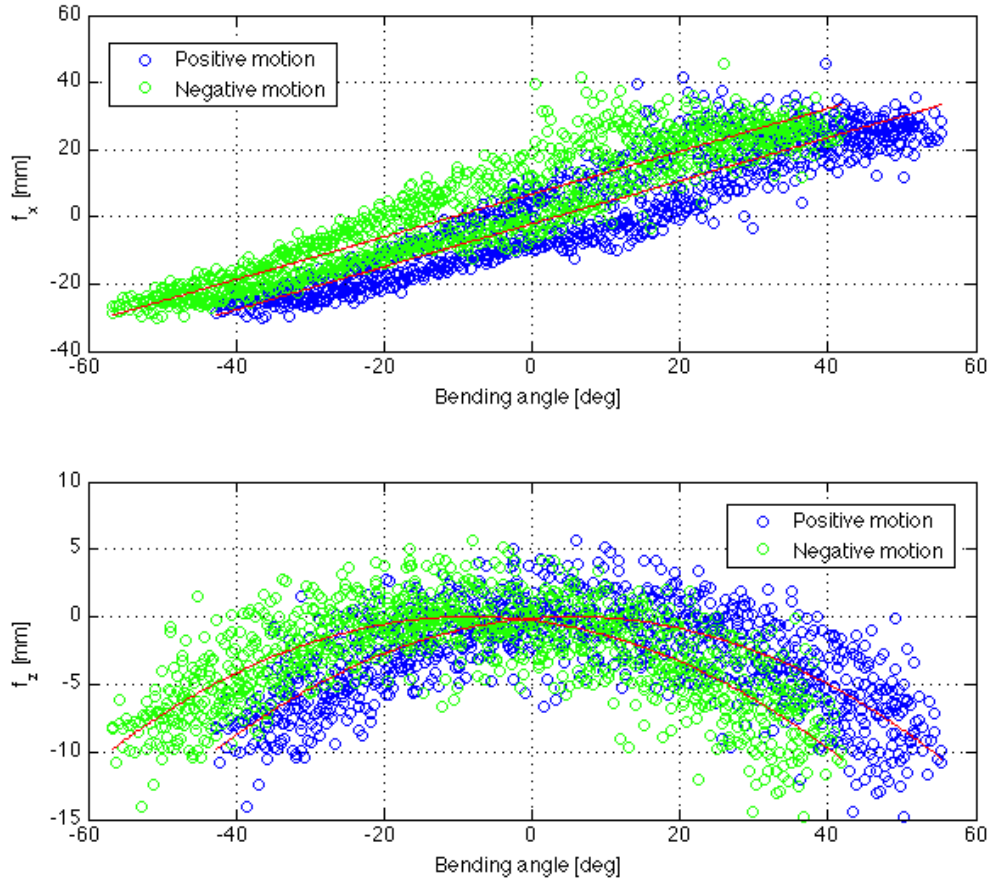


Figure 4.8: Calibration of the flexible instrument - f_x and f_z - The function f_x and f_z have been defined for both positive (blue) and negative (green) motion directions.

Table 4.1: Calibration of the flexible instrument - Numerical coefficients.

Coefficient	Unit	Positive	Negative
b_1	[deg/pos]	$-2.8989e - 5$	$-2.9146e - 5$
b_2	[deg]	3.2415	-10.6185
x_1	[mm/deg]	0.6402	0.6368
x_2	[mm]	-2.0752	6.7613
z_1	[mm/deg ²]	-0.0042	-0.0042
z_2	[mm/deg]	0.0469	-0.0695
z_3	[mm]	-0.1075	-0.2665
L	[mm]	264	264

4. DYNAMIC ACTIVE CONSTRAINTS

reachable and dexterous workspace. Moreover, an optimal approach direction can be achieved. While the rotation around the instrument axis can be related with the encoder measurement defining a proportional coefficient dependant only on the reduction ratio and the sensibility of the encoder according to (4.19), an empirical function has to be defined for relating the rotation of the bending motor and the bending of the instrument, due to the tendon-driven actuation.

Although the function $\beta = f_\beta(M_B)$ (4.35) is quite repeatable, backlash has to be considered when evaluating the bending angle. Moreover, due to the elasticity of the tendon, the calibration has to be repeated occasionally, for taking into account the tendons deformation.

In addition, when contacts between the flexible shaft and the human tissues happen, it is not possible to esteem the configuration of the flexible instrument, and the calibrated functions $\beta = f_\beta(M_B)$, $f_x = f_x(\beta)$ and $f_z = f_z(\beta)$ do not provide anymore accurate results; moreover, displacements in the y_d direction might happen.

The tendons tension might be measured for increasing the knowledge about the flexible instrument pose; however, shape and position sensing should be integrated for having an accurate information on the pose of the flexible instrument. As an example, the fibre optic shape sensing proposed by Luna Innovations¹ might be used.

4.4 Conclusions

In this Chapter, an extension to the 6 DoFs Active Constraints technique introduced in Chapter 3 was proposed, for dynamically adapting it under the varying environment and flexible instrument configuration.

For tracking changes in the environment, an optimal tracking system was introduced. A calibration algorithm was proposed for quickly defining the pose of the tracking system in the robot base frame. The tracking system is able to follow the trocar position, and a motion law for moving the instrument while re-positioning the limb was proposed in Section 4.2.3.

Moreover, for reducing the occurrences of re-positionings, a flexible instrument was introduced, which is able to increase the workspace and the ablation rate when performing a laser chondroplasty. The 6 DoFs Active Constraints technique introduced

¹<http://www.lunainnovations.com/technologies/shape-sensing.htm>

4. DYNAMIC ACTIVE CONSTRAINTS

in the previous Chapter was adapted for achieving an optimal approach direction, and for dealing with the additional DoFs of the flexible instrument. The kinematics of the flexible instrument was empirically defined. The behaviour of the instrument is quite repeatable in absence of contacts, although the effects of backlash in the tendon-driven actuation are not negligible.

However, when contacts happen, it is not possible to predict the configuration of the instrument, and sensing should be integrated.

In the next Chapter, two techniques for implicitly acquiring the trocar position and the pre-defined region where the instrument should be constrained on will be introduced, and a subject tests will be performed for analysing the enhancements in performances.

Chapter 5

Implicit Active Constraints

5.1 Introduction

The 6 DoFs Active Constraints technique introduced in Chapter 3 requires prior knowledge of the trocar position and the pre-defined path in order to provide guidance to the manipulation of the instrument. However, for improving the control ergonomics, the acquisition of the constraints should be natural, without increasing the setup time. Moreover, the 6 DoFs Active Constraints technique can be extended for accurate surgical exploration on a surface. Such an extension requires an effective method to interpolate a surface based on a set of non-ordered 3D control points, acquired by the surgeon at the beginning of the operation. This surface interpolation technique will be presented in Section 5.2, then, a method for deriving the trocar position considering only the first movements of the surgeon will be presented in Section 5.3. Generally, all the constraints can be defined *implicitly* by the surgeon, without having to acquire any programming skill or any prior knowledge regarding the patient's anatomy, thus avoiding the use of imaging techniques, such as CT or MRI, reducing setup times, costs and radiation dose to the patient.

To evaluate the practical value of the proposed control system in terms of surgical outcomes, detailed performances analysis on a group of subjects was carried on, as reported in Section 5.4. The subject tests were aimed to simulating a minimally invasive laser chondroplasty as realistically as possible. Some performance indices will be defined, and the control ergonomics will be qualitatively evaluated through a survey.

5. IMPLICIT ACTIVE CONSTRAINTS

5.2 Surface interpolation

In this section, an extension of the *Approximation Based On Smoothing* (ABOS) method introduced by Dressler will be proposed [21].

The original version of this method is used for defining a surface once few control points, represented in a canonical base in a 3D Cartesian space, have been assigned. An extension of the ABOS method will be proposed in Section 5.2, for deriving the surface. This extension will be able to use the method for surfaces not definable explicitly in a canonical base frame, adding the normal evaluation (this information will be used in Chapter 4) and introducing a *post-smoothing* interpolation for speeding up the process and assuring C^1 continuity. However, several interpolation techniques can be used for assuring higher degree continuity. The technique will be validated in detail in Section 5.2.7.

5.2.1 ABOS interpolation

The ABOS interpolation is mainly used for geology and geophysics applications, and can be used for fitting a set of points on a regular rectangular lattice (*base*), corresponding to the xy plane of the base frame. The interpolation is achieved in several steps:

1. Set the *altitude*, text it i.e. the z coordinate, of each node on the *base* to zero;
2. Project all the control points on the *base*;
3. Pair each point with the closest node on the *base*, and transfer the z coordinate of the point to the *altitude* of the node on the grid;
4. “Spread” The value of the node on its neighbourhood, until the *altitude* has been defined for each point within the grid (*Circulation*);
5. Apply the *Interpolating* operator (several interpolating operators have been proposed by Dressler, and the *Smoothing* interpolation was evaluated as suitable for the proposed application¹).

¹ The following text is quoted from Dressler Ph.D. thesis for the sake of clarity [21]:

“*Smoothing replaces elements of the [interpolated surface] by the value of weighted*

5. IMPLICIT ACTIVE CONSTRAINTS

When applying *Circulation*, the *Moore* neighbourhood is considered. However, if only the *von Neumann* neighbourhood is used (which can be seen as a subset of the *Moore* neighbourhood), smoothness might be increased.

The ABOS method does not ensure that the interpolated surface will pass through all the control points; however, the *smoothing* function (5.1) introduced by Dressler [21] can be modified in order not to smooth the surface when the closest points on the grid to the control points are considered:

$$P_{i,j} = \begin{cases} P_{i,j} & P_{i,j} \text{ is a control point} \\ \frac{\sum_{k=i-1}^{i+1} \sum_{l=j-1}^{j+1} P_{k,l} + P_{i,j} \cdot (q \cdot t_{i,j} - 1)}{q \cdot t_{i,j} + 8} & P_{i,j} \text{ is not a control point} \end{cases} \quad (5.3)$$

This consideration requires all the points have to be characterised also by a new property, so as to distinguish whether they are control points or not.

5.2.2 Extended ABOS method

The ABOS method requires a bijection between the points and the surface, since the fitting profile is described by an explicit surface, such as:

$$z = f(x, y) \quad \forall (x, y) \exists! z \quad (5.4)$$

where (x, y) are the coordinates of the point on the grid, and z its altitude.

This method can not be used when two points are projected on the same point of the *base*. However, provided that *the curvature of the under-investigation surface* on the condyles *is sufficiently small*, it is reasonable to assume that it always exists at least one plane that can be used as a *base* where the bijection is preserved.

average:

$$P_{i,j} = \frac{\sum_{k=i-1}^{i+1} \sum_{l=j-1}^{j+1} P_{k,l} + P_{i,j} \cdot (q \cdot t_{i,j} - 1)}{q \cdot t_{i,j} + 8} \quad (5.1)$$

where q us the parameter of the ABOS method controlling smoothness of the interpolation / approximation (its default value is 0.5) and $t_{i,j}$ are weights, which are zero before the first smoothing and afterward they are computed according the formula:

$$t_{i,j} = \left(\sum_{k=i-2}^{i+2} \sum_{l=j-2}^{j+2} (P_{i,j} - P_{k,l}) \right)^2 \quad (5.2)$$

and scaled into the interval $< 0, 100 >$.

This algorithm is repeated $K^2/16$ times, where K is the maximum distance (in number of cells) from the control point to the border of the regions obtained with *Circulation*.

5. IMPLICIT ACTIVE CONSTRAINTS

The plane where the *base* lies on can be defined using the *multiple regression* technique, *i.e.*, given a set of points $\{P_i = (x_i, y_i, z_i)\}, i = 1, \dots, m$, it is the plane $z = a \cdot x + b \cdot y + c$ that reduced the residual E_i [36]:

$$E_i = z_i - z = z_i - (a \cdot x + b \cdot y + c) \quad (5.5)$$

Parameters a , b and c can then be defined as [36]:

$$\begin{bmatrix} a \\ b \\ c \end{bmatrix} = \begin{bmatrix} \sum_{i=1}^m x_i^2 & \sum_{i=1}^m x_i y_i & \sum_{i=1}^m x_i \\ \sum_{i=1}^m x_i y_i & \sum_{i=1}^m y_i^2 & \sum_{i=1}^m y_i \\ \sum_{i=1}^m x_i & \sum_{i=1}^m y_i & m \end{bmatrix}^{-1} \begin{bmatrix} \sum_{i=1}^m x_i z_i \\ \sum_{i=1}^m y_i z_i \\ \sum_{i=1}^m z_i \end{bmatrix} \quad (5.6)$$

An orthogonal reference frame $(\hat{x}, \hat{y}, \hat{z})$ can be defined, having \hat{x} and \hat{y} lying on the plane, and \hat{z} perpendicular to the plane. Giving three arbitrary points Q_1 , Q_2 and Q_3 on the plane ¹:

$$Q_1 = \begin{bmatrix} 0 \\ 0 \\ c \end{bmatrix} \quad Q_2 = \begin{bmatrix} 1 \\ 0 \\ a+c \end{bmatrix} \quad Q_3 = \begin{bmatrix} 0 \\ 1 \\ b+c \end{bmatrix} \quad (5.7)$$

\hat{x} is the unitary vector point towards Q_2 from Q_1 , \hat{z} is perpendicular to both $\overrightarrow{Q_1 Q_2}$ and $\overrightarrow{Q_1 Q_3}$. The reference frame $(\hat{x}, \hat{y}, \hat{z})$ is formed as follows:

$$\hat{x} = \frac{\overrightarrow{Q_1 Q_2}}{\|\overrightarrow{Q_1 Q_2}\|} \quad \hat{z} = \frac{\overrightarrow{Q_1 Q_2} \times \overrightarrow{Q_1 Q_3}}{\|\overrightarrow{Q_1 Q_2} \times \overrightarrow{Q_1 Q_3}\|} \quad \hat{y} = \frac{\hat{z} \times \hat{x}}{\|\hat{z} \times \hat{x}\|} \quad (5.8)$$

Once the orthogonal base has been defined, all the points have to be transferred in the new reference frame [75]:

$$\hat{P}_i = {}^0 R_{\hat{0}}^T P_i \quad {}^0 R_{\hat{0}} = [\hat{x} \quad \hat{y} \quad \hat{z}] \quad (5.9)$$

Using this new representation, the coordinates $[\hat{x}_i, \hat{y}_i]$ represent the position of the considered control point on the *base*, while the coordinate \hat{z} is its *altitude*.

The *base* grid limit can be defined according to the following procedure:

1. Find out the convex hull of the projected points (the Andrew's Monotone Chain Algorithm was considered and implemented [5]);
2. Define the limits of the mesh based on the points with the lowest and highest \hat{x}_i and \hat{y}_i ;

¹This choose of points degenerates if the plane is orthogonal to the xy plane.

5. IMPLICIT ACTIVE CONSTRAINTS

3. Apply the ABOS interpolation;
4. Reject all the points outside from the convex hull.

Once the new plane has been defined, the surface can be created using the ABOS method as described at the beginning of this section. Result of the ABOS method will be a surface defined in the $(\hat{x}, \hat{y}, \hat{z})$ reference frame. In order to define the points in the operative theatre frame, the following transformation has to be applied for each point \hat{P}_i^* of the interpolated surface:

$$P_i^* = {}^0 R_{\hat{0}} \hat{P}_i^* \quad (5.10)$$

where ${}^0 R_{\hat{0}}$ is the rotation matrix defined in (5.9), and P_i^* is the representation of \hat{P}_i^* in the operative theatre frame.

In conclusion, the following steps have to be followed when implementing the proposed extended ABOS (eABOS) method:

1. Evaluate the *base* plane using the multiple regression technique (Fig. 5.1), according to (5.6);
2. Define a reference frame for the *base* plane, and evaluate the rotation matrix, according to (5.7), (5.8) and (5.9);
3. Transfer all the points to the new reference frame, with (5.9);
4. Find out a convex hull for the region of interest, and determine the lattice grid (for considerations about the dimension of the lattice grid, see Section 5.2.5);
5. Perform *circulation*, using the *von Neumann* neighbourhood with the aim to increase the surface smoothness (Fig. 5.2);
6. *Smooth* the surface in two steps (Fig. 5.3):
 - (a) Smooth the surface, according to (5.3);
 - (b) Update the weights $t_{i,j}$, according to (5.2).

In Section 5.2.4 the normal evaluation is introduced.

However, if the grid dimension is really small, the computational time for interpolating the surface might increase dramatically; thus, the method can be used for

5. IMPLICIT ACTIVE CONSTRAINTS

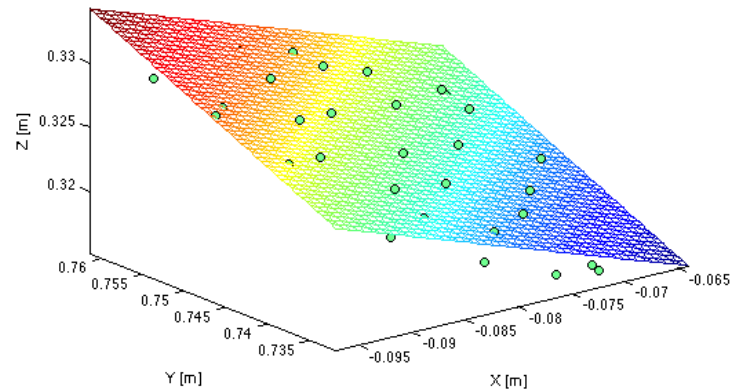


Figure 5.1: eABOS *base plane* - The *base plane* is evaluated using the multiple regression technique [36].

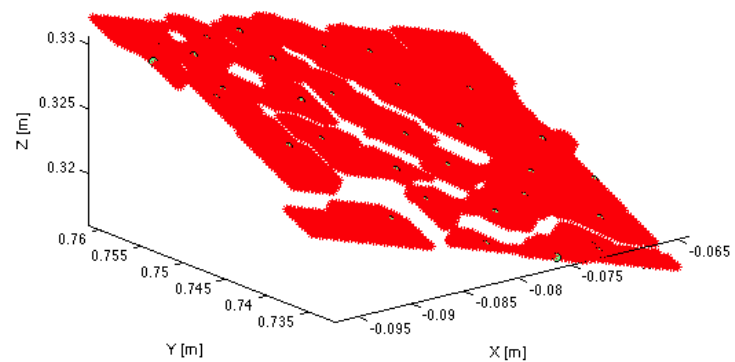


Figure 5.2: Results of the *Circulation* - The *Circulation* is performed using the *von Neumann* neighbourhood, in order to increase the smoothness.

5. IMPLICIT ACTIVE CONSTRAINTS

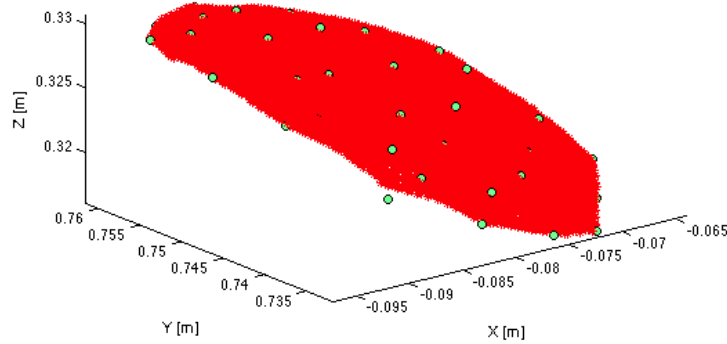


Figure 5.3: Results of the eABOS method - After the smoothing, only the points within the convex hull are considered, while the others are rejected.

interpolating a surface on a bigger lattice, and using other techniques for increasing the resolution of the lattice, still obtaining a smooth surface, as discussed in Section 5.2.6.

5.2.3 Advantages of the proposed method

Regarding the under-examination procedure, the proposed technique exhibits the following advantages over the original ABOS method:

1. This method can be used for interpolating a surface that is not excessively convex, without requiring bijection;
2. Diagonal borders between different *circulation* regions can be obtained due to the implementation of the *Von Neumann* neighbourhood instead of the *Moore* neighbourhood, thus increasing the smoothness of the interpolated surface;
3. Evaluation of surface normal can be introduced (Section 5.2.4);
4. The resolution of the interpolated surface can be improved using the techniques described in Section 5.2.6;
5. Continuity in C^1 can be obtained using Catmull spline patch, as shown in Fig. 5.7. Moreover, higher degree continuity can be assure using different techniques (for example, Bezier Curves can assure C^2 continuity);

5. IMPLICIT ACTIVE CONSTRAINTS

6. An exact fitting of the surface to the control points can be achieved, if necessary, by implementing (5.3);
7. This method can be used for the interpolation of a non-rectangular surface, since the border of the interpolated surface is obtained considering the *convex hull* of the control points projected on the *base* frame.

Moreover, with respect to other surface interpolation techniques, the following advantages are achieved in both original and extended ABOS methods:

1. The surface is determined once a set of point is given, and no information about how the points are connected to each others is required;
2. The surface is defined on a rectangular grid, thus allowing the implementation of the proposed 6 DoFs Active Constraints technique (see Section 3.2.4);
3. For each point, its neighbourhood is defined by the closest point on the *base* grid; thus, when looking for the closest point (see Section 3.2.4), the search can be limited to the neighbourhood of the previous closest point without considering the whole set of points describing the surface.

5.2.4 Evaluation of the surface normal

In order to evaluate the normal vector of each point within the reconstructed surface, the circles approximating the curvature of the surface in both xz and yz planes will be considered.

Three points in the 3D space define univocally a circle, that can be seen as a local approximation of the curvature of the surface. Referring to Fig. 5.4 and considering the xz plane, the blue circle approximates the curvature of the surface in the x direction nearby the point (x_2, z_2) ; thus, the vector representing the normal to the surface in the xz plane (blue vector), lies down the line connecting the centre of the blue circle with the (x_2, z_2) point.

Equivalently, the red vector represents the normal to the surface nearby the same point in the yz plane, evaluated considering the red circle.

Since the points lie onto a regular grid, the distance d^* between two points in both x and y directions is fixed.

5. IMPLICIT ACTIVE CONSTRAINTS

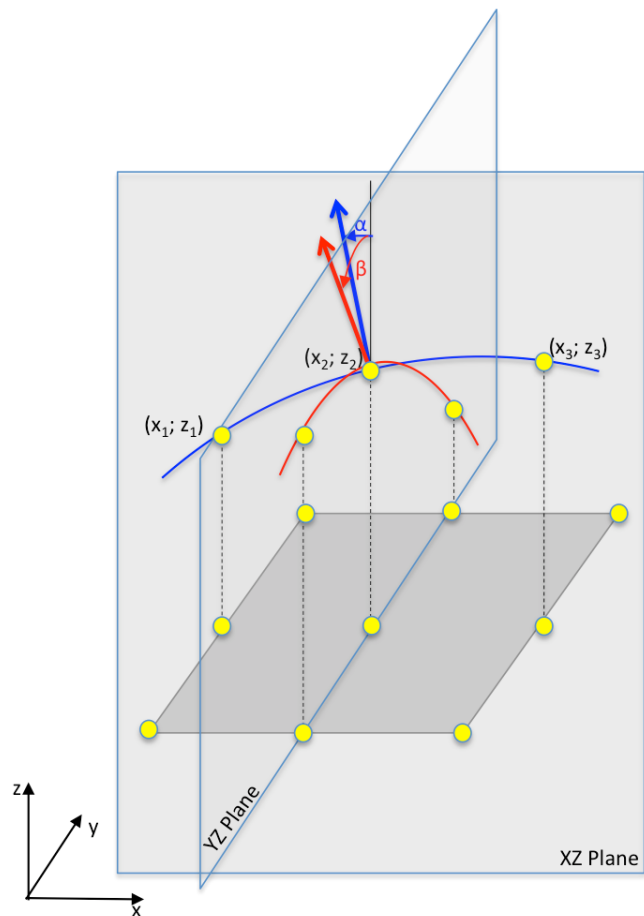


Figure 5.4: Theoretical explanation of how to evaluate the normal of the reconstructed surface - The points are aligned on a regular grid, and the normal can be evaluated considering separately the curvature in the xz plane and in the yz plane.

5. IMPLICIT ACTIVE CONSTRAINTS

Considering the xz plane, the centre of the blue circle in Fig. 5.4 is the intersection of the axes of the segments connecting the pairs of points $(x_1, z_1) - (x_2, z_2)$ and $(x_2, z_2) - (x_3, z_3)$. By trivial geometrical considerations, the slopes m_{12} and m_{23} of these two axes are, respectively:

$$m_{12} = \frac{d^*}{z_1 - z_2} \quad m_{23} = \frac{d^*}{z_2 - z_3} \quad (5.11)$$

Considering the axis of the segment connecting (x_1, z_1) and (x_2, z_2) , it has to pass through the point:

$$\left(\frac{x_1 + x_2}{2}, \frac{z_1 + z_2}{2} \right) = \left(x_2 - \frac{d^*}{2}, \frac{z_1 + z_2}{2} \right) \quad (5.12)$$

Thus, this axis is defined in the xz plane by the following equation:

$$z - \left(\frac{z_1 + z_2}{2} \right) = m_{12} \left[x - \left(x_2 - \frac{d^*}{2} \right) \right] \quad (5.13)$$

Equivalently, for the axis of the segment connecting (x_2, z_2) and (x_3, z_3) :

$$z - \left(\frac{z_2 + z_3}{2} \right) = m_{23} \left[x - \left(x_2 + \frac{d^*}{2} \right) \right] \quad (5.14)$$

Thus, the centre (x_c^{xz}, z_c^{xz}) of the circle approximating the surface nearby the point (x_2, z_2) in the xz plane can be evaluated as:

$$x_c^{xz} = x_2 + \frac{m_{12} + m_{23}}{m_{23} - m_{12}} \frac{d^*}{2} + \frac{1}{m_{12} - m_{23}} \frac{z_3 - z_1}{2} \quad (5.15)$$

$$z_c^{xz} = m_{12} \left(x_c^{xz} - x_2 + \frac{d^*}{2} \right) + \frac{z_1 + z_2}{2} \quad (5.16)$$

Equivalently, it is easy to define the centre (y_c^{yz}, z_c^{yz}) of the circle approximating the surface nearby the same point in the yz plane.

The tangents of the angles α and β (as shown in Fig. 5.4), which represent the angles between the vertical direction and the direction of the normal in the xz and yz planes, respectively, can be evaluated as:

$$\tan \alpha = \frac{x_c^{xz} - x_2}{z_c^{xz} - z_2} \quad \tan \beta = \frac{y_c^{yz} - y_2}{z_c^{yz} - z_2} \quad (5.17)$$

Considering an arbitrary value z^* for the z component of the normal to the surface, the vector n representing the normal itself can be evaluated as:

$$n = [z^* \cdot \tan \alpha \quad z^* \cdot \tan \beta \quad z^*]^T \quad (5.18)$$

5. IMPLICIT ACTIVE CONSTRAINTS

for $z^* = 1$, the unitary vector \hat{n} representing the normal is:

$$\hat{n} = \frac{[\tan \alpha \quad \tan \beta \quad 1]^T}{\sqrt{\tan^2 \alpha + \tan^2 \beta + 1}} \quad (5.19)$$

It is worth noticing that the normal is represented in the *base* plane evaluated with the multiple regression technique; thus, the normal can be represented in the operative theatre frame applying the transformation (5.10). Fig. 5.5 shows the results of the normal evaluation; the normal is continuous over the surface, as shown by the zooming represented in Fig. 5.6.

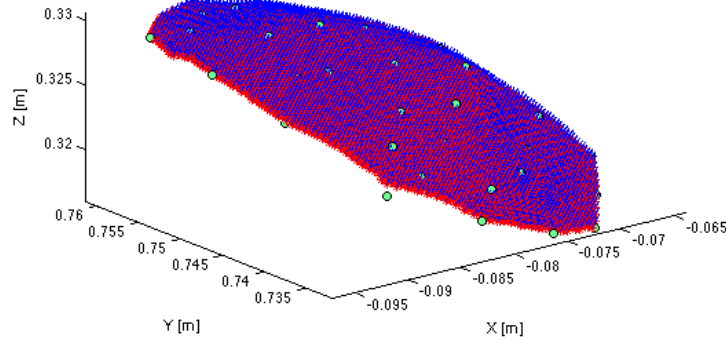


Figure 5.5: eABOS normal evaluation - The normal is evaluated considering the local curvature of the surface.

5.2.5 Lattice mesh and robot stiffness

The considerations introduced in Section 3.2.4 about the maximum distance ϵ between two points when considering a path following task, can be easily extended to define the lattice mesh dimension; when considering a surface where the points are aligned on a rectangular grid, the maximum distance between two points is on the diagonal of the grid; thus, the mesh dimension d^* should be equal to:

$$d^* = \frac{\epsilon}{\sqrt{2}} \leq \sqrt{2} \frac{LF}{k} \quad (5.20)$$

where the maximum distance ϵ is defined in (3.54), LF is the maximum force that the robot will exert due to the interpolation resolution when the surgeon is on the pre-planned surface and k is the desired stiffness.

5. IMPLICIT ACTIVE CONSTRAINTS

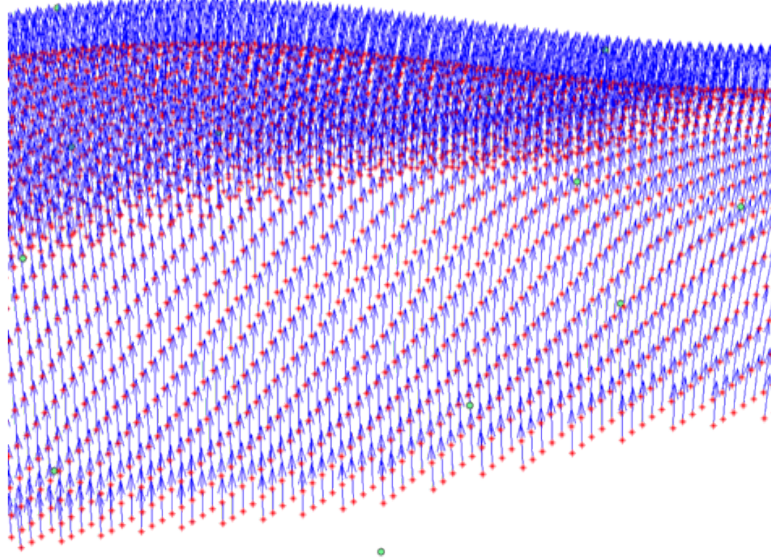


Figure 5.6: Results of the eABOS normal evaluation - The normal surface direction appears continuous along the surface.

Considering the same values previously quoted in Table 3.1, the lattice mesh dimension can be set as follows:

$$d^* = \begin{cases} 0.094 \text{ mm} & c^* < 100 \text{ } 1/m \\ \frac{0.0094}{c^*} & 100 \text{ } 1/m \leq c^* < 133.3 \text{ } 1/m \\ 0.071 \text{ mm} & c^* \geq 133.3 \text{ } 1/m \end{cases} \quad (5.21)$$

However, since evaluating the maximum curvature of a surface is a computational expensive process, the following conservative values can be considered for a surface scanning task:

$$k = 4000 \text{ N/m} \quad d^* = 0.07 \text{ mm} \quad (5.22)$$

5.2.6 Post-smoothing interpolation

The proposed extension to the ABOS algorithm was implemented in Matlab and tested on a *HP Z400 Workstation*, whose configuration is reported in Table 5.1, having terminated all the unnecessary processes. 22 control points were assigned, limited in a $14.6 \times 33.2 \times 16.5 \text{ mm}^3$ workspace. The computational time was evaluated repeating the algorithm 10 times. Results are quoted in Table 5.2.

5. IMPLICIT ACTIVE CONSTRAINTS

Computational time was distinguished in several tasks:

1. Evaluation of the *base* plane (*i.e.* evaluating the interpolating plane, defining a new reference frame, projecting all the points in the new reference frame);
2. Definition of the grid properties (*i.e.* evaluating the lattice dimension and the grid extension, analysing the convex hull, assigning the control points on the grid, checking whether the points on the grid are inside the convex hull or not);
3. *Circulation* (circulation was performed using the *Von Neumann* neighbourhood);
4. *Smoothing* (considering the equation (5.2)) and *Normal evaluation*.

Although the surface interpolation has not to be evaluated necessarily in real-time, modifications of operative conditions due to redefinition of the operative surface or reposition of the limb, require a new intra-operative surface re-evaluation. Thus, computational time should be reduced.

Table 5.1: HP Z400 Workstation properties

Parameter	Value
Processor	Intel Xeon CPU W3520 @ 2.67 GHz
Ram	4 GB
Operative system	Windows 7 Professional SP1
Matlab Version	R 2011 b

Table 5.2: Computational time of the extended ABOS method

Task	Mean [s]	St. Dev. [s]
Evaluation of the <i>base</i> plane	5e-4	< 2e-5
Definition of grid properties	22.8	0.036
<i>Circulation</i>	22.3	0.045
<i>Smoothing and Normal Eval.</i>	115.6	0.431
Total time	160.7	0.486

A *post-smoothing interpolation* is proposed for reducing the computational time. Instead of directly interpolating the surface on a grid with a lattice mesh dimension equal to d^* , a gross interpolation can be firstly performed on a lattice mesh equal to

5. IMPLICIT ACTIVE CONSTRAINTS

$d^* \cdot \lambda$, where $\lambda > 1$ is an integer scaling factor. Once the surface has been interpolated on the gross lattice using the above proposed eABOS method, a new fine interpolation is then performed, in order to improve the resolution of the lattice grid to the desired value. The fine interpolation is achieved using the *Catmull spline patch*, as shown in Fig. 5.7. The eABOS method produces a set of points perpendicular to the *base* plane (figure a). When performing the rows interpolation, the Catmull spline method described in (3.55) is applied row-by-row for all the points within the convex hull of the pre-planned surface (figure b), thus reducing the row dimension of λ . When all the rows have been interpolated, the same process is repeated for all the columns (figure c), thus reducing the mesh dimension to the desired value ($d^* \times d^*$) (figure d).

The Catmull spline technique is used for interpolating the three components of the coordinates of the points describing the surface, as well as the three components of the normal to the surface for each point. Results of the interpolation are shown in Fig. 5.8.

The pseudo-code for the proposed *eABOS method with post-smoothing interpolation* is reported in Algorithm 5.1.

It is worth noticing that the proposed method increases the error when the control points have to be assigned to the rectangular grid, since the bigger is the lattice mesh, the higher is the error. In fact, when the desired resolution is directly reached with the eABOS method without post-smoothing interpolation, the maximum error is achieved when the control point is exactly at the centre of the square mesh, thus a position error of $d^*/\sqrt{2}$ is reached, being d^* the dimension of the lattice mesh. However, if a scaling factor $\lambda > 1$ is considered, the maximum error linearly increases with the scaling factor coefficient, according to the relation:

$$\varepsilon \leq \frac{d^* \cdot \lambda}{\sqrt{2}} \quad (5.23)$$

where ε is the error.

The algorithm was tested in the same conditions described at the beginning of this Section, for $\lambda \in [2; 10]$. The proposed method reduced drastically the computational time; results are plotted in Fig. 5.9. It is worth noticing that the evaluation of the *base* plane is not affected by the scaling factor, being dependent only on the number of control points.

5. IMPLICIT ACTIVE CONSTRAINTS

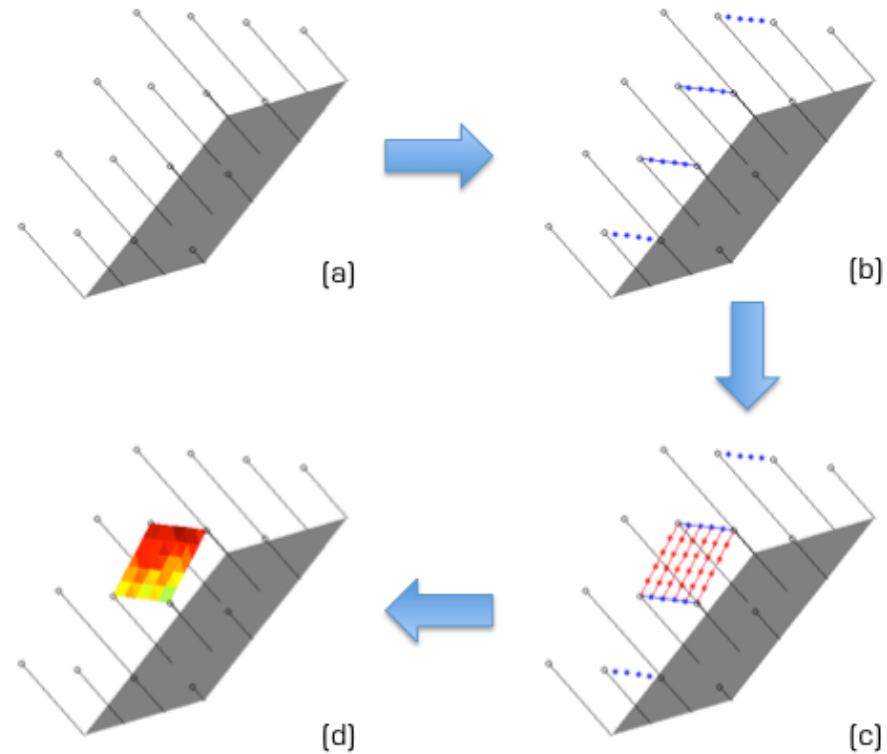


Figure 5.7: Representation of the *post-smoothing interpolation* method - The figures show the enhanced resolution for a scaling factor $\lambda = 5$, applying the Catmull spline patch.

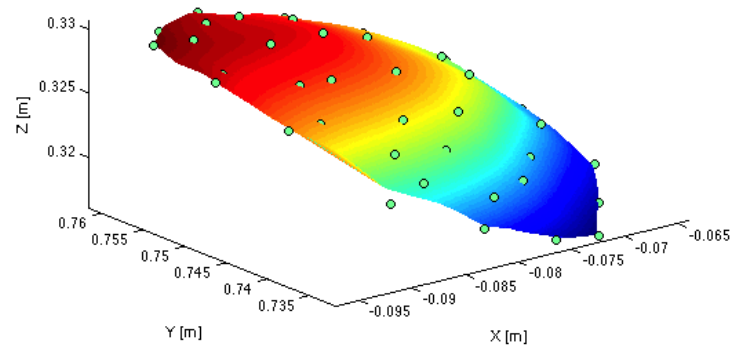


Figure 5.8: eABOS post-smoothing interpolation - Resolution is increased with the post-smoothing interpolation.

5. IMPLICIT ACTIVE CONSTRAINTS

Algorithm 5.1 eABOS method with post-smoothing interpolation

- 1: Read the control points P_i
- 2: Define the base plane according to (5.5) and (5.6)
- 3: Define a reference frame for the base plane according to (5.7) and (5.8)
- 4: **for all** P_i **do**
- 5: $\hat{P}_i = {}^0 R_{\hat{0}}^T P_i$
- 6: **end for**
- 7: Define the convex hull CH of the surface
- 8: Define the gross grid properties (row mesh dimension = $d^* \cdot \lambda$; column mesh dimension = $d^* \cdot \lambda$)
- 9: **for all** \hat{P}_i **do**
- 10: Assign \hat{P}_i to the closest point on the grid
- 11: **end for**
- 12: $K = 0$
- 13: **repeat**
- 14: *Circulate* the border of each region considering the *von Neumann* neighbourhood
- 15: $K = K + 1$
- 16: **until** All the points on the grid have been assigned
- 17: $n = \max(4, K^2/16)$
- 18: **while** $n > 1$ **do**
- 19: *Smooth* the surface according to (5.3)
- 20: Update the weights $t_{i,j}$ according to (5.2)
- 21: Scale the weight in $<0, 100>$
- 22: $n = n - 1$
- 23: **end while**
- 24: Evaluate the normal for each point within the convex hull CH
- 25: Define a new semi-fine grid (row mesh dimension = d^* ; column mesh dimension = $d^* \cdot \lambda$)
- 26: **for** $i = 1 \rightarrow$ (number of columns in the **gross** grid) **do**
- 27: **for** $j = 1 \rightarrow$ (number of rows in the **gross** grid) $- 1$ **do**
- 28: **if** $\text{gross grid}_{i,j}$ and $\text{gross grid}_{i,j+1} \in CH$ **then**
- 29: Interpolate $\lambda - 1$ points using C-Spline between $\text{gross grid}_{i,j}$ and $\text{gross grid}_{i,j+1}$
- 30: Interpolate $\lambda - 1$ normals using C-Spline between $\text{gross grid}_{i,j}$ and $\text{gross grid}_{i,j+1}$

5. IMPLICIT ACTIVE CONSTRAINTS

```

31:           Assign the interpolated points on the semi-fine grid
32:       end if
33:   end for
34: end for
35: Define a new fine grid (row mesh dimension =  $d^*$ ; column mesh dimension =  $d^*$ )
36: for  $j = 1 \rightarrow$  (number of rows in the semi-fine grid) do
37:     for  $i = 1 \rightarrow$  (number of columns in the semi-fine grid) - 1 do
38:         if semi-fine grid $_{i,j}$  and semi-fine grid $_{i+,j} \in CH$  then
39:             Interpolate  $\lambda - 1$  points using C-Spline between semi-fine grid $_{i,j}$  and semi-
40:             fine grid $_{i+1,j}$ 
41:             Interpolate  $\lambda - 1$  normals using C-Spline between semi-fine grid $_{i,j}$  and
42:             semi-fine grid $_{i+1,j}$ 
43:             Assign the interpolated points on the fine grid
44:         end if
45:     end for
46: end for
47: for all  $\hat{P}_i \in$  fine grid do
48:      $P_i = {}^0 R_{\hat{0}} \hat{P}_i$ 
49: end for

```

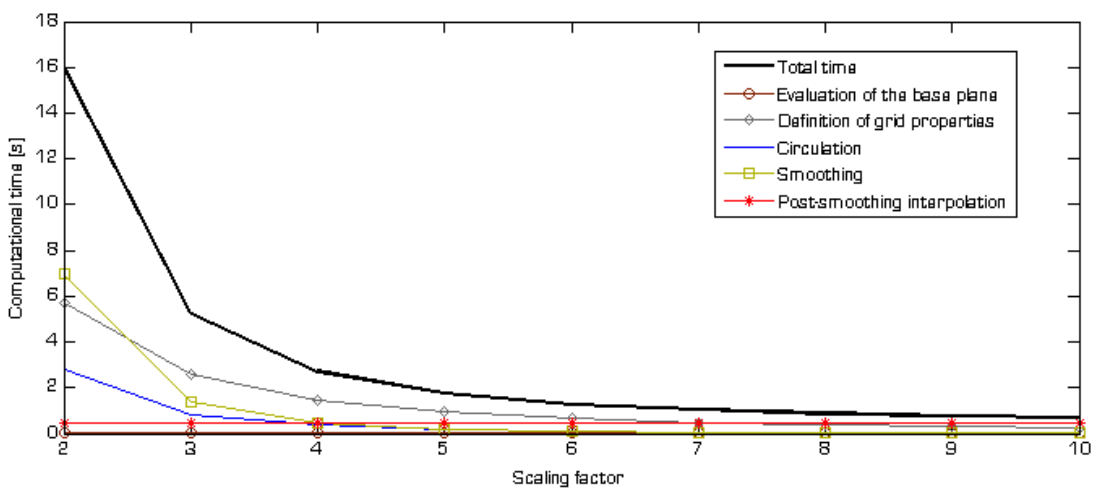


Figure 5.9: Reduction of computational time due to post-smoothing interpolation - The post-smoothing interpolation takes less than 0.5 s, independently of the scaling factor.

5. IMPLICIT ACTIVE CONSTRAINTS

If a maximum error equal to 0.25 mm can be considered as acceptable when assigning the control points, a scaling factor $\lambda = 5$ might be used (if $d^* = 0.07 \text{ mm}$, the maximum error is lower than 0.248 mm), for which the total computational time was measured equal to 1.74 s.

5.2.7 Validation of surface reconstruction

For validating the proposed surface reconstruction algorithm, a CT image of the knee phantom shown in Fig. 1.5 has been acquired¹. The surface is represented by a high-resolution mesh (41,987 Vertices; 84,092 Faces), and it represents the distal extremity of the femur and the proximal extremity of the tibia (Fig. 5.10).

Aim of this validation experiment is to reconstruct the highlighted area in Fig. 5.10, corresponding approximately to the condyles area, analysing the accuracy of the proposed surface reconstruction algorithm while varying the number of control points. The CT image is considered as the ground truth for validating the *eABOS* method.

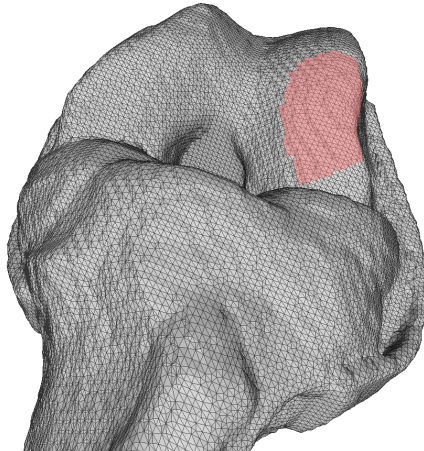


Figure 5.10: eABOS validation: Ground truth - The red area on the CT scan of the knee phantom, approximately corresponding to the condyles area, is considered as the ground truth.

The highlighted area in Fig. 5.10 comprises 374 vertices (automatically extracted from the CT image). Considering all the vertices within the area as control points, the *eABOS* technique was used for reconstructing the surface. An average distance

¹The author would like to acknowledge Julia Greenwood and Su-Lin Lee for having acquired and segmented the CT image of the knee phantom.

5. IMPLICIT ACTIVE CONSTRAINTS

of 0.189 mm was evaluated between the vertices of the ground truth and the closest point within the reconstructed surface (standard deviation: 0.143 mm). However, this results is not representative of a real error in the surface reconstruction algorithm, since the displacement is behind the resolution of a medical CT scanner ($1 - 2\text{ mm}$).

The surface reconstruction algorithm was repeated several time, each time reducing the number of control points (thus increasing the average distance between the points themselves). Results are shown in Fig. 5.11.

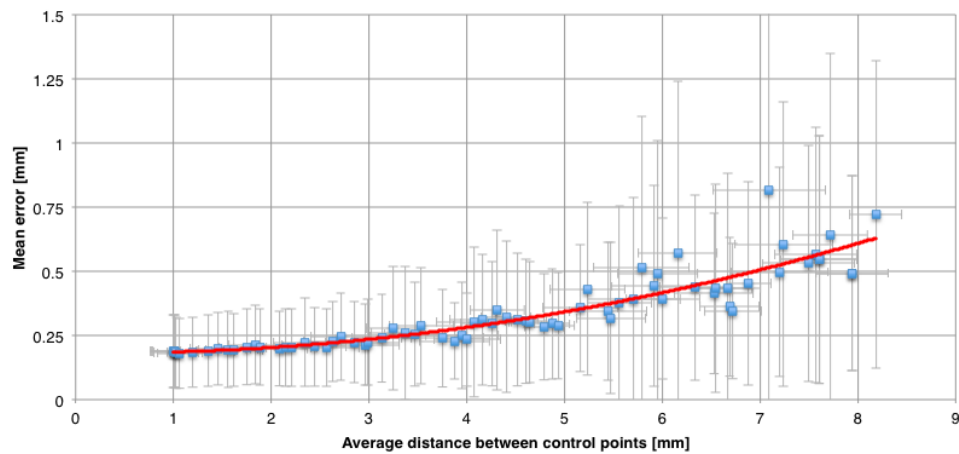


Figure 5.11: Results of the eABOS interpolation: mean error - The mean error is evaluated vs the average minimum value of the distance between the control points.

As expected, both average error and standard deviation increase when reducing the number of control points; the average error increases since fewer information are available for the surface reconstruction, while the standard deviation increases because the accuracy of the surface reconstruction algorithm is depending on the closeness to the nearest control point. However, it should be taken into account that a CT image was used for validating the results (accordingly to the clinical practice, where a CT scan is generally used for analysing the state of the decease). Thus, since the spatial resolution of a CT image is worse than 1 mm , if the mean error plus two times the standard deviation is lower than 1 mm , (supposing a normal distribution, this is the maximum value of the error for more than 95.44% of the samples), the error value should not be considered as significant. In conclusion, for an average distance between the control points lower than 5.16 mm , the maximum error value for 95.44% of the

5. IMPLICIT ACTIVE CONSTRAINTS

samples is not significant (maximum value of 0.97 mm recorded for an average distance of 4.31 mm).

It is worth noticing that for an average distance between control points of 5.5 mm , the value of the standard deviation is not increasing according to a trend, but a lack of consistency was shown (Fig. 5.12); the explanation for this phenomenon should be that if the average distance between control points is above a certain value, the result of the *eABOS* interpolation technique is highly dependant on the set of control points, thus the accuracy cannot be easily predict only considering the number of control points (or, equivalently, the average distance).

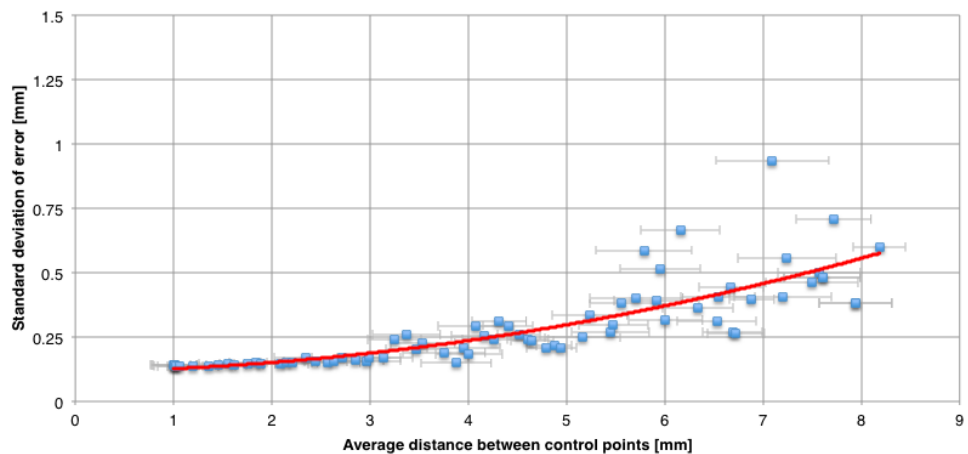


Figure 5.12: Results of the eABOS interpolation: standard deviation - The standard deviation of the error is evaluated vs the average minimum value of the distance between the control points.

For an average distance of about 5 mm (mean: 4.934 mm ; st. dev: 0.167 mm), the mean error is equal to 0.289 mm (st. dev: 0.208 mm), and both average value and standard deviation of the error increase consistently, showing a predictable behaviour; thus, an average distance of about 5 mm should be considered as an indication when acquiring the control points within the condyles area; for the area highlighted in Fig. 5.10, 23 control points were considered. The reconstructed surface, manually aligned with the phantom model, is shown in Fig. 5.13.

5. IMPLICIT ACTIVE CONSTRAINTS

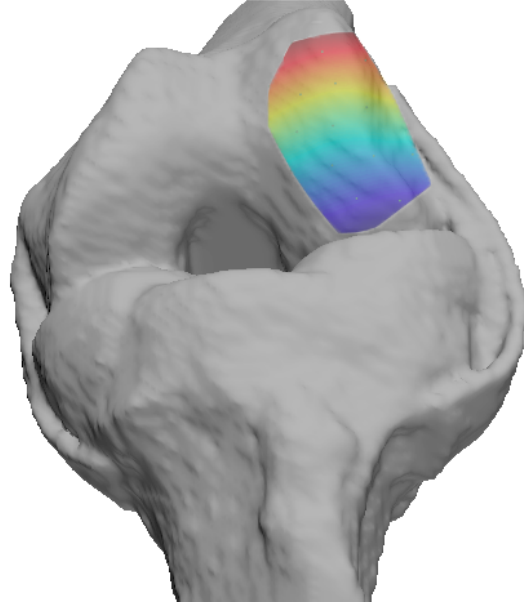


Figure 5.13: Comparison between the ground truth and the reconstructed surface - The reconstructed surface has been manually registered with the CT image. 23 control points were considered, being the average minimum distance equal to 4.9 mm.

5.3 Implicit evaluation of the trocar position

The instrument is required to always pass through the trocar; thus, the trocar can be defined as the intersection point of the directions of the rigid shaft of the laparoscopic instrument while performing a procedure (ideal condition). However, considering a real scenario, the trocar point can be defined as the point that minimises the cumulative square distance with all the lines representing the directions of the rigid shaft.

Being 0p_T the position of the trocar defined in the base reference frame, the square distance d_k^2 with the axis of the rigid shaft for the sample k is defined by:

$$d_k^2 = \|{}^0z_{b,k} \times ({}^0p_{b,k} - {}^0p_T)\|^2 \quad (5.24)$$

being ${}^0z_{b,k}$ and ${}^0p_{b,k}$ the z axis and the centre of the reference frame (x_b, y_b, z_b) in the robot base frame, respectively.

Thus, the commutative square distance D^2 has to be minimised in order to evaluate the trocar position, as:

$$D^2 = \sum_{k=1}^w d_k^2 \quad (5.25)$$

5. IMPLICIT ACTIVE CONSTRAINTS

being w the number of samples. The Nelder-Mead Simplex Method¹ can be used for solving the minimisation problem [20].

The trocar can be evaluated before starting executing the surgical procedure, considering the directions of the instrument when acquiring the control points for defining the pre-planned path or surface.

5.4 Subject tests

A minimally invasive laser chondroplasty was simulated for analysing the effects of the proposed control framework, and subject tests were performed.

A knee phantom (Sawbones Europe AB²) comprising femur, tibia, patella, menisci and ligaments was used. A synthetic tissue representing the skin and the muscles covers those internal structures. For simulating a minimally invasive procedure, the operating site was accessed through a small port created in the phantom and localised accordingly to a real scenario. Direct vision was not involved, and an endoscopic camera was user to view the operating site through another incision. The endoscope was connected with another LWR, acting as a fixed camera holder. Visual feedback was provided to the operator through a 2D screen.

At the beginning of this study, to validate the performances of the proposed control technique, a rigid instrument was used instead of the flexible one, so as to avoid any uncertainty due to the lack of a precise kinematic model of the flexible instrument caused by the absence of position and shape sensing (as discussed in Section 4.3.5). The experimental setup is shown in Fig. 5.14.

5.4.1 Experimental protocol

Twelve subjects (six males, six females), aged between 20 and 31 (mean age: 25.08; median value: 25), were involved in the experiment. All subjects, from various technical backgrounds (1 Chemistry, 1 Physics, 2 Computer science, 8 Engineering), were all tested to be right-handed with the Edinburgh Handedness Inventory [62] (average score: 82.83; minimum score: 43³).

¹C++ implementation available at <http://www.mikehutt.com/neldermead.html>

²<http://www.sawbones.com>

³According to the Edinburgh Handedness Inventory, a subject is right-handed if his score is higher than 40.

5. IMPLICIT ACTIVE CONSTRAINTS

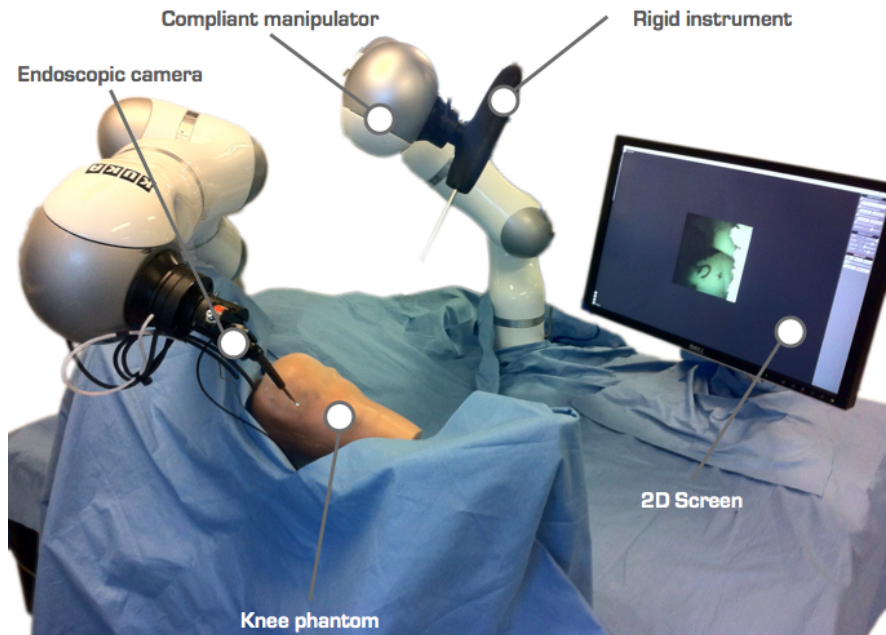


Figure 5.14: The experimental setup for the Subject tests - A minimally invasive chondroplasty was simulated within a knee phantom.

The subjects were instructed to move the instrument tip along a pre-defined path within the condyles area (Fig. 5.15), while keeping the instrument always passing through the incision port.

Each session of the experiment was composed by four different and consequential phases:

1. **Free motion of the instrument** - A training time was given to familiarise with the setup. A fixed maximum time was not defined, but the subject was asked to decide when to start the real test;
2. **Acquisition of the trocar point** - The location of this point was defined from the insertion of the instrument from three different orientations. The trocar was defined according to Section 5.3;
3. **Acquisition of the control points** - The subject was asked to acquire few control points for reconstructing the articular surface. In order to standardise the experiment, the control points were pre-defined on the condyles area and

5. IMPLICIT ACTIVE CONSTRAINTS

were not set arbitrarily by the user (the control points are marked with a cross “X” in Fig. 5.15);

4. **Path following** - The subject attempted to move the tip as accurate as possible to follow the path marked on the cartilage as well as to maintain the instrument passing through the incision port. He/she was also informed that the task time to completion is one of the performance indices.

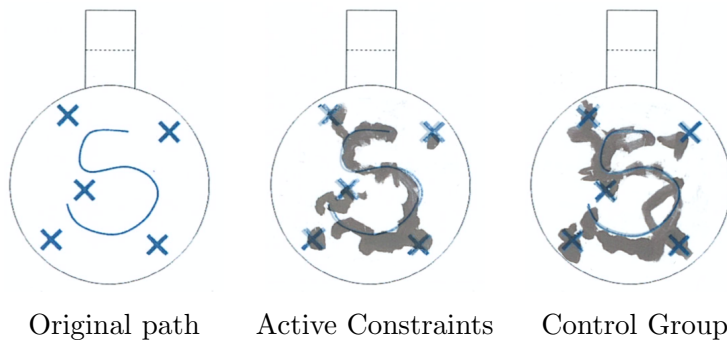


Figure 5.15: Pre-planned path on the articular cartilage - Subjects were asked to follow the pre-defined path on the articular cartilage shown in the left figure. Central and right picture are two examples of the path followed with orientation constrained and without orientation constrained, respectively.

A pen was added at the tip of the rigid instrument, in order to provide the subject with a feedback about the covered area.

The subjects repeated the same task twice. In the control execution (*Control Group*, which is acquired for measuring the performances in the *null hypothesis*, the subject could freely move the instrument, while the robot was not constraining his/her motion. In the other execution (*Active Constraints*), whose performances represent the *test hypothesis*, the robot actively constrained the orientation of the instrument in order to help the subject to keep instrument passing through incision port. The order of these two executions was randomised for eliminating the bias due to the learning effect.

At the end of the executions, subjects were asked to answer qualitatively, with a score from 1 to 6, to these three questions:

1. *Did you find it easy to constrain the instrument passing through the incision point, when you were NOT assisted by the robot? (1:extremely easy; 2: easy; 3: feasible; 4: a bit difficult; 5: difficult; 6: extremely difficult)*

5. IMPLICIT ACTIVE CONSTRAINTS

2. *Did you find it easy to constrain the instrument passing through the incision point, when you were assisted by the robot? (1:extremely easy; 2: easy; 3: feasible; 4: a bit difficult; 5: difficult; 6: extremely difficult)*
3. *Did you find it stressful to acquire the few control points at the beginning of the procedure? (1:extremely easy; 2: easy; 3: feasible; 4: a bit stressful; 5: stressful; 6: extremely stressful)*

5.4.2 Results

During the execution, the homogeneous transformation matrix 0T_b from the robot base frame to the proximal end of the rigid instrument was recorder; the operator's hand position 0p_b , supposed correspondent to the proximal end of the laparoscopic instrument, is defined by the forth column of the 0T_b matrix, while the instrument direction 0z_b is defined by its third column. The tip position 0p_c is easily evaluable multiplying 0T_b by the matrix bT_c defined in (3.2). The reconstructed surface (defined in the robot base frame) was recorded for evaluating the closest point ${}^0c^*$ to the instrument tip. The incision point 0p_T , defined implicitly, is also recorded.

The following performances index were considered:

1. **Time to completion** - The time to completion represents the time the subject needs for covering the whole path. The time to completion for all the subjects is shown in Fig. 5.16.
2. **Orientation error** - The orientation error represents the distance between the instrument axis and the trocar position. It is evaluated as the displacement between the point 0p_T and the line oriented as 0z_b and passing through 0p_b . The error ϵ_O can be defined by:

$$\epsilon_O = \|{}^0z_b \times ({}^0p_b - {}^0p_T)\| \quad (5.26)$$

The mean value for all the subjects is represented in Fig. 5.17.

3. **Intracorporeal error** - The intracorporeal error ϵ_I is the distance between the instrument tip position 0p_c and the closest point ${}^0c^*$ within the predefined surface:

$$\epsilon_I = \|{}^0p_c - {}^0c^*\| \quad (5.27)$$

The mean value for all the subjects is shown in Fig. 5.18.

5. IMPLICIT ACTIVE CONSTRAINTS

4. **Extracorporeal error** - The extracorporeal error is defined as the distance between the real position of the subject's hand (supposed coincident with the proximal end of the laparoscopic instrument 0p_b), and the position he should have had for having the instrument passing through the trocar and in contact with the pre-defined region. Being ${}^0c^*$ the closest point to the instrument tip, the extracorporeal error ϵ_E is defined as:

$$\epsilon_0 = \left\| {}^0p_b - \left[{}^0c^* - L \frac{{}^0c^* - {}^0p_T}{\| {}^0c^* - {}^0p_T \|} \right] \right\| \quad (5.28)$$

where L is the length of the instrument, and 0p_T is the trocar position. A graphical representation of the meaning of the extracorporeal error is shown in Fig. 5.19. Results for all the subjects are represented in Fig. 5.20.

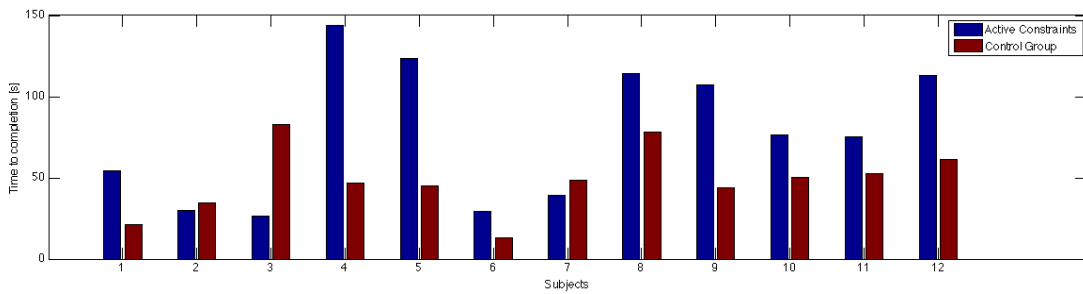


Figure 5.16: Time to completion - All subjects (s) - The time to completion is defined as the time used for completing the task of following the pre-defined path.

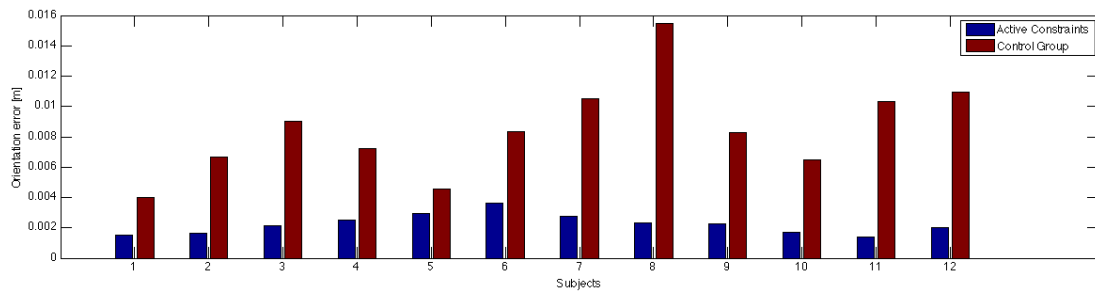


Figure 5.17: Orientation error - All subjects (mm) - The orientation error is defined as the mean distance between the instrument axis and the trocar point.

Increased time to completion and intracorporeal error were shown when the orientation was constrained, while reduced orientation and extracorporeal errors were shown for almost all the subjects.

5. IMPLICIT ACTIVE CONSTRAINTS

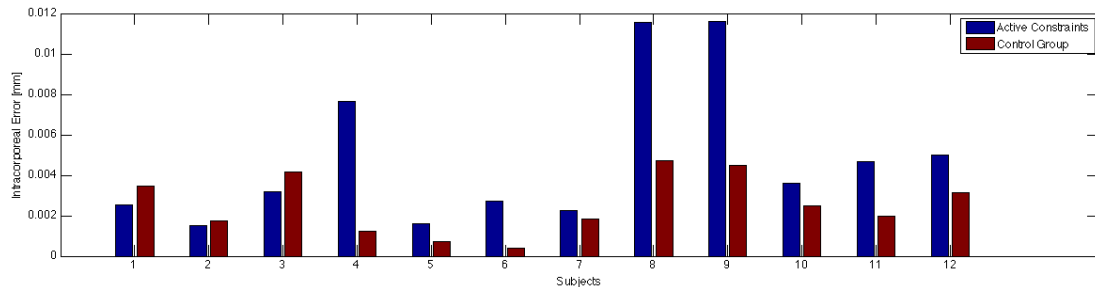


Figure 5.18: Intracorporeal error - All subjects (mm) - The intracorporeal error is defined as the mean distance between the instrument tip and the closest point within the pre-defined region.

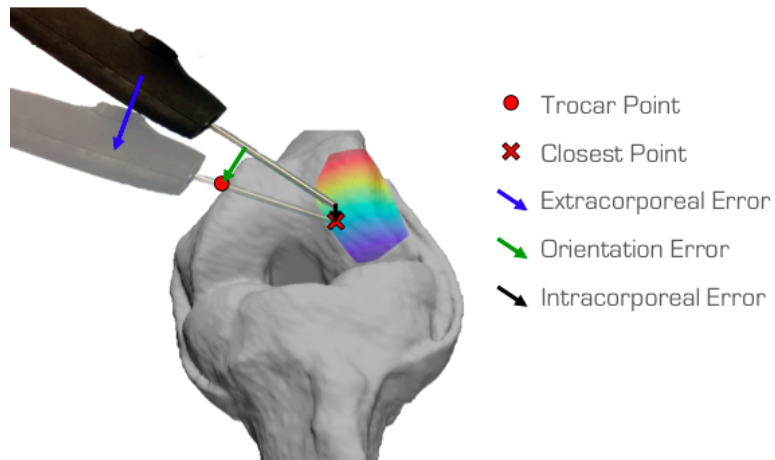


Figure 5.19: Intracorporeal, Extracorporeal and Orientation errors - They represent the error between the effective and desired tip position (intracorporeal error), the instrument axis and the trocar point (orientation error) and the effective and desired subject's hand position (extracorporeal error).

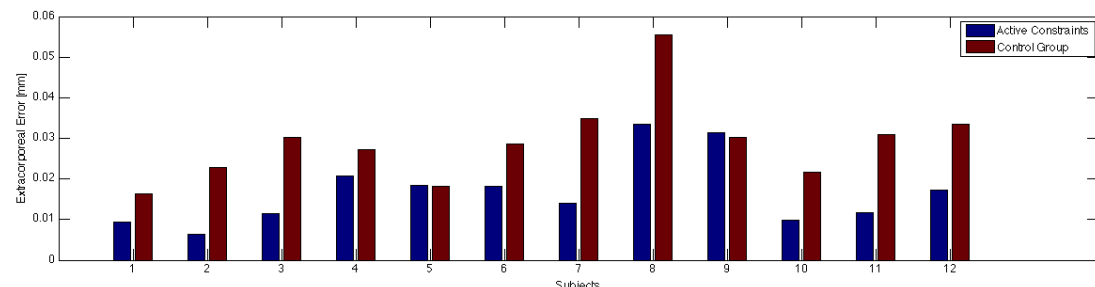


Figure 5.20: Extracorporeal error - All subjects (mm) - The extracorporeal error is defined as the mean distance between the real position of the subject's hand and the position he should have had for having the instrument passing through the trocar point and its tip in contact with the pre-defined region.

5. IMPLICIT ACTIVE CONSTRAINTS

Before performing a comparative analysis of the statistical significance of the performance indices, results were tested to have a normal distribution. The Lilliefors (Kolmogorov-Smirnov) normality test was used. Thus, equality of variance distributions was checked visually using the Quantile-Quantile plots (Fig. 5.21) and numerically using the F-Test. Apart from the extracorporeal error, which has equal variance distributions for both groups, all other performance indices showed different variance distributions between groups.

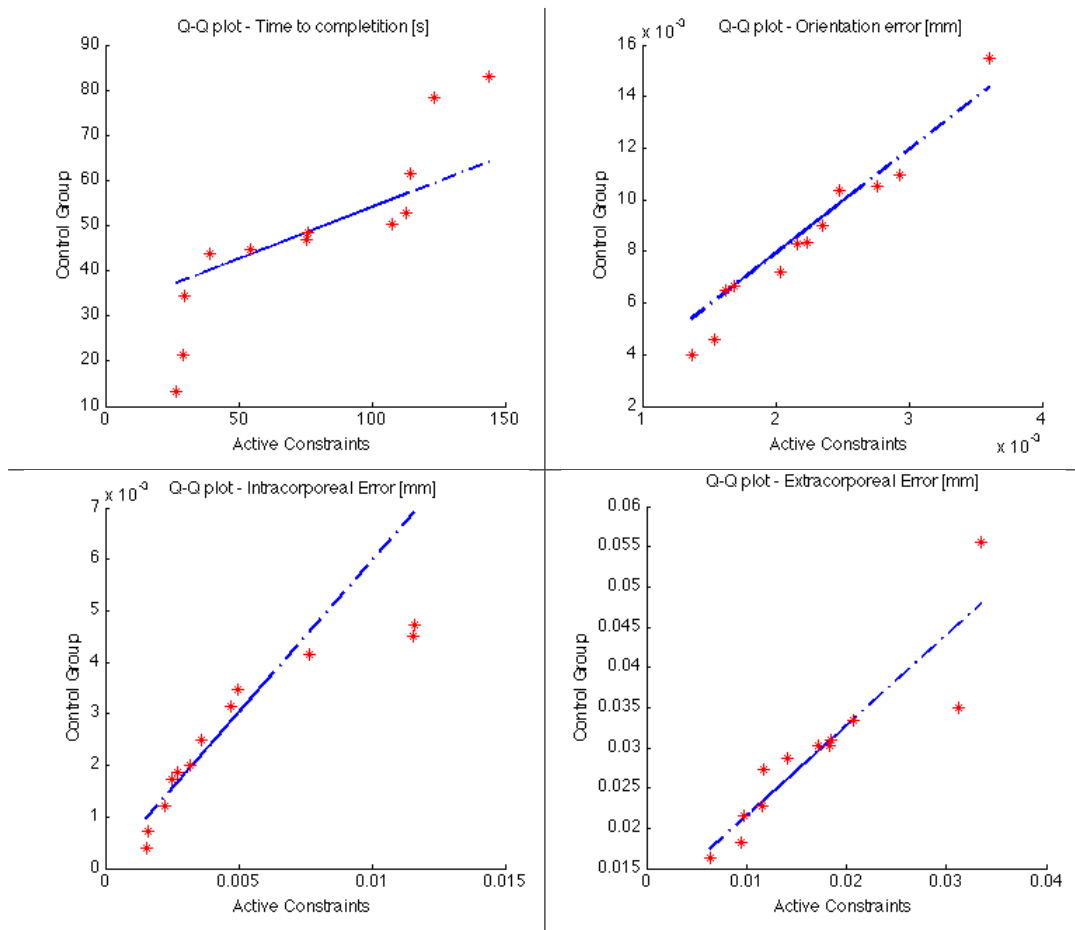


Figure 5.21: Quantile-Quantile Plots (Q-Q Plots) for the analysed data - The Q-Q Plots were used for analysing the equality in variance distributions.

Since all the performance indices have a normal distribution, statistical significance was evaluated with the T-Test for unequal variance distributions (apart from the extracorporeal error, which was tested with the T-Test for equal variance distributions).

5. IMPLICIT ACTIVE CONSTRAINTS

All tests (Lilliefors test, F-Test, T-Test) were performed with a significance level equal to 5%. Results are shown in Fig. 5.22. The time to completion increases when the orientation constraint is applied, while the orientation error and the extracorporeal error are reduced. The intracorporeal error is not statistically significant.

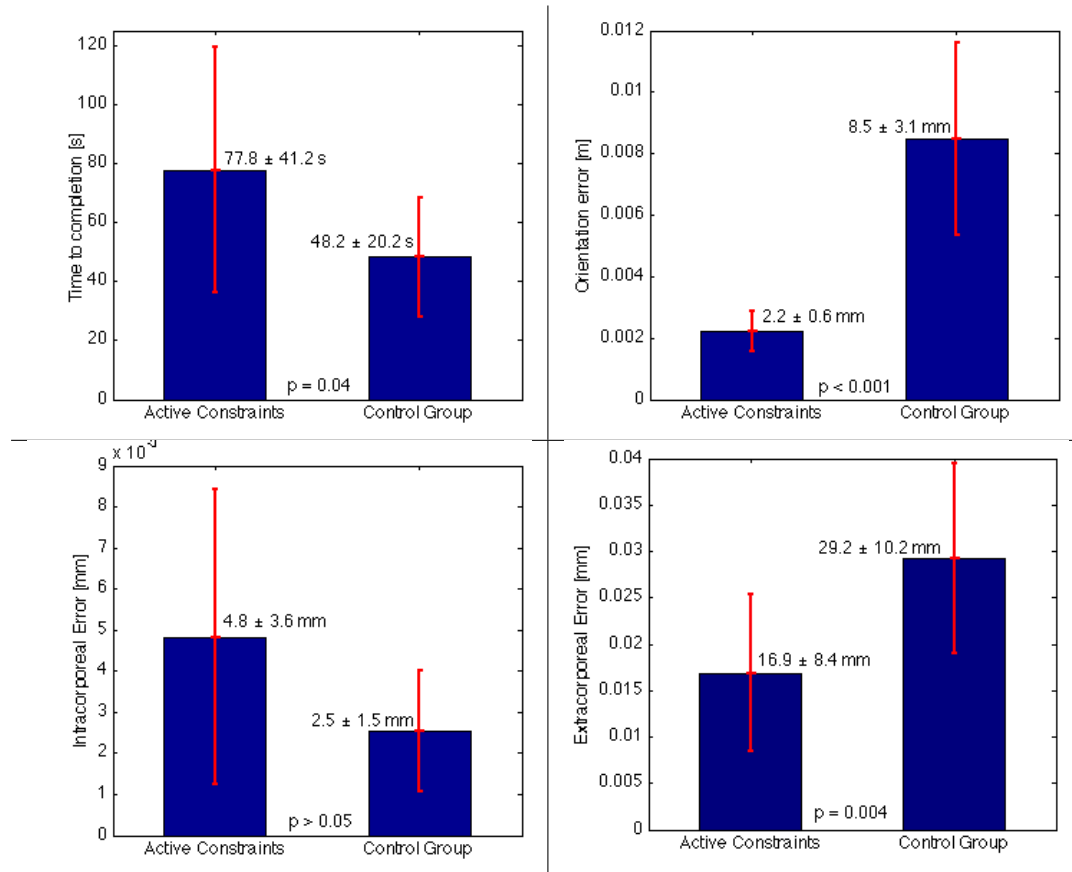


Figure 5.22: Analysis of the performance indices - A statistical analysis was performed for checking whether or not differences between the Active Constraints results and the Control Group results are significant.

Question 1 and 2 of the qualitative survey are aimed to evaluate the user's perception of the task complexity; a reduction in the perceived task complexity is expected to allow the user to handle more in other tasks. Question 1 was asked for measuring the *null hypothesis*, while Question 2 was asked for measuring the *test hypothesis*. Results for all the subjects are represented in Fig. 5.23.

Neither the *test hypothesis* nor the *null hypothesis* have a normal distribution; thus, for analysing the statistical significance of the improvement, the Wilcoxon Rank Sum

5. IMPLICIT ACTIVE CONSTRAINTS

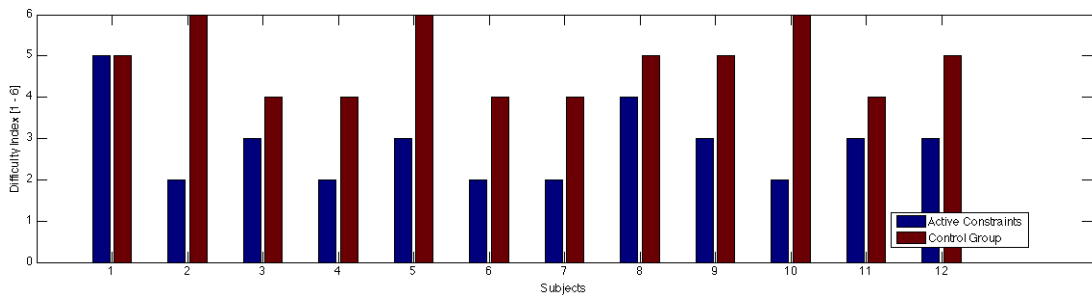


Figure 5.23: Difficulty index (qualitative survey) - All subjects - Score is between 1 (extremely easy) and 6 (extremely difficult).

Test was used. A reduction of 2 points in the difficulty index was evaluated, being the value highly significant (p value lower than 0.001), as shown in Fig. 5.24. The mean score is equal to 2.4 (being 2 = “easy” and 3 = “feasible”).

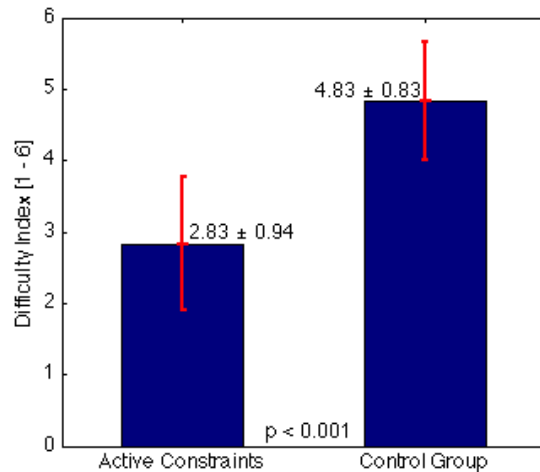


Figure 5.24: Difficulty index (qualitative survey) - Statistical analysis - A statistical analysis was performed for checking whether or not differences between the Active Constraints results and the Control Group results are significant.

For evaluating the ergonomics of the proposed control system, the question number 3 of the survey can be analysed. Results are shown in Fig. 5.25. Overall, the acquisition of the control points was evaluated between “easy” and “feasible” (mean score: 2.4).

All the results are quoted in Table 5.3, where also the p -values from the Lilliefors (Kolmogorov-Smirnov) test and the F-Test are shown.

5. IMPLICIT ACTIVE CONSTRAINTS

Table 5.3: Results of the Subject tests: performance indices.

Performance index	Active Constraints			Control Group			F-Test (p-value) ^b	Significance (p-value) ^c
	Mean	St. Dev.	Normality ^a	Mean	St. Dev.	Normality ^a		
Time to completion [s]	77.8	41.8	0.36	48.2	20.2	> 0.5	0.02	0.04
Orientation error [mm]	2.2	0.6	> 0.5	8.5	3.1	> 0.5	< 0.001	< 0.001
Intracorporeal error [mm]	4.8	3.6	0.07	2.5	1.5	> 0.5	0.006	0.06
Extracorporeal error [mm]	16.9	8.4	0.36	29.2	10.2	0.18	0.54	0.004
Difficulty index	2.8	0.9	0.02	4.8	0.8	0.03	0.71	< 0.001

^a. Normal distribution is checked with the Lilliefors (Kolmogorov-Smirnov) test. Values represent the p-value for a significance level

α equal to 5%.

^b. Significance level α is equal to 5%.

^c. If normal distribution is met for both active constraints and control groups, a T-Test is applied (for equal or unequal variance distributions, according to the results of the F-Test); otherwise, the Wilcoxon Rank Sum Test is used. Significance level α is equal to 5%.

5. IMPLICIT ACTIVE CONSTRAINTS

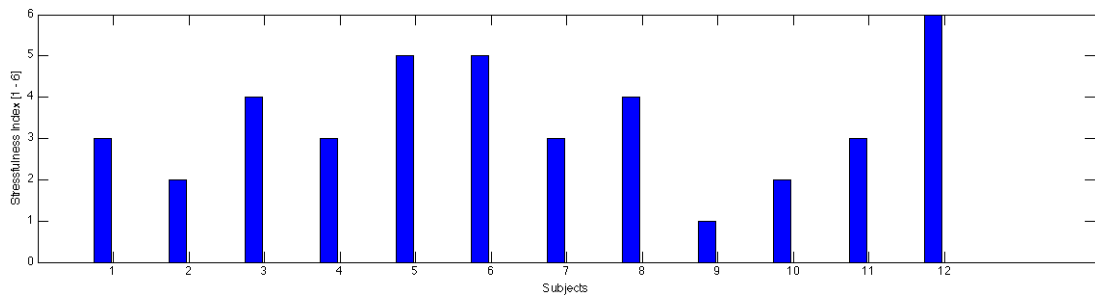


Figure 5.25: Control ergonomics - Acquisition of control points - All subjects were asked to evaluate qualitatively how much acquiring the control points for reconstructing the articular surface was stressful.

5.4.3 Specification for the flexible instrument

The range of bending defines the amount of surface that is possible to cover with an optimal approach direction. Thus, the measurements acquired during the subject tests were also used for evaluating the optimal range of motion R and the centre of motion C (*i.e.* the central position in the total range $2 \cdot R$), as shown in Fig. 5.26. Increasing the range of motion R from 0 to $\pi/4$, the optimal centre of motion C for covering the highest amount of surface with the optimal approach direction was evaluated.



Figure 5.26: Illustration of the centre of motion C and the range of motion R
- For the considered flexible instrument, it is possible to define the range of motion ($\pm R$) around the central position C .

Fig. 5.26 represents the amount of surface that can be covered. The red numbers represent the optimal centre of motion C . For example, when considering 60% of the total surface, a range of motion of plus/minus 15° is sufficient, being the central position oriented at 49° from the instrument shaft direction.

5. IMPLICIT ACTIVE CONSTRAINTS

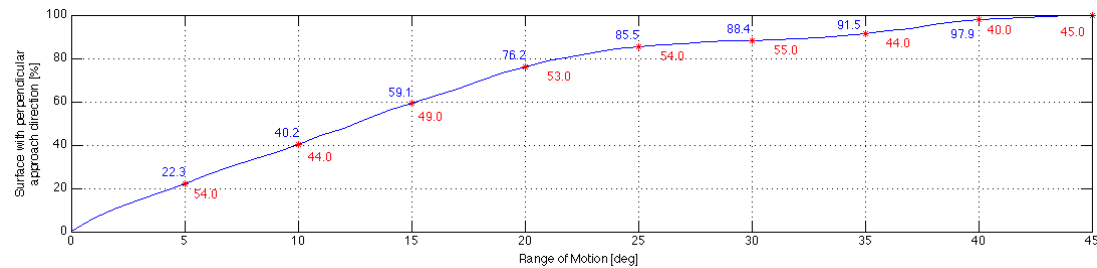


Figure 5.27: Evaluation of the centre of motion C and the range of motion R

- Varying the range of motion from 0° to 45° , it is possible to cover an amount of surface indicated with the blue line with an optimal approach direction. The optimal range of motion C is typed in red numbers (in degrees).

5.4.4 Discussion

Results from the subject tests were statistically analysed, as explained in the previous Section.

Increase of time to completion was found when the Active Constraints technique was applied (from 48.2 s to 77.8 s). This can be considered as a consequence of the disorientation due to the mirrored movements that have to be executed when the trocar constraint is applied. It is worth noticing that no subjects have a minimally invasive surgical background, thus none was used to dealing with the trocar constraint, which is actually always active during a minimally invasive procedure.

The reduction in the orientation error, measured as the mean distance between the axis representing the instrument shaft and the trocar point, was statistically significant ($p\text{-value} < 0.001$), and its mean value was reduced to about one quarter (from 8.5 mm to 2.2 mm). Thus, the Active Constraints technique may lead to reduced damages to the patient's skin and tissues.

On the other side, the intracorporeal error, measured as the mean distance between the instrument tip and the pre-defined surface, is bigger when constraints were applied. However, the result is not statistically significant ($p\text{-value} > 0.05$).

The extracorporeal error can be considered as a performance index of the overall system, since it takes into account both intracorporeal error and orientation errors, as shown in Fig. 5.19. This error is almost halved (from 29.2 mm to 16.9 mm), showing a significant enhancement in the performances, being the $p\text{-value}$ lower than 0.005 .

5. IMPLICIT ACTIVE CONSTRAINTS

The procedure for acquiring the control points is intuitive and effective, and it does not represent a drawback of the proposed method. Moreover, it is worth noticing that this technique avoids the use of pre-operative imaging, reducing the radiation dose to patients and not requiring images registration.

5.5 Conclusions

In this Chapter, two techniques for reconstructing the surface where the instrument should be constrained on and for evaluating the position of the trocar have been proposed, allowing to *implicitly* define the constraints that should be considered in the 6 DoFs Active Constraints technique introduced in Chapter 3. Only few points are required, and the constraints are evaluated automatically from the surgeon's initial movements, without requiring complicated manual inputs.

The ABOS surface reconstruction technique proposed by Dressler [21] has been modified for being applied in a surgical scenario, where bijection can not be trivially assured, resulting in an algorithm fast enough for real-time applications, which provides a surface continuous enough for the considered application (continuity can be assured in C^1 or C^2 according to the post-smoothing interpolation technique; other interpolation techniques might be considered for assuring higher continuity), defining also the normal direction; the technique has been validated, and an average distance of 5 mm has been provided as an optimal indication when considering the application of reconstructing the condyles area.

Moreover, for implicitly defining the trocar position, an optimisation problem has been introduced, which considers the first movements of the surgeon.

For validating the whole setup, and for checking whether or not the proposed system can increase the surgical performances, a subject tests were performed, involving 12 subjects and simulating a minimally invasive surgical procedure.

The subject tests demonstrated an enhancement in the accuracy, reducing the orientation error to about one quarter and almost halving the extracorporeal error, that can be considered as a performance index for the whole system, while an increase in the time to completion was recorder. The ergonomics of the acquisition of the control points for reconstructing the surface was qualitative evaluated, through a survey. More-

5. IMPLICIT ACTIVE CONSTRAINTS

over, a perceived reduction of the difficulty was reported when the Active Constraints technique was applied, allowing the subjects to focus more on other tasks.

However, the flexible instrument was not considered, since the lack of shape sensing does not allow to measure its pose when contacts happen during the procedure.

Chapter 6

Conclusions

6.1 Achievement of this thesis

In this thesis, a robotic system for minimally invasive knee laser chondroplasty has been developed with the aim to design a precise, safe and ergonomic platform for the treatment of early-stage knee arthritis. This disease has the highest incidence and prevalence among people older than forty-five, when compared to other joints arthritis, such as hands arthritis or hips arthritis [46, 63]. Knee arthritis represents the major cause of disability in many activities, such as walking, carrying bundles and housekeeping [27]. The benefits of chondroplasty using lasers have been well documented. The laser light can be transmitted via a boundless of flexible thin optical fibres, simplifying the integration with flexible instruments. No contact forces are required. Thermal necrosis zones can be minimised and high-quality haemostat control can be achieved [9, 34, 52, 76]. Furthermore, micro-confocal images can be acquired simultaneously through the same optical fibres while performing the arthroscopic procedure, enhancing the understanding of pathological and structural information [47].

The research objective of this thesis was to design a **safe** surgical system, which can enhance the surgical performances, coping with the constraints of a minimally invasive procedure. In a minimally invasive procedure the instrument has always to be inserted through the incision point, and the orientation of the instrument has to be constrained in order to avoid excessive tissues injuries around the trocar position. Moreover, since the layer of the cartilage that has to be ablated is relatively thin, the manipulation has to be constrained and guided within a pre-defined region; the surface has to be acquired

6. CONCLUSIONS

in a quick and intuitive manner from a set of sparse control points, in order to reduce the setup time. Limb re-positionings during the procedure were taken into account when designing a control law capable to adapt to the dynamic surgical environment. For increasing the cartilage ablation rate, the instrument has to be as perpendicular as possible to the articular surface.

The proposed setup consists of a KUKA LWR 4+ coupled with a flexible instrument, capable of rotating around its longitudinal axis and of bending. The KUKA LWR 4+ has been specifically designed for working safely in contact with human subjects in an unstructured environment. The features of its compliant control were used for providing the operator with motion constraints and guidance in manoeuvring the instrument.

Technically, a comprehensive control framework has been proposed, and the contributions of this thesis can be summarised by the following five aspects:

- **6 DoFs Active Constraints.** The 3 DoFs Virtual Fixtures law introduced by Davis, Bettini *et al.* [10, 11, 19, 54] has been extended. In Chapter 3, an impedance (6×6) matrix has been proposed for constraining both instrument orientation and tip position, correlating the end-effector linear and angular velocity to the control force and torque. It represents a general control framework that can be applied to any manipulator capable of providing 6 DoFs in the Cartesian space. The control law was also designed for incorporating articulated laparoscopic instruments, such as flexible instruments or snake-like robots;
- **Promising control stability.** In Chapter 3, the proposed control law has been proved to be stable and robust, simulating frequency-known disturbances. A unique feature of the KUKA LWR 4+ control system was exploited. Therefore, the **safety** of the proposed setup was demonstrated and can be guaranteed;
- **Intuitive definition of surgical regions.** A surface interpolation technique for *in situ* reconstruction of anatomical surfaces, where the instrument tip has to be constrained on, has been developed in Chapter 5. It is an extension of the Approximation Based on Smoothing technique newly introduced for geophysical applications [21]. This interpolation technique allows to reconstruct the articular surface from a set of sparse and not-ordered control points. It provides a smooth surface, guaranteeing C^1 continuity. The surface normal is also evaluated considering the local curvature. The algorithm is processed sufficiently fast for real

6. CONCLUSIONS

time applications. The surface interpolation technique has been validated, and criteria for the selection of the control points were also described in detail;

- **Incorporation of additional DoFs.** A 2 DoFs flexible instrument has been introduced in Chapter 4 for increasing the rate of laser ablation conducted on the cartilage. The additional DoFs increase the accessibility to the target anatomy, with larger reachable and dexterous workspaces. The 6 DoFs Active Constraints technique has been modified and extended, incorporating the additional DoFs of the flexible instrument. The instrument configuration can be automatically adjusted for accessing the reconstructed surface with an optimal orientation;
- **Dynamically adaptation under changes of knee configuration.** Limb re-positionings commonly take place during the procedure. The proposed control law has been extended in Chapter 4 to be able to adapt to this dynamic surgical environment. An optical tracking system was introduced, and a quick calibration algorithm for registering the tracking system base frame within the robot base frame has been proposed.

To understand the practical value of the proposed control framework, performances analysis was conducted on a group of subjects. The flexible instrument was not used during the Subject Tests, since its pose can not be accurately predicted due to the lack of shape sensing. Only the orientation of the instrument was constrained, while the motion of the instrument tip was not confined within the pre-defined region.

The Subject Tests results have demonstrated a statistically significant enhancement in the accuracy, almost halving the extracorporeal error, that can be considered as an overall accuracy index of the system, taking into account both orientation and position errors.

Furthermore, the control ergonomics has been qualitatively measured through a survey, which reported a reduction of the perceived difficulties in maintaining the instrument passing through the incision point, thus allowing the surgeon to focus on other tasks.

6. CONCLUSIONS

6.2 Ongoing research and future directions

Precise shape sensing will be embedded within the flexible instrument to estimate an accurate kinematics. A fibre optics shape sensor can be used, as discussed in Section 4.3.5; alternatively, the tendons tension might be measured for having a feedback for closed loop control. Once the shape sensor is integrated and the kinematics of the flexible instrument is fully and accurately defined, not only the orientation of the instrument can be constrained, but also its tip motion can be properly guided according to the surgical plane; the additional constraint on the tip motion is expected to further reduce the intracorporeal error, and consequently the extracorporeal error, enhancing the overall accuracy and safety of the procedure.

Accidental collisions between the instrument and the surrounding tissues were not considered; incorporation of Proximity Queries, which is a process to compute the shortest distance among objects, can be used for preventing potential collisions, as anticipated in Section 2.4.2. A sub-optimal configuration for the flexible instrument can be defined for avoiding contacts while approaching the articular cartilage surface with an optimal access orientation. An optimisation-based problem might be formulated for defining the sub-optimal configuration for all the control points, evaluating a proper bending angle and a proper rotation angle for the flexible instrument. These parameters will then be used as additional inputs to the eABOS surface interpolation technique, allowing to define a 5 dimensions iper-surface, which will represent the optimal pose of the KUKA LWR 4+ and the optimal configuration of the flexible instrument, for all the points within the pre-defined region.

Bibliography

- [1] Quantum Coblation - Paragon T2 (<http://quantumcoblation.com/paragonT2.aspx>). 18
- [2] J. J. ABBOTT, G. D. HAGER, A. M. OKAMURA. Steady-hand teleoperation with virtual fixtures. In Robot and Human Interactive Communication, 2003. Proceedings. ROMAN 2003. The 12th IEEE International Workshop on (2003) 145–151. 27
- [3] A. ALBU-SCHAFFER, S. HADDADIN, C. OTT, A. STEMMER, T. WIMBOCK, G. HIRZINGER. The DLR lightweight robot: design and control concepts for robots in human environments. *Industrial Robot-an International Journal* (2007); **34**(5):376–385. 8
- [4] R. D. ALTMAN, J. KATES, L. E. CHUN, D. D. DEAN, D. EYRE. Preliminary observations of chondral abrasion in a canine model. *Annals of the Rheumatic Diseases* (1992); **51**(9):1056–1062. 15
- [5] A. M. ANDREW. Another efficient algorithm for convex hulls in two dimensions. *Information Processing Letters* (1979); **9**(5):216–219. 85
- [6] M. H. ANG, V. D. TOURASSIS. Singularities of Euler and Roll-Pitch-Yaw Representations. *Aerospace and Electronic Systems, IEEE Transactions on* (1987); **AES-23**(3):317–324. 36
- [7] ARTHRITISCARE.ORG.UK. Arthritis Care - Annuak Report 2010. Tech. rep. (2010). xii, 1, 13
- [8] H. AZIMIAN, R. V. PATEL, M. D. NAISH. On constrained manipulation in robotics-assisted minimally invasive surgery. In Biomedical Robotics and Biomechatronics (BioRob), 2010 3rd IEEE RAS and EMBS International Conference on (2010) 650–655. 24
- [9] M. BERNARD, M. GROTHUES-SPORK, P. HERTEL, Y. MOAZAMI-GOUDARZI. Reactions of meniscal tissue after arthroscopic laser application: An in vivo study using five different laser systems. *Arthroscopy: The Journal of Arthroscopic and Related Surgery* (1996); **12**(4):441–451. 15, 16, 18, 117
- [10] A. BETTINI, S. LANG, A. OKAMURA, G. HAGER. Vision assisted control for manipulation using virtual fixtures. In Intelligent Robots and Systems, 2001. Proceedings. 2001 IEEE/RSJ International Conference on, vol. 2 (2001) 1171–1176 vol.2. 27, 28, 31, 118
- [11] A. BETTINI, P. MARAYONG, S. LANG, A. M. OKAMURA, G. D. HAGER. Vision-assisted control for manipulation using virtual fixtures. *Robotics, IEEE Transactions on* (2004); **20**(6):953–966. 27, 31, 118

BIBLIOGRAPHY

- [12] E. M. BOCTOR, R. J. WEBSTER 3RD, H. MATHIEU, A. M. OKAMURA, G. FICHTINGER. Virtual remote center of motion control for needle placement robots. *Computer aided surgery : official journal of the International Society for Computer Aided Surgery* (2004); **9**(5):175–183. 21, 24
- [13] G. BRISSON, T. KANADE, A. DiGIOIA, B. JARAMAZ. Precision freehand sculpting of bone. In C. BARILLOT, D. R. HAYNOR, P. HELLIER, eds., *Medical Image Computing and Computer-Assisted Intervention - Miccai 2004, Pt 2, Proceedings, vol. 3217, 105–112* (Springer-Verlag Berlin, Berlin, 2004). 20
- [14] N. CHAKRABORTY, P. JUFENG, S. AKELLA, J. E. MITCHELL. Proximity Queries Between Convex Objects: An Interior Point Approach for Implicit Surfaces. *Robotics, IEEE Transactions on* (2008); **24**(1):211–220. 25
- [15] J. E. COLGATE. Robust impedance shaping telemanipulation. *Robotics and Automation, IEEE Transactions on* (1993); **9**(4):374–384. 26
- [16] M. CONDITT. History of Robots in Orthopedics. In J. ROSEN, B. HANNAFORD, R. M. SATAVA, eds., *Surgical Robotics*, 661–677 (Springer US, 2011). 20
- [17] P. DARIO, M. C. CARROZZA, M. MARCACCI, S. D'ATTANASIO, B. MAGNAMI, O. TONET, G. MEGALI. A novel mechatronic tool for computer-assisted arthroscopy. *Information Technology in Biomedicine, IEEE Transactions on* (2000); **4**(1):15–29. 5, 9, 18
- [18] B. DAVIES, M. JAKOPEC, S. J. HARRIS, F. RODRIGUEZ Y BAENA, A. BARRETT, A. EVANGELIDIS, P. GOMES, J. HENCKEL, J. COBB. Active-Constraint Robotics for Surgery. *Proceedings of the IEEE* (2006); **94**(9):1696–1704. 20
- [19] B. L. DAVIES, S. J. HARRIS, W. J. LIN, R. D. HIBBERD, R. MIDDLETON, J. C. COBB. Active compliance in robotic surgery - the use of force control as a dynamic constraint. *Proceedings of the Institution of Mechanical Engineers Part H-Journal of Engineering in Medicine* (1997); **211**(4):285–292. 27, 118
- [20] J. E. DENNIS, D. J. WOODS. Optimization of Microcomputers: The Nelder-Mead Simplex Algorithm. In A. WOUK, ed., *New computing environments: microcomputers in large-scale computing*, chap. 9, 116–122 (SIAM, 1987). 103
- [21] M. DRESSLER. Interpolation methods for construction of surfaces. Ph.D. thesis, Technical University of Liberec (2007). 10, 83, 84, 115, 118
- [22] A. ESCANDE, S. MIOSSEC, A. KHEDDAR. Continuous gradient proximity distance for humanoids free-collision optimized-postures. In *Humanoid Robots, 2007 7th IEEE-RAS International Conference on* (2007) 188–195. 25
- [23] E. G. GILBERT, D. W. JOHNSON, S. S. KEERTHI. A fast procedure for computing the distance between complex objects in three-dimensional space. *Robotics and Automation, IEEE Journal of* (1988); **4**(2):193–203. 25, 26
- [24] P. GOMES. Surgical robotics: Reviewing the past, analysing the present, imagining the future. *Robotics and Computer-Integrated Manufacturing* (2011); **27**(2):261–266. 20, 21

BIBLIOGRAPHY

- [25] S. GOTTSCHALK, M. C. LIN, D. MANOCHA. OBBTree: a hierarchical structure for rapid interference detection (1996). 28
- [26] E. GRIFFITHS, V. KHANDUJA. Hip arthroscopy: evolution, current practice and future developments. *International Orthopaedics* (2012); Under publ. 4
- [27] A. A. GUCCIONE, D. T. FELSON, J. J. ANDERSON, J. M. ANTHONY, Y. ZHANG, P. W. F. WILSON, M. KELLY-HAYES, P. A. WOLF, B. E. KREGER, W. B. KANNEL. The effects of specific medical conditions on the functional limitations of elders in the Framingham Study. *American Journal of Public Health* (1994); **84**(3):351–358. 2, 3, 117
- [28] G. S. GUTHART, J. K. SALISBURY JR. The Intuitive telesurgery system: overview and application. In Robotics and Automation, 2000. Proceedings. ICRA '00. IEEE International Conference on, vol. 1 (2000) 618–621 vol.1. 21
- [29] S. HADDADIN, A. ALBU-SCHAFFER, A. DE LUCA, G. HIRZINGER. Collision detection and reaction: A contribution to safe physical Human-Robot Interaction. In Intelligent Robots and Systems, 2008. IROS 2008. IEEE/RSJ International Conference on (2008) 3356–3363. 8
- [30] B. HAGAG, R. ABOVITZ, H. KANG, B. SCHMITZ, M. CONDITT. RIO: Robotic-Arm Interactive Orthopedic System MAKoplasty: User Interactive Haptic Orthopedic Robotics. In J. ROSEN, B. HANNAFORD, R. M. SATAVA, eds., *Surgical Robotics*, 219–246 (Springer US, 2011). 18, 20
- [31] S. C. HO, R. D. HIBBERD, B. L. DAVIES. Robot assisted knee surgery. *Engineering in Medicine and Biology Magazine, IEEE* (1995); **14**(3):292–300. 26
- [32] E. B. HUNZIKER. Articular cartilage repair: basic science and clinical progress. A review of the current status and prospects. *Osteoarthritis and Cartilage* (2002); **10**(6):432–463. 1, 15
- [33] C. HYO-JEONG, Y. BYUNG-JU. Modeling of a constraint force at RCM point in a needle insertion task. In Mechatronics and Automation (ICMA), 2011 International Conference on (2011) 2177–2182. 24
- [34] A. B. IMHOFF. The use of lasers in orthopaedic surgery. *Operative Techniques in Orthopaedics* (1995); **5**(3):192–203. 15, 16, 117
- [35] R. W. JACKSON, C. DIETERICH. The results of arthroscopic lavage and debridement of osteoarthritic knees based on the severity of degeneration. *Arthroscopy: The Journal of Arthroscopic and Related Surgery* (2003); **19**(1):13–20. 13, 14
- [36] W. G. JACOBY. Regression III: Advanced Methods (<http://polisci.msu.edu/jacoby/icpsr/regress3/>) (2005). 85, 87
- [37] M. JAKOPEC, S. J. HARRIS, R. Y. BAENA, P. GOMES, B. L. DAVIES. The Acrobot (R) system for total knee replacement. *Industrial Robot-an International Journal* (2003); **30**(1):61–66. 20, 28
- [38] M. JAKOPEC, F. RODRIGUEZ Y BAENA, S. J. HARRIS, P. GOMES, J. COBB, B. L. DAVIES. The hands-on orthopaedic robot "acrobot": Early clinical trials of total knee replacement surgery. *Robotics and Automation, IEEE Transactions on* (2003); **19**(5):902–911. 20, 26

BIBLIOGRAPHY

- [39] B. T. KELLY, D. E. WEILAND, M. L. SCHENKER, M. J. PHILIPPON. Arthroscopic Labral Repair in the Hip: Surgical Technique and Review of the Literature. *Arthroscopy: The Journal of Arthroscopic and Related Surgery* (2005); **21**(12):1496–1504. 4
- [40] B. T. KELLY, R. J. WILLIAMS, M. J. PHILIPPON. Hip Arthroscopy: Current Indications, Treatment Options, and Management Issues . *The American Journal of Sports Medicine* (2003); **31**(6):1020–1037. 4
- [41] R. KIKUWE, N. TAKESUE, H. FUJIMOTO. A Control Framework to Generate Nonenergy-Storing Virtual Fixtures: Use of Simulated Plasticity. *Robotics, IEEE Transactions on* (2008); **24**(4):781–793. 26
- [42] Y. H. KIM, H. L. MINH. A Laboratory-level Surgical Robot System for Minimal Invasive Surgery (MIS) Total Knee Arthroplasty. *International Journal of Precision Engineering and Manufacturing* (2011); **12**(2):237–242. 19
- [43] K. W. KWOK, G. P. MYLONAS, L. W. SUN, M. LEROTIC, J. CLARK, T. ATHANASIOU, A. DARZI, G. Z. YANG. Dynamic Active Constraints for Hyper-Redundant Flexible Robots. In G. Z. YANG, D. HAWKES, D. RUECKERT, A. NOBEL, C. TAYLOR, eds., *Medical Image Computing and Computer-Assisted Intervention - Miccai 2009*, Pt I, Proceedings, vol. 5761, 410–417 (Springer-Verlag Berlin, Berlin, 2009). 29
- [44] K. W. KWOK, K. H. TSOI, V. VITIELLO, J. CLARK, G. C. T. CHOW, W. LUK, G. Z. YANG. Dimensionality Reduction in Controlling Articulated Snake Robot for Endoscopy under Dynamic Active Constraints. *Submitted to IEEE Trans. on Robotics* ; . 25, 29
- [45] K. W. KWOK, V. VITIELLO, G. Z. YANG. Control of Articulated Snake Robot under Dynamic Active Constraints. In T. JIANG, N. NAVAB, J. P. W. PLUIM, M. A. VIERGEVER, eds., *Medical Image Computing and Computer-Assisted Intervention - Miccai 2010*, Pt Iii, vol. 6363, 229–236 (Springer-Verlag Berlin, Berlin, 2010). 29
- [46] R. C. LAWRENCE, D. T. FELSON, C. G. HELMICK, L. M. ARNOLD, H. CHOI, R. A. DEYO, S. GABRIEL, R. HIRSCH, M. C. HOCHBERG, G. G. HUNDER, J. M. JORDAN, J. N. KATZ, H. M. KREMERS, F. WOLFE, N. A. D. WORKGROUP. Estimates of the prevalence of arthritis and other rheumatic conditions in the United States: Part II. *Arthritis and Rheumatism* (2008); **58**(1):26–35. 2, 117
- [47] M. LEUNIG, A. LEUNIG, K. BISE, A. GOETZ. Laser induced removal of meniscus cartilage and tendines. *Lasers in Medical Science* (1992); **7**(1):369–374. 16, 18, 117
- [48] M. LI, M. ISHII, R. H. TAYLOR. Spatial Motion Constraints Using Virtual Fixtures Generated by Anatomy. *Robotics, IEEE Transactions on* (2007); **23**(1):4–19. 9, 20, 24, 28
- [49] M. C. LIN, J. F. CANNY. A fast algorithm for incremental distance calculation. In *Robotics and Automation, 1991. Proceedings., 1991 IEEE International Conference on* (1991) 1008–1014 vol.2. 25

BIBLIOGRAPHY

- [50] R. C. O. LOCKE, R. V. PATEL. Optimal Remote Center-of-Motion Location for Robotics-Assisted Minimally-Invasive Surgery. In *Robotics and Automation, 2007 IEEE International Conference on* (2007) 1900–1905. 21, 24
- [51] P. MAILLET, B. NAHUM, L. BLONDEL, P. POIGNET, E. DOMBRE. BRIGIT, a Robotized Tool Guide for Orthopedic Surgery. In *Robotics and Automation, 2005. ICRA 2005. Proceedings of the 2005 IEEE International Conference on* (2005) 211–216. 20
- [52] P. MAINIL-VARLET, D. MONIN, C. WEILER, S. GROGAN, T. SCHAFFNER, B. ZUGER, M. FRENZ. Quantification of laser-induced cartilage injury by confocal microscopy in an ex vivo model. *Journal of Bone and Joint Surgery* (2001); **83A**(4):566–571. 16, 18, 117
- [53] F. MANTWILL, A. P. SCHULZ, A. FABER, D. HOLLSTEIN, M. KAMMAL, A. FAY, C. JURGENS. Robotic systems in total hip arthroplasty - is the time ripe for a new approach? *International Journal of Medical Robotics and Computer Assisted Surgery* (2005); **1**(4):8–19. 18, 19
- [54] P. MARAYONG, A. BETTINI, A. OKAMURA. Effect of virtual fixture compliance on human-machine cooperative manipulation. In *Intelligent Robots and Systems, 2002. IEEE/RSJ International Conference on*, vol. 2 (2002) 1089–1095 vol.2. 27, 118
- [55] P. MARAYONG, L. MING, A. M. OKAMURA, G. D. HAGER. Spatial motion constraints: theory and demonstrations for robot guidance using virtual fixtures. In *Robotics and Automation, 2003. Proceedings. ICRA '03. IEEE International Conference on*, vol. 2 (2003) 1954–1959 vol.2. 27, 28
- [56] H. MAYER, I. NAGY, A. KNOLL, E. U. BRAUN, R. BAUERNSCHMITT, R. LANGE. Haptic feedback in a telepresence system for endoscopic heart surgery. *Presence-Teleoperators and Virtual Environments* (2007); **16**(5):459–470. 20
- [57] D. S. MENCHIE, S. R. FRENKEL, B. BLAIR, N. F. WATNIK, B. C. TOOLAN, R. S. YAGHOUBIAN, M. I. PITMAN. A comparison of abrasion burr arthroplasty and subchondral drilling in the treatment of full-thickness cartilage lesions in the rabbit. *Arthroscopy: The Journal of Arthroscopic and Related Surgery* (1996); **12**(3):280–286. 15
- [58] M. MITSUSHI, N. SUGITA, K. FUJIWARA, N. ABE, T. OZAKI, M. SUZUKI, H. MORIYA, T. INOUE, K. KURAMOTO, Y. NAKASHIMA, K. TANIMOTO. Development of a medical CAD/CAM system for orthopedic surgery. *Cirp Annals-Manufacturing Technology* (2007); **56**(1):405–410. 19
- [59] C. A. J. MOORE, M. A. PESHKIN, J. E. COLGATE. Cobot implementation of virtual paths and 3D virtual surfaces. *Robotics and Automation, IEEE Transactions on* (2003); **19**(2):347–351. 27
- [60] J. B. MOSELEY, K. O'MALLEY, N. J. PETERSEN, T. J. MENKE, B. A. BRODY, D. H. KUYKENDALL, J. C. HOLLINGSWORTH, C. M. ASHTON, N. P. WRAY. A Controlled Trial of Arthroscopic Surgery for Osteoarthritis of the Knee. *New England Journal of Medicine* (2002); **347**(2):81–88. x, 13, 14
- [61] L. MURPHY, C. G. HELMICK. The Impact of Osteoarthritis in the United States: A Population-Health Perspective: A population-based review of the fourth most common cause of hospitalization in U.S. adults. *Orthopaedic nursing / National Association of Orthopaedic Nurses* (2012); **31**(2):85–91. 1, 2, 12, 13

BIBLIOGRAPHY

- [62] R. OLDFIELD. The assesment and analysis of handedness: the Edinburgh Inventory. *Neuropsychologia* (1971); **9**:97–113. 103
- [63] S. A. OLIVERIA, D. T. FELSON, J. I. REED, P. A. CIRILLO, A. M. WALKER. Incidence of symptomatic hand, hip, and knee osteoarthritis among patients in a health maintenance organization. *Arthritis and Rheumatism* (1995); **38**(8):1134–1141. 2, 117
- [64] T. ORTMAYER, G. HIRZINGER. Cartesian control issues for minimally invasive robot surgery. In Intelligent Robots and Systems, 2000. (IROS 2000). Proceedings. 2000 IEEE/RSJ International Conference on, vol. 1 (2000) 565–571 vol.1. 24
- [65] A. D. PEARLE, P. F. O’LOUGHLIN, D. O. KENDOFF. Robot-Assisted Unicompartmental Knee Arthroplasty. *Journal of Arthroplasty* (2010); **25**(2):230–237. 30
- [66] M. S. PEDERSEN, A. Z. MOGHADDAM, K. BAK, J. S. S. KOCH. The effect of bone drilling on pain in gonarthrosis. *International Orthopaedics* (1995); **19**(1):12–15. 15
- [67] M. J. PHILIPPON. Debridement of acetabular labral tears with associated thermal capsulorrhaphy. *Operative Techniques in Sports Medicine* (2002); **10**(4):215–218. 4
- [68] C. PLASKOS, P. CINQUIN. Praxiteles: a miniature bone-mounted robot for minimal access total knee arthroplasty. *International Journal of Medical Robotics and Computer Assisted Surgery* (2005); **1**(4):67–79. 21, 30
- [69] C. PLASKOS, P. CINQUIN, A. J. HODGSON, S. LAVALLEE. Safety and Accuracy Considerations in Developing a Small Sterilizable Robot for Orthopaedic Surgery. In Robotics and Automation, 2005. ICRA 2005. Proceedings of the 2005 IEEE International Conference on (2005) 930–935. 21
- [70] J. REN, R. V. PATEL, K. A. MCISAAC, G. GUIRAUDON, T. M. PETERS. Dynamic 3-D Virtual Fixtures for Minimally Invasive Beating Heart Procedures. *Medical Imaging, IEEE Transactions on* (2008); **27**(8):1061–1070. 28, 29
- [71] M. L. SCHENKER. Current trends in hip arthroscopy: a review of injury diagnosis, techniques, and outcome scoring. *Current opinion in orthopaedics* (2005); **16**(2):89–94. 4
- [72] M. L. SCHENKER, M. J. PHILIPPON. The Role of Flexible Radiofrequency Energy Probes in Hip Arthroscopy. *Techniques in Orthopaedics* (2005); **20**(1):37–44. 4
- [73] G. SCHREIBER. Fast Research Interface (FRI) - Preliminary Documentation (2010). 8
- [74] H. SHIRZAD, F. FALAHATI, A. MAJIDI, S. BAGHERI. Designing a 6 Dof Assistant Robot for Arthroscopic Surgery. In O. DÖSSEL, W. C. SCHLEGEL, eds., World Congress on Medical Physics and Biomedical Engineering, Vol 25, Pt 6, *IFMBE Proceedings*, vol. 25/6, 193–196 (Springer Berlin Heidelberg, 2009). 18
- [75] B. SICILIANO, L. SCIavicco, L. VILLANI. Robotics: modelling, planning and control (Springer, 2009). 39, 55, 56, 85

BIBLIOGRAPHY

- [76] E. STEIN, T. SEDLACEK, R. L. FABIAN, N. S. NISHIOKA. Acute and chronic effects of bone ablation with a pulsed holmium laser. *Lasers in Surgery and Medicine* (1990); **10**(4):384–388. 16, 117
- [77] N. SUGANO. Computer-assisted orthopedic surgery. *Journal of orthopaedic science : official journal of the Japanese Orthopaedic Association* (2003); **8**(3):442–448. 18, 19
- [78] T. TAKAHASHI, H. YAMAMOTO. Development and clinical application of a flexible arthroscopy system. *Arthroscopy: The Journal of Arthroscopic and Related Surgery* (1997); **13**(1):42–50. 5, 18
- [79] G. THOLEY, J. P. DESAI, A. E. CASTELLANOS. Force feedback plays a significant role in minimally invasive surgery - Results and analysis. *Annals of Surgery* (2005); **241**(1):102–109. 20
- [80] A. L. TREJOS, R. V. PATEL, M. D. NAISH. Force sensing and its application in minimally invasive surgery and therapy: a survey. *Proceedings of the Institution of Mechanical Engineers Part C-Journal of Mechanical Engineering Science* (2010); **224**(C7):1435–1454. 48
- [81] J. TROCCAZ. Computer and Robot-Assisted Medical Intervention. In S. Y. NOF, ed., Springer Handbook of Automation, 1451–1466 (Springer Berlin Heidelberg, 2009). 19
- [82] N. TURRO, O. KHATIB, E. COSTE-MANIÈRE. Haptically augmented teleoperation. In Robotics and Automation, 2001. Proceedings 2001 ICRA. IEEE International Conference on, vol. 1 (2001) 386–392 vol.1. 28
- [83] C. R. WAGNER, R. D. HOWE. Force Feedback Benefit Depends on Experience in Multiple Degree of Freedom Robotic Surgery Task. *Robotics, IEEE Transactions on* (2007); **23**(6):1235–1240. 20
- [84] A. WOLF, B. JARAMAZ, B. LISIEN, A. M. DiGIOIA. MBARS: mini bone-attached robotic system for joint arthroplasty. *International Journal of Medical Robotics and Computer Assisted Surgery* (2005); **1**(2):101–121. 19
- [85] A. WOLF, M. SHOHAM. Medical Automation and Robotics. In S. Y. NOF, ed., Springer Handbook of Automation, 1397–1407 (Springer Berlin Heidelberg, 2009). 19
- [86] A. WOLF, M. SHOHAM, S. MICHAEL, R. MOSHE. Feasibility study of a mini, bone-attached, robotic system for spinal operations - Analysis and experiments. *Spine* (2004); **29**(2):220–228. 19
- [87] L. YANG, C. B. CHNG, C. K. CHUI, D. P. C. LAU. Model-based design analysis for programmable remote center of motion in minimally invasive surgery. In Robotics Automation and Mechatronics (RAM), 2010 IEEE Conference on (2010) 84–89. 24
- [88] E. YELIN, L. MURPHY, M. G. CISTERNAS, A. J. FOREMAN, D. J. PASTA, C. G. HELMICK. Medical care expenditures and earnings losses among persons with arthritis and other rheumatic conditions in 2003, and comparisons with 1997. *Arthritis and Rheumatism* (2007); **56**(5):1397–1407. 1
- [89] P. L. YEN. A two-loop robust controller for compensation of the variant friction force in an over-constrained parallel kinematic machine. *International Journal of Machine Tools & Manufacture* (2008); **48**(12-13):1354–1365. 20

BIBLIOGRAPHY

- [90] P. L. YEN, B. L. DAVIES. Active constraint control for image-guided robotic surgery. *Proceedings of the Institution of Mechanical Engineers Part H-Journal of Engineering in Medicine* (2010); **224**(H5):623–631. 20, 27